DYNAMIC MODELS OF ELECTRON TRANSPORT IN HALL
THRUSTER SIMULATIONS

A DISSERTATION
SUBMITTED TO THE DEPARTMENT OF MECHANICAL
ENGINEERING
AND THE COMMITTEE ON GRADUATE STUDIES
OF STANFORD UNIVERSITY
IN PARTIAL FULFILLMENT OF THE REQUIREMENTS
FOR THE DEGREE OF
DOCTOR OF PHILOSOPHY

Eunsun Cha
August 2015

This dissertation is online at: http://purl.stanford.edu/bz358ff1214

I certify that I have read this dissertation and that, in my opinion, it is fully adequate in scope and quality as a dissertation for the degree of Doctor of Philosophy.

Mark Cappelli, Primary Adviser

I certify that I have read this dissertation and that, in my opinion, it is fully adequate in scope and quality as a dissertation for the degree of Doctor of Philosophy.

Matthias Ihme

I certify that I have read this dissertation and that, in my opinion, it is fully adequate in scope and quality as a dissertation for the degree of Doctor of Philosophy.

Nicolas Gascon

Approved for the Stanford University Committee on Graduate Studies.

Patricia J. Gumport, Vice Provost for Graduate Education

This signature page was generated electronically upon submission of this dissertation in electronic format. An original signed hard copy of the signature page is on file in University Archives.

Abstract

The Hall-effect thruster (HET) is an electrostatic propulsion device that relies on the Hall effect to generate a dense $E \times B$ electron current to ionize the propellant gas. In simulating Hall thrusters, describing electron cross-field transport has been one of the greatest challenges because the electron transport in a Hall thruster is anomalously higher than that predicted by classical collision theory. Researchers have suggested some explanations of the anomalous transport, but they have failed to establish a reliable physical model for general applications. Establishing a physical model that is applicable to various types of Hall thrusters in various operating conditions is an objective of this work.

In this thesis, a 2-D hybrid particle-in-cell (PIC) simulation for the Stanford Hall thruster (SHT) is used to implement the transport (electron mobility) models. Among various attempts, an entropy closure model, as well as a turbulent transport model were successfully implemented and demonstrated results that show reasonable agreement to measured data.

The entropy closure model uses a 1-D entropy transport equation in the plasma of a Hall thruster discharge to derive a relation for electron mobility as a function of other plasma properties. The simulated results show a reasonable agreement with experiments.

The turbulent transport model seeks for a more straightforward way to incorporate the entropy production mechanism into the simulation. By assuming that the Joule heating is the main source of entropy production, we adopted the turbulent kinetic theory to relate the energy dissipated from the largest eddies with the energy

production rate. Through a scaling analysis, electron mobility is expressed as an explicit function of other plasma properties of the simulation. The simulated electron mobility captures the electron transport phenomenon measured experimentally.

To test the transportability of the turbulent model, the simulation was modified for an SPT-type thruster with a different geometry than the SHT. Also, an alternative propellant, molecular nitrogen (N_2), was simulated on the geometry of the SHT using the turbulent model.

The dynamic mobility models make it possible to observe the dynamic characteristics of the Hall thruster. The mobility models in this study magnify the capability of Hall thruster simulations to explore design space cost effectively.

Acknowledgements

This section was not reviewed – it was weird to ask the people to review something that contains comments about them. Skip this part if you can't bear a writing with a lot of grammatical errors.

I've always anticipated the moment to write "acknowledgements" in my thesis, although I never imagined it to be a few days before the submission due date. Before I begin, I want to make it clear the people listed here are not ordered by the amount of gratefulness. It is random, except for the first and the last.

So, the first comes Mark, my advisor. As a Korean, I don't feel 100 % comfortable when I call him "Mark," instead of "Professor Cappelli." (It's impossibly rude to call seniors/teachers by the first name in Korea.) I appreciate his friendliness to encourage me to call him "Mark" and to freely address my ideas. I really hate to write such a cliche in my precious thesis, but it's true that I would have never finished this thesis if it were not for Mark. Not only he guided me with his brightness but also he waited very patiently when I struggled and appreciated any slight progress.

As frequently mentioned by the peers, Mark is also good at attracting nice people to our group (not necessarily meaning I am one of them). I appreciate my friends at SPPL for making my Stanford years more fun and flourishing, and also for pronouncing my name quite accurately. I deeply appreciate Eduardo for his time and effort to advise on my research for all those years. Michelle was always generous and kind to help me understanding the simulation. I also appreciate Michelle for her incredibly helpful thesis. Cheryl has been my finish-up-partner for the last year, which I enjoyed and benefited from so much. Cheryl helped me in so many ways from preparing my defense talk to reviewing this thesis (and many more outside the thesis). Chris

helped me better understand the turbulent model by applying the model to his Z-70 thruster. He also reviewed most of the poorly-written first draft – I am amazed by his patience. When I once worked at lab, Nic, Scott and Tsuyo were my heroes. I enjoyed sharing office and having conversations with Hide in 2009 and with Nakyung in 2012 (actually we talked too much and I miss it). Andrew not only helped me with my mass spectrometer setup, he was the first (and the last for now) American who invited my family for Thanksgiving feast. I appreciate Hyungrok, Sungkyun and Moonsoo for the support, kindness, and the coffee break we had. I am grateful to Aaron, Sasha, David (Scharfe), Flavio and Cliff for making a fun-filled atmosphere (long ago) which is now succeeded by Keith, Ben, Andrea, David (Biggs), Roberto, Thomas, Jack, Taemin, and Fabio. I am honored to have been a part of this wonderful team of enthusiasm.

Outside SPPL, I was lucky to make friends with Bola, Kijung, Meesook, Ahra, and Yoonjin who love and support me like family. Thanks to these ladies, I never felt lonely for those years that I have left my home country.

That does not necessarily mean that I did not miss my friends and family in Korea. I miss and thank Goeun and Soomin in Korea for their constant love and support. I appreciate all my family for praying for me.

I am especially grateful to my father for all his sacrifice and love. He was always willing to stay alone for months so that my mom could visit us and help me concentrate more on work. I am also grateful to his financial support for my education since I was a kindergartener until today. If anything is about learning (anything), my parents are generous. I admit I am spoiled by that.

I am sorry my grandmother missed my commencement because she is now too old to make a long-flight trip. I wanted to show her how Stanford is nicer than Harvard (she was sorry when I did not apply to Harvard which is to her the best school in the world.) I stayed at my grandmother's when I went to Seoul National University. She took such a good care of me, which I did not thanked enough at that time. (I should call her tomorrow.)

My brother, Deoksun, was my best friend when we were young. Although I am the elder, he always has been more mature and considerate. When I studied late to

prepare for the SAT at the library, he waited for me even though he did not need to study that late (he slept instead while waiting) to walk home together. He did so to save my father's trip to pick me up in the midnight, which I learned later. Now he came up with a nice family giving me a wonderful sister-in-law, Seunghye, and a cute niece, Yoohyun.

Now, I want to mention my favorite guys: Yeul and Chan. They have been suffering a hysterical and occupied wife and mom, and they survived. I am grateful to Yeul for working hard for our marriage. Although we have not always been happy through our 10 years of marriage, I have benefited from his love and support for sure. I am grateful to Chan for waking up before I do and fixing his own breakfast at the age of 6. He must be the most graduate-student-mom-compatible child in the world. Honestly, I did not know what it would be like to be a mom and a PhD student. Then it turned out that it was more than I could handle, which took many people's sacrifice for my PhD. The largest sacrifice was made by my mother who spent months at our home to make me a full-time student. Not all mothers can do what she's done. This thesis is dedicated to my mother who made everything possible.

Contents

List of Tables

List of Figures

Chapter 1

Introduction

1.1 Hall-Effect Thrusters

The Hall-effect thruster (HET), also known as the Hall thruster, is one of the most widely used type of electric propulsion device or, specifically, electrostatic propulsion system. The basic concept behind the Hall thruster is that ionized propellant, typically xenon, is accelerated by the applied electric field to produce thrust. It is called an electrostatic accelerator because of the use of electric fields to accelerate the ions. The Hall effect of electromagnetic fields, arranged perpendicular to each other, plays an important role in the electron-impact ionization of the injected neutral propellant by trapping a cloud of electrons in the Hall region where the Hall effect is the strongest.

The history of electric propulsion was started more than a century ago by the fathers of rocket science, Konstantin Eduardovitch Tsiolkovsky of Russia and Robert Hutchings Goddard of the US. In 1911, Tsiolkovsky speculated the possibility of using fast electrons to generate thrust [1]. In 1917, Goddard invented and patented the electrostatic ion thruster [2]. Since then, the field of electric propulsion has developed steadily although it has drawn less focus than chemical propulsion until the 1970s.

The Hall thruster configuration that resembles the modern state-of-the-art design was first developed in the early 1970s in the former Soviet Union and were introduced to North America in 1992. Since then, thanks to a more efficient use of propellant
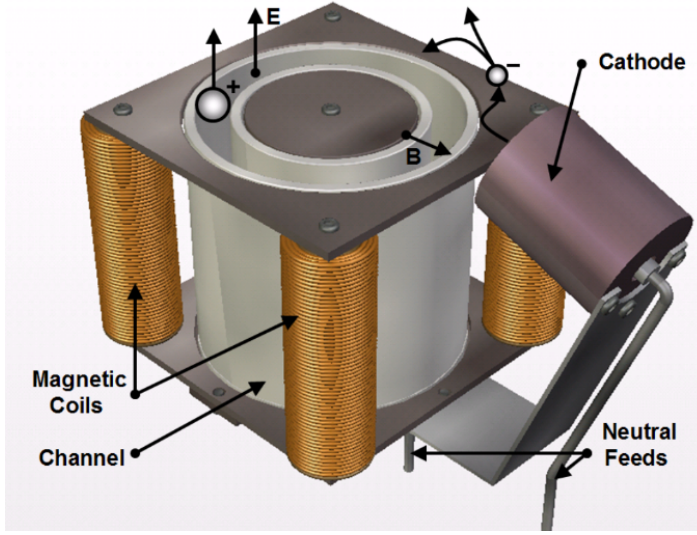
Figure 1.1: Schematic diagram of a Hall thruster.

and a higher specific impulse (I_{sp}), Hall thrusters have become the favored technology for satellite station keeping, orbit maintenance, and orbit transfer. According to Choueiri [1], more than 200 HETs have been flown on satellites in Earth orbit. HETs typically have input power in the range of 1.35-10 kW, an exhaust velocity of 10-50 km/s, thrust of 40-600 mN and an efficiency of 45-60 % [1].

Since the late 1990's, mission planners have been considering Hall thrusters as the main and/or supplemental propulsion unit for deeper and longer space missions. For example, the European Space Agency (ESA) used Hall thrusters to cost effectively propel its SMART-1 spacecraft to the moon [3].

A schematic diagram of a stationary plasma thruster (SPT) type of Hall thruster is shown in Fig. 1.1 (image borrowed from the thesis of Thomas [4]). Many modern Hall thruster designs have a coaxial shape with an annular channel surrounded by inner and outer electromagnets inside and out. The thruster shown in the schematic has an applied electric field directed from the anode to the cathode in the axial direction, which is the direction that the ionized propellant accelerates to produce propulsive thrust. The magnetic field is formed along the radial direction, which is perpendicular to the electric field. These fields create a strong $E \times B$ drift of electrons

in the azimuthal direction inside the channel. The dimension of the channel is chosen such that the Larmor radii of electrons are small enough (about 1 mm) that they remain inside the $E \times B$ region throughout their gyro-orbits, while the heavier ions are not affected by the magnetic field (they would have Larmor radius of several meters). The acceleration channel of an SPT is typically made of, or coated with, non-conducting materials such as boron nitride (BN).

Xenon has been the propellant of choice for Hall thrusters because xenon is stable and energy-efficient, i.e., xenon has a relatively lower ionization energy threshold and has relatively high atomic mass. However, the scarcity of xenon (less than 1 % ppm in air) has lead to soaring prices in recent decades, increasing the operating cost of exploratory missions that use xenon Hall and other types of electric thrusters.

1.2 Motivation and Objectives

The process of developing a new Hall thruster for commercial use can be costly and time-consuming because building prototypes and ground-testing is expensive. A reliable computer-based simulation of Hall thrusters would enable us to reduce the costly initial stage of prototyping and testing in the thruster development cycle.

In simulating Hall thrusters, describing how electrons migrate across the magnetic field (so-called electron cross-field transport) has been one of the greatest challenges because the electron transport in Hall thrusters is anomalously higher than that predicted by classical collision theory. Researchers have suggested some explanations of this anomalous transport, but they have failed to develop a reliable physical model for general applications. The motivation of this study is to add additional physics that enables one to directly solve for the electron mobility within the simulation rather than to prescribe an empirical model that requires fitting parameters that are obtained from experiments. Developing a physical model that may be universally applicable to a broad range of Hall thrusters with varying operating conditions is an objective of this work. The physical model is expected to capture the dynamic characteristics of plasmas in the Hall thrusters because the model-calculated electron mobility would reflect the instantaneous time-varying plasma properties.

1.2.1   Hall Thruster Simulation

The Hall thruster simulation used in this study is built on the same simulation platform as that widely studied in the SPPL. This initial simulation was developed by Fernandez *et al.* in 1998 [5], and is similar to that of Fife at MIT [6].

The simulation is referred to as a 2-D hybrid particle-in-cell (PIC) simulation because it models the plasma in a two-dimensional plane spanning from the inside of the channel (starting from the anode which is at high potential, ($\phi = \phi_{\mathrm{anode}}$)) to the plume of Hall thruster just beyond the exit where the cathode sets a boundary condition ($\phi = \phi_{\mathrm{cathode}}$) on the potential. It combines the PIC method for neutrals/ions with a fluid description of electrons. The PIC method is one of the most common approaches to simulating plasmas [7],[8]. This method tracks motions of a discrete number of particles in the computational domain and uses a Monte-Carlo technique when dealing with collisions between particles. The PIC method requires massive data storage in memory and a significant computational effort to produce a statistically meaningful result [9]. Thus, the majority of Hall thruster simulations (including ours) use the fluid equations for electrons on top of the PIC method for neutrals and ions instead of using PIC methods for all species (a.k.a., full-PIC models).

The dimensional resolution of dynamic variables that a simulation captures also characterizes the simulation. Using the R-Z plane of the Stanford Hall Thruster (SHT) as computational domain, the species in the simulation described here span 2-D space, while their velocities are estimated in 3-D. The other plasma properties are resolved in 2-D. A detailed description of the simulation is given in Chapter 2.

1.2.2   Anomalous Electron Transport in Hall Thrusters

To solve for plasma properties from the electron fluid equations in the 2-D hybrid PIC simulation, the electron mobility is one of the important transport parameters involved. The electron mobility, μ, is a measure of the transport of bulk electrons due to the effects of the electric and magnetic fields. In a simple case, where a group of electrons are accelerated by an applied electric field, E, the electron drift velocity,

v_d can be expressed as,

$$v_\mathrm{d} = -\mu E \tag{1.1}$$

Here, the negative sign accounts for the fact that the electrons are attracted toward the opposite direction of the electric field.

The description of electron transport has been one of the greatest challenges in simulating magnetically-confined plasma devices. The main reason for this difficulty is the so-called "anomalous electron diffusion" [10] or "anomalous transport" [11] of the electrons across the strong magnetic field. This anomalous transport is believed to be caused by fluctuations (turbulence) in the plasma and/or collisions of the electrons with surrounding walls. It has been reported (Fig. 1.2) that the rate of transport of electrons across the magnetic field is anomalously higher than that predicted by classical collision theory.

In the classical theory of electron transport, the electron mobility is described by,

$$\mu = \frac{e}{m_\mathrm{e}} \frac{\nu}{\omega_\mathrm{ce}^2 + \nu^2}, \tag{1.2}$$

where e is the fundamental charge, m_e is the mass of an electron, ν is the electron momentum transfer collision frequency between electrons and heavy particles, and ω_ce is the electron cyclotron frequency given by,

$$\omega_\mathrm{ce} = \frac{eB}{m_\mathrm{e}} \tag{1.3}$$

In most regions of a Hall thruster, the magnetic field, B, is strong enough that $\omega_\mathrm{ce} \gg \nu$. Thus, Eq. 1.2 can be approximated to an effective electron mobility:

$$\mu_\mathrm{eff} = \frac{e}{m_\mathrm{e}} \frac{\nu_\mathrm{eff}}{\omega_\mathrm{ce}^2} = \frac{\nu_\mathrm{eff}}{\omega_\mathrm{ce}} \frac{1}{B} = \frac{1}{\omega_\mathrm{ce}\tau} \frac{1}{B} \tag{1.4}$$

$\omega_\mathrm{ce}\tau$ in Eq. (1.4) is also referred to as the Hall parameter, where τ is the time scale of collisions, equal to $1/\nu_\mathrm{eff}$. Thus, the inverse Hall parameter, $\frac{1}{(\omega_\mathrm{ce}\tau)}$, is interchangeably used with mobility because they differ by a factor of B. This Hall parameter
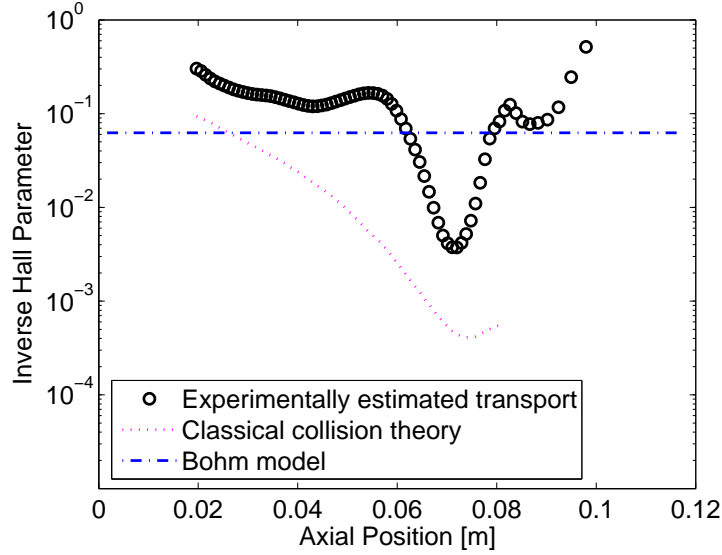
Figure 1.2: Experimental inverse Hall parameter compared with the classical value and the Bohm value at 200 V.

scales as $1/B$, so the classical mobility should thus scale as $1/B^2$. In some experiments [12], the Hall parameter is found to be independent of B (taking on a value of about 0.05) resulting in an effective mobility that varies as $1/B$. This type of scaling ($\mu \propto \frac{1}{B}$) is referred to as a Bohm-type scaling of mobility which seems to be more appropriate than the classical model for many plasma devices.

Fig. 1.2 compares the axial variation of the experimentally estimated transport [11] of electrons in a prototype thruster (SHT) with the classical value and the Bohm value. Experimental inverse Hall parameter is higher than that classical theory predicted for the whole range of comparison. Although Bohm-type mobility models are relatively straightforward to implement (blue dashed-dot in Fig. 1.2), they do not capture the spatial variations in plasma properties throughout the Hall thruster channel [13]. Early theories suggested the importance played by electron-wall scattering in enhancing the so-called near-wall conductivity [14], although it appears that the loss of the high energy electrons to the wall may not be replenished in the bulk plasma at a sufficient rate to account for the anomalous electron current [15]. Researchers have used, with some success, $ad\ hoc$ types of models with arbitrary coefficients or

combinations of the early theories. For example, Hagelaar *et al.* used an *ad hoc* model that combines an empirical collision model with wall effects for the region inside of channel and a Bohm-type model for the region outside of the channel [16]. However, the *ad hoc* models seem to be incapable of capturing plasma properties accurately without adjustable parameters derived from experiments.

Therefore, at Stanford, an effort has gone into developing a reliable physical mobility model to enhance the transportability and accuracy of our 2-D hybrid particle-in-cell (PIC) simulations of Hall thrusters. Those efforts have yielded the 1-D isentropic fluid model of Knoll [17], the shear-based transport model of Scharfe [13], the entropy closure model (see Chapter 3), and the turbulent transport model (see Chapter 4) for 2-D hybrid PIC Hall thruster simulations, the latter two of which form the basis for this thesis.

To extend the simulation as a tool to design novel devices or to explore the range of operating conditions that have not been experimentally tested, this thesis focused on developing a reliable physical model for electron transport for robust simulations of Hall thrusters.

1.3 Organization

This thesis contains three methods to describe the electron transport in Hall thrusters: the entropy closure model, the turbulent transport model, and the polytropic model. Among those models, the entropy closure model, as well as the turbulent transport model were successfully implemented and demonstrated results that show reasonable agreement to measured data. All of the attempts are related to modeling entropy production of plasma in Hall thrusters. The basic idea that the effective electron mobility is solved within the simulation by a physical modeling or an equation rather than being prescribed becomes capable by adding one more equation to the set of electron equations.

In Chapter 2, a detailed description of the simulation platform to implement the models are given. Chapter 3 will relay the model description and simulation results of the entropy closure model. The entropy closure model adds an 1-D entropy transport

equation with an assumed form of entropy source, which leads to an expression for electron mobility as a function of other plasma properties.

In Chapter 4, the model description and simulation results of the turbulent transport model follow. With the assumptions that the Joule heating is the main source of the plasma entropy production and that the turbulent dissipation is closely related to the electron mobility, a zero-equation model for the electron mobility is derived and implemented into the SHT simulation. Motivated by the successful implementation, the turbulent model is also tested with the geometry of an SPT-100 type thruster in the latter of the Chapter.

Finally, in Chapter 5, the development and initial tests of a N_2 Hall thruster using the turbulent transport model are presented. The modification and optimization of the N_2 Hall thruster is also suggested in Appendix.

The polytropic model is not included in the main body of the thesis because this model has not been fully tested. But the motivation and the model description can be found in the Appendix.

Chapter 2

Hall Thruster Simulation

2.1 Overview

A 2-D hybrid particle-in-cell (PIC) simulation was used as a platform to implement the dynamic mobility models and a nitrogen fueled Hall thruster introduced in Chapter 1. The version of the simulation used in this study is similar to the one used by Scharfe [13], which models the plasma on the radial-axial (R-Z) plane of the Stanford Hall thruster (SHT), a coaxial SPT-type laboratory Hall thruster. The SHT has an annular acceleration channel, as depicted in Fig. 2.1 (from the thesis of Aaron Knoll [18]). The simulated geometry includes a thruster channel 8 cm in length and 1.2 cm in width as well as the plume just beyond the exit plane, graphically depicted in Fig. 2.2 along with the magnetic field. The magnetic field is a result of the central north magnetic pole and the south outer poles at the four corners. It peaks near the exit plane of the thruster and reaches levels as high as 160 Gauss. This region where the magnetic field peaks corresponds to the Hall region, where the electron population is highest due to the Hall effect, creating a region of efficient ionization.

In this chapter, details of the R-Z hybrid simulation used in this study is described in the order of its algorithmic flow. As an overview, the flowchart and the pseudo-code of the simulation are presented first. The assumptions on which the simulation is based on are followed. Then the PIC part and electron fluid equations are introduced.
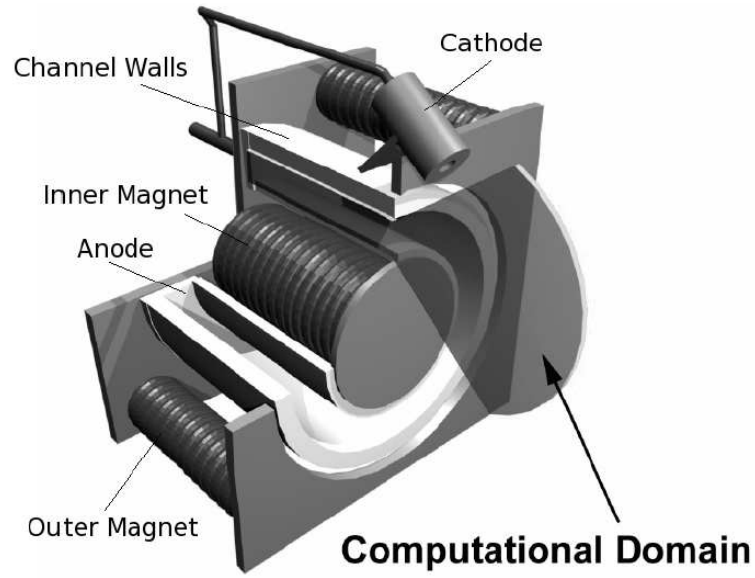
Figure 2.1: HET and the radial-axial (RZ) domain.
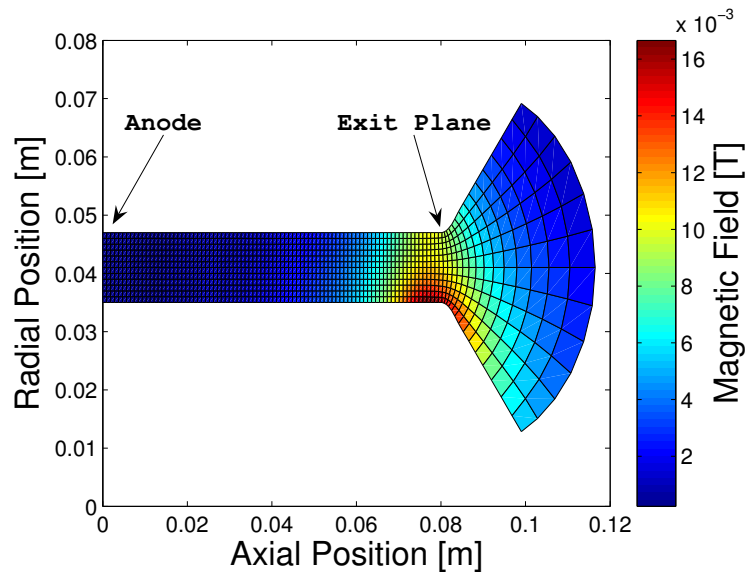
Figure 2.2: HET and RZ domain with applied magnetic field.

2.2 Algorithm

As mentioned in Chapter 1, the simulation consists of two subcodes: a PIC solver for heavy particles (neutrals and ions) and electron equations. Data calculated from the simulation include: particles' information (position, velocity, and group-mass), electron temperature, T_e, and corresponding electric potential, ϕ, electric field, E, and discharge current, I_d. The computation algorithm is as follows:

---

initialization

for each ion time step **do**

    PIC: advance ions and neutrals, ionize neutrals and update $n_i, \vec{v}_i, n_n, \vec{v}_i$

    update $n_e \leftarrow n_i$

    update T_e 250 times using smaller time step

    update ϕ w.r.t. T_e

    while $(V_d - \phi_{\text{anode}} > \text{tolerance})$ **do**

        update $I_d \leftarrow I_d + \Delta I_d$ where $\Delta I_d = f(V_d - \phi_{\text{anode}})$

        update T_e 250 times using smaller time step

        update ϕ w.r.t. T_e

    end while

end for

---

where the simulation variables are defined as:

$$n = \text{number density}$$
$$\vec{v} = \text{velocity}$$
$$V_d = \text{discharge voltage}$$
$$\text{subscript i} = \text{ion}$$
$$\text{subscript n} = \text{neutral}$$
$$\text{subscript e} = \text{electron}$$

Graphical representation of the algorithm is presented in the flowchart of Fig. 2.3.
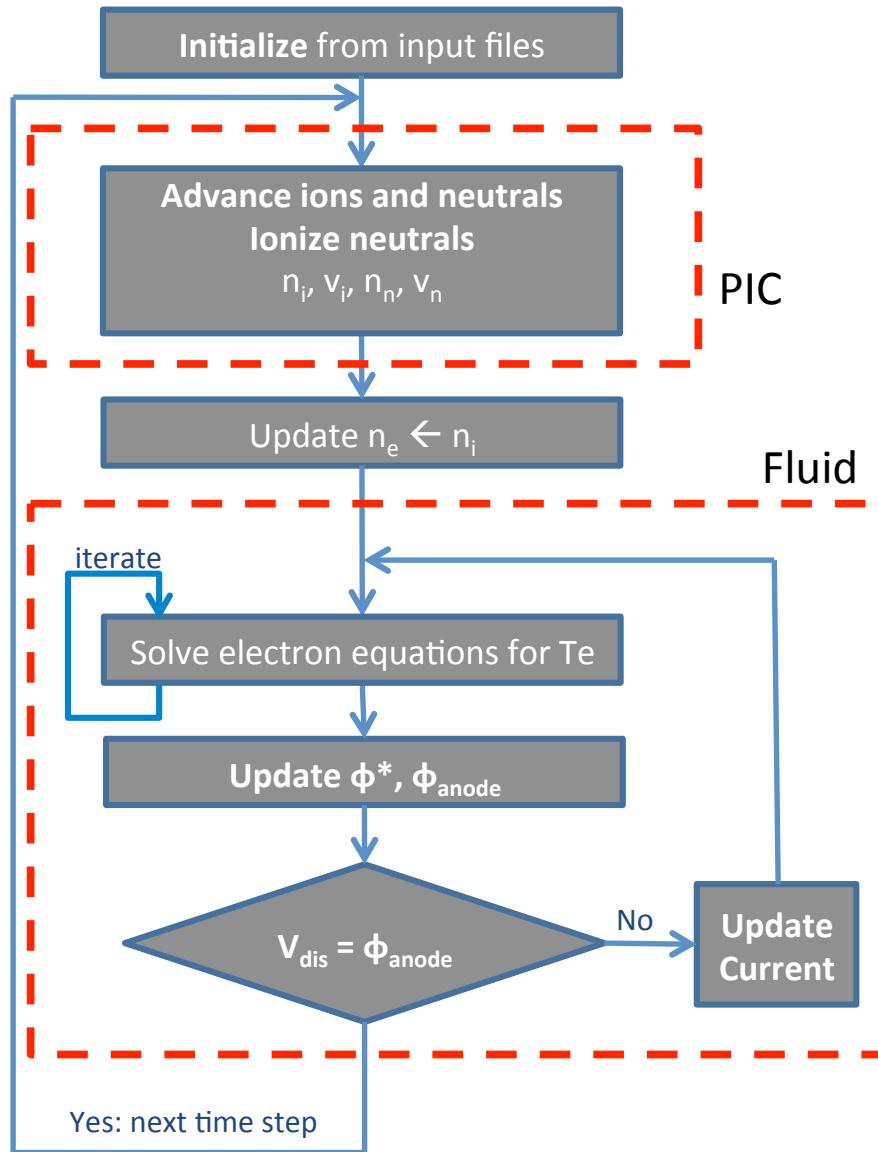
Figure 2.3: Flowchart of the hybrid Hall thruster simulation.

2.3 Assumptions

2.3.1 Coexistence of Two Discrete Time Steps

The main loop iterates over ion time steps for the PIC section of the code, which are distinct from the electron time steps used in the fluid portion of the code (250 electron steps per ion step). Because of their heavier mass, ions and neutrals move much more slowly than electrons. To reduce the computational cost of the PIC part, properties of heavy particles are assumed to be constant over a longer time period (ion time step) and are not updated as often as those of electrons in the simulations. In other words, for each ion time step, electron equations are solved multiple times with respect to the finer electron time scale.

2.3.2 Quasi-Neutrality of the Plasma

At each ion time step, electron density (n_e) is passed to the electron equation solver after the PIC code updates the properties of ions and neutrals. Here, we assume quasi-neutrality of the plasma in the Hall thruster, in which, the electric charge of the plasma is macroscopically neutral ($n_e \approx n_i$) when the length scale is larger than the Debye length [19]. Debye length, λ_D is a length scale arises naturally from Poisson's equation for a system of different species with different charges and for plasma it can be expressed as follows:

$$\lambda_D = \sqrt{\frac{\varepsilon_0 k_B T_e}{n_0 e^2}} \tag{2.1}$$

where ε_0 is the permittivity of free space, k_B is Boltzmann's constant, n_0 is the bulk plasma density, and T_e is the plasma temperature. For a Hall thruster with the typical T_e range of 5 - 20 eV and n_e range of $10^{16} - 10^{18}$ m^{-3}, the Debye length is in the order of 0.01 mm.

Table 2.1: Ionization reactions of Xe.

Reactions	Threshold Energy [eV]
$Xe + e^- \rightarrow Xe^+ + 2e^-$	12.1
$Xe + e^- \rightarrow Xe^{2+} + 3e^-$	33.3
$Xe^+ + e^- \rightarrow Xe^{2+} + 2e^-$	21.2

2.3.3 Ionization

Ion production is assumed to occur only through electron-neutral collisions. More specifically, the simulation considers only the ionization processes described by Eq. 2.2 or 2.3 for each propellant.

$$Xe + e^- \rightarrow Xe^+ + 2e^- \tag{2.2}$$

$$N_2 + e^- \rightarrow N_2{}^+ + 2e^- \tag{2.3}$$

Therefore, the singly charged ions (Xe^+ or N_2^+) are assumed to be the dominant ion species, although the simulation is equipped with the ability to compute the doubly charged ions for xenon (Xe^{2+}).

This assumption seems reasonable for xenon propellant from the evidence given by Scharfe [13], where she concluded that due to their small population (less than 10%), the effect of including Xe^{2+} is negligible on most plasma properties within the hybrid simulation. This agrees with intuition obtained from comparing the ionization threshold energy for each ionization state, given in Table 2.1.

For the Hall thruster with molecular nitrogen propellant, treating N_2^+ as the dominant ion species seems reasonable; however, the exclusion of the other chemical reactions might be more problematic than in the case of xenon propellant. This issue is discussed in more detail in Chapter 5.

Ionization cross section for the reactions are used to calculate the ion production rate (same as the neutral depletion rate) for both the PIC subcode and the fluid equation solver. The published ionization cross section measurements by Rejoub *et*

al. [20] and Nagy *et al.* [21] are used for calculating ionization rates (Eq. 2.2) as a function of electron temperature and assuming Maxwellian velocity distribution of electrons (f_M) as follows:

$$\frac{dn_e}{dt} = n_e n_n \underbrace{\int \int \int_{C_e} |C_e| \cdot \sigma(|C_e|) f_M dV_C}_{f(T_e)} \tag{2.4}$$

where we assume electron velocity C_e is much larger than the velocity of the colliding partner, C_n, because the electrons are have lighter mass and higher temperature. $\sigma(|C_e|)$ is substituted bt experimental cross-sections referred above, and we fit the calculated ionization rate function $f(T_e)$ of temperature in the following form:

$$f(T_e) = A \left[\log(T_e/B)\right]^C \exp\left[-D \left(\log(T_e/B)\right)^E\right] \tag{2.5}$$

where the fitting parameters for the single ionization of xenon used in the simulation are given below and the constructed function is plotted in Fig. 2.4.

$$A = 0.0074455$$
$$B = 4.9105$$
$$C = -8.6830$$
$$D = 1.3927 \times 10^5$$
$$E = -4.3602$$

For calculating ionization rates of N_2 (Eq. 2.3), the Binary-Encounter-Bethe (BEB) model of Hwang *et al.* [22] is used. More details can also be found in Chapter 5.

2.3.4 Imposed Conditions

Discharge voltage, V_d, and propellant mass flow rate, $\dot{m}$ are imposed as operating conditions as in the prototype experiments. Typical set of operating conditions for the SHT is 200 V discharge voltage and 2 mg/s xenon flow rate. Although all simulation results presented in this study were run with fixed V_d as a constant unless otherwise
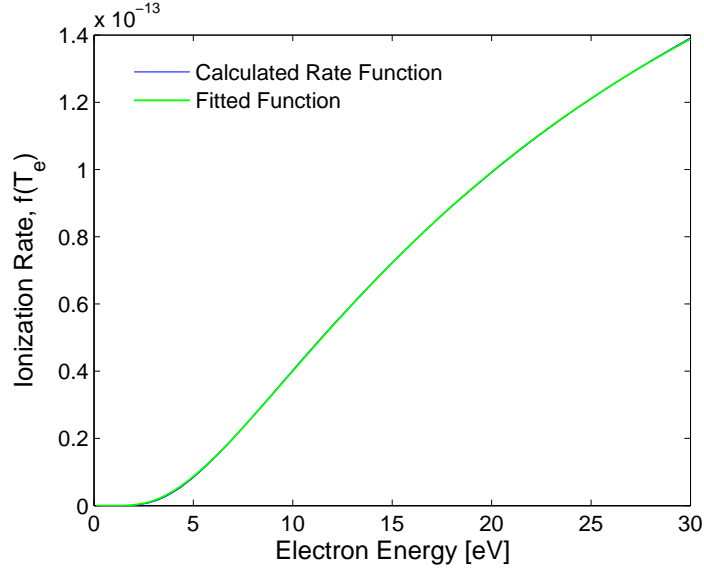
Figure 2.4: Ionization rate function of single ionization of xenon, $Xe + e^- \rightarrow Xe^+ + e^{2-}$

noted, the actual voltage at the anode might vary due to the external circuit and power supplies used in the experimental setup. In the Appendix, this external circuit effect is investigated by implementing an RLC circuit model of the laboratory setup in which the discharge voltage is allowed to vary in time. As shown in the flowchart (Fig. 2.3), the electron equations are iteratively solved by Newton's method for discharge current until the resulting potential at anode agrees with the imposed discharge voltage. The applied magnetic field plotted in Fig. 2.2 is also set as a constant at the initialization step.

2.4   Heavy Particles

In the PIC method, the heavy particles are grouped as "superparticles" which represent about $10^6 - 10^8$ actual ion particles or $10^8 - 10^{10}$ actual neutral particles. In a typical SHT simulation with xenon propellant, there are approximately 500,000 neutral superparticles and 300,000 ion superparticles in overall domain. At each time step, the heavy particles are injected, ionized, and pushed along the two-dimensional

R-Z domain shown in Fig. 2.2, and all of their position, velocity, and mass information is tracked.

Neutral particles are injected at the anode at the prescribed mass flow rate with a one-way flux Maxwellian velocity distribution at the prescribed anode temperature, 1000 K typically. Without external forces, the neutrals move with respect to the simplified equations of motion in cylindrical coordinates:

$$\dot{z} = \text{constant} \tag{2.6}$$

$$\ddot{r} - r\dot{\theta}^2 = 0 \tag{2.7}$$

$$r^2\dot{\theta} = \text{constant} \tag{2.8}$$

Ions, however, are influenced by the applied electromagnetic field in the Hall thruster. While the applied electric field accelerates the ions toward the cathode, the magnetic field does not significantly affect the motion of ions because of their high mass (or inertia) and because their Larmor radius of ions are much larger than the channel's length scale. Thus, the following equations describe the motion of the ions.

$$\ddot{z} = -\frac{e}{m}\frac{\partial \phi}{\partial z} \tag{2.9}$$

$$\ddot{r} - r\dot{\theta}^2 = -\frac{e}{m}\frac{\partial \phi}{\partial r} \tag{2.10}$$

$$r^2\dot{\theta} = \text{constant} \tag{2.11}$$

Note that, although an azimuthal electric field may exist, the axisymmetry of the simulation ignores the variations in the azimuthal direction.

2.5 Electron Equations

The electrons are treated as a conducting fluid in the hybrid simulation and governed by the first three moments of the Boltzmann equation which represent mass, momentum and energy conservation of electrons [19].

$$\frac{\partial n_{\rm e}}{\partial t} + \nabla \cdot (n_{\rm e}\vec{v}_{\rm e}) = w_{\rm i} \tag{2.12}$$

$$m_{\rm e}n_{\rm e}\left(\frac{\partial \vec{v}_{\rm e}}{\partial t} + \vec{v}_{\rm e} \cdot \nabla \vec{v}_{\rm e}\right) = -en_{\rm e}\vec{E} - en_{\rm e}\vec{v}_{\rm e} \times \vec{B} - \nabla \cdot P_{\rm e}$$

$$- \nu_{\rm en}\left(\vec{v}_{\rm e} - \vec{v}_{\rm n}\right)m_{\rm en}n_{\rm e} - \nu_{\rm ei}\left(\vec{v}_{\rm e} - \vec{v}_{\rm i}\right)m_{\rm ei}n_{\rm e} - \vec{v}_{\rm e}m_{\rm e}w_{\rm i} \tag{2.13}$$

$$\frac{\partial}{\partial t}\left(\frac{3}{2}n_{\rm e}k_{\rm B}T_{\rm e}\right) + \frac{\partial}{\partial \hat{n}_\perp}\left(\frac{5}{2}n_{\rm e}v_{{\rm e},\perp}k_{\rm B}T_{\rm e} - K_{\rm eff}\frac{\partial T_{\rm e}}{\partial \hat{n}_\perp}\right)$$

$$= j_{{\rm e},\perp}E_\perp - \sum w_{\rm i}\,\psi(T_{\rm e})\,\varepsilon_{\rm i} - \Gamma_{\rm w} \tag{2.14}$$

where

$$w_{\rm i} = \text{ion production rate} = n_e n_n f(T_e)$$

$$f(T_{\rm e}) = \text{ionization rate function}$$

$$P_e = \text{electron pressure tensor}$$

$$\nu_{\rm en} = \text{electron-neutral collision frequency}$$

$$\nu_{\rm ei} = \text{electron-ion collision frequency}$$

$$k_{\rm B} = \text{Boltzmann constant}$$

$$K_{\rm eff} = \text{effective thermal conductivity} = \frac{8n_{\rm e}k_{\rm B}^2 T_{\rm e}\mu_{\rm eff}}{\pi e}$$

$$\mu_{\rm eff} = \text{effective electron mobility}$$

$$j = \text{current density}$$

$$\psi(T_{\rm e}) = \text{ion production cost factor}$$

$$\varepsilon_{\rm i} = \text{threshold energy of ionization}$$

$$\Gamma_{\rm w} = \text{energy loss due to the electron flux to the wall}$$

In treating these equations, we consider the coordinates in two directions: perpendicular ($\hat{n}_\perp$) and parallel ($\hat{n}_\parallel$) to the magnetic contours. Magnetic contours are equally spaced with respect to the magnetic stream function, λ. Since $\nabla \cdot \vec{B} = 0$, it is possible to define a magnetic stream function whose gradient is orthogonal to $\vec{B}$,

such that λ satisfies the following relations in R-Z coordinates:

$$B_{\mathrm{r}} = \frac{1}{r}\frac{\partial\lambda}{\partial z} \tag{2.15}$$

$$B_{\mathrm{z}} = -\frac{1}{r}\frac{\partial\lambda}{\partial r} \tag{2.16}$$
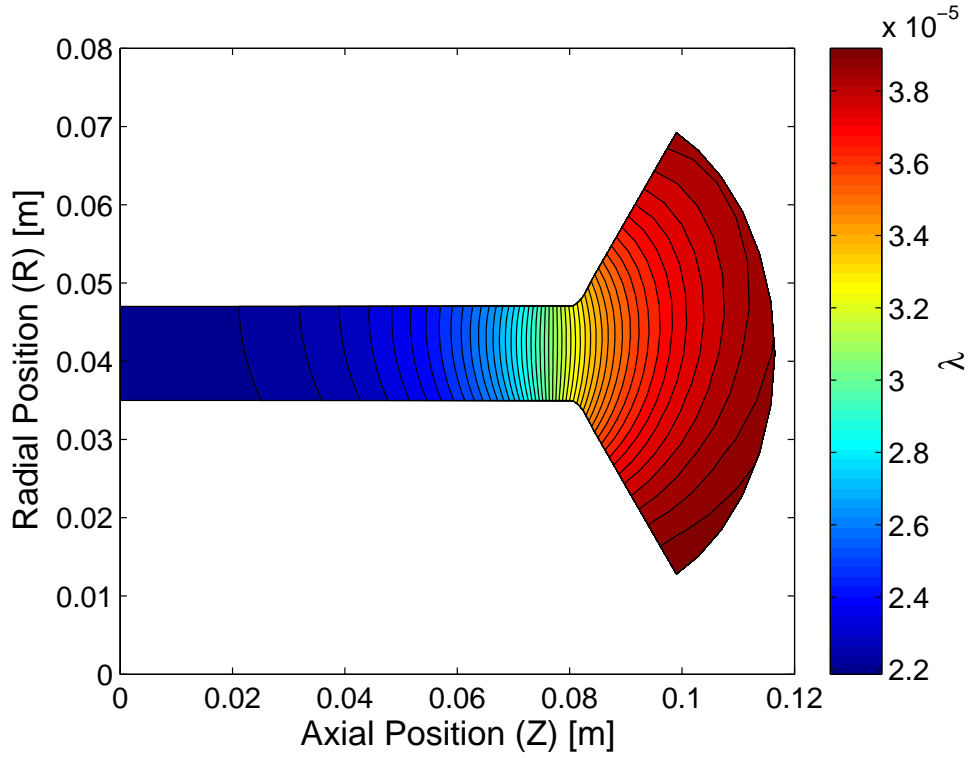
Figure 2.5: Contour plots of magnetic stream function, λ

Figure 2.5 shows an example of the λ contours resulting from the SHT's magnetic field shown in Fig. 2.2. The nominal number of λ contours is 200 in the hybrid simulation. To better resolve the region where the magnetic field changes drastically, the number of contours was increased up to 800 for the simulations with the dynamic mobility models in this study. Note that the choice of $\hat{n}_{\perp} - \hat{n}_{\parallel}$ coordinates do not agree with the R-Z grid for the PIC part of the simulation. Therefore, interpolating plasma properties between the two coordinates is required after each subcode is executed.

Assuming a Maxwellian velocity distribution of electrons, and given an ion field from the PIC subcode, Eqs. 2.12–2.14 are sufficient to solve for the electron velocity, electric potential, and electron temperature as functions of time.

2.5.1   Simplifying Momentum Conservation

The generalized Ohm's law given by Eq. 2.13 can be simplified by the assumptions valid for Hall thruster operations.

- Inertial terms are negligible because thermal energy is much greater than directed energy.

- Isotropic pressure: $P_e = p_e \, \mathbf{1}$.

- $\vec{v_e} \gg \vec{v_n}, \vec{v_i} \quad \Rightarrow \quad \vec{v_e} \approx (\vec{v_e} - \vec{v_n})$ and $\vec{v_e} \approx (\vec{v_e} - \vec{v_i})$ to combine the electron-neutral and electron-ion collision frequencies, $\nu_e = \nu_{en} + \nu_{ei}$.

Then, the simplified momentum equation becomes:

$$0 = -en_e\vec{E} - en_e\vec{v}_e \times \vec{B} - \nabla p_e - \nu_e\vec{v}_e m_e n_e \qquad (2.17)$$

Here, the electric field $\vec{E} = -\nabla\phi$ and we assume ideal gas law for the isotropic pressure, i.e., $p_e = n_e k_B T_e$. Also, note that the second term in the right hand side of Eq. 2.17 is canceled to 0 for the radial-axial domain, i.e., $E \times B$ term is purely azimuthal.

2.5.2   Calculation of electric potential

The electron mobility along the magnetic contours is considered to be very large, because collisions with heavy particles are negligible due to the large mean free path (order of 1 meter). Since the thermal conductivity is assumed to scale with the electron mobility, the electron temperature is assumed to be constant along magnetic contours. Thus, the momentum equation in the parallel direction can be simply

integrated along a magnetic contour as follows:

$$0 = -en_\mathrm{e}E_\parallel - \frac{\partial p_\mathrm{e}}{\partial \hat{n}_\parallel} \tag{2.18}$$

$$\frac{\partial \phi}{\partial \hat{n}_\parallel} = \frac{k_\mathrm{B}T_\mathrm{e}}{en_\mathrm{e}} \frac{\partial n_\mathrm{e}}{\partial \hat{n}_\parallel} \tag{2.19}$$

$$\phi = \frac{k_\mathrm{B}T_\mathrm{e}}{e} \ln n_\mathrm{e} + \phi^* \tag{2.20}$$

where the thermalized potential ϕ^* varies from contour to contour. To integrate for the potential at each position along a contour, ϕ^* must be calculated first. As a boundary condition, ϕ and T_e at cathode are given as 19 V and 32275 K respectively, for the contour that passes the cathode. This correspond to the values measured by Meezan *et al.* [11].

2.5.3 Relation of electron velocity

The perpendicular component of the momentum equation gives a relation for electron velocity and other properties we deal with in the simulation as follows:

$$v_{\mathrm{e},\perp} = -\mu_\mathrm{eff} \left(E_\perp + \frac{k_\mathrm{B}T_\mathrm{e}}{en_\mathrm{e}} \frac{\partial n_\mathrm{e}}{\partial \hat{n}_\perp} + \frac{k_\mathrm{B}}{e} \frac{\partial T_\mathrm{e}}{\partial \hat{n}_\perp} \right) \tag{2.21}$$

Here, the effective electron mobility, μ_eff, can be either an imposed constant or a variable calculated within the simulation depending on the mobility model. Most of the hybrid Hall thruster simulations use a constant imposed mobility as mentioned in Chapter 1. For the dynamic mobility models discussed in this study, μ_eff is calculated within the simulation and updated every ion time step after the PIC subcode.

2.5.4 Discharge Current Relation

Writing the ion continuity equation using the same ion production rate, w_i, as Eq. 2.12, we get:

$$\frac{\partial n_\mathrm{i}}{\partial t} + \nabla \cdot (n_\mathrm{i}\vec{v}_\mathrm{i}) = w_i \tag{2.22}$$

Using quasi-neutrality ($n_\mathrm{e} = n_\mathrm{i}$), subtracting above Eq. 2.22 from Eq. 2.12 yields the following relation.

$$\nabla \cdot (n_\mathrm{e}(\vec{v_\mathrm{i}} - \vec{v_\mathrm{e}})) = 0 \tag{2.23}$$

$$\Rightarrow \nabla \cdot \vec{J} = \nabla \cdot (en_\mathrm{e}\vec{v_\mathrm{i}} - en_\mathrm{e}\vec{v_\mathrm{e}}) = 0 \tag{2.24}$$

where $\vec{J}$ is the total current density. Using the divergence theorem,

$$\int_S \vec{J} \cdot dS' = 0 \tag{2.25}$$

where S is any closed surface. This relation implies that the net current through the channel is constant at any location. Thus, by calculating the anode current that passes through the cross-sectional area, A, perpendicular to the magnetic contours at the anode, we can calculate the discharge current, I_d, as following.

$$I_\mathrm{d} = I_\mathrm{a} = e \int_A n_\mathrm{e}(\vec{v_\mathrm{i}} - \vec{v_\mathrm{e}}) \cdot dA' \tag{2.26}$$

Here, we only need the velocity component in the direction perpendicular to contours. Use axisymmetry to yield,

$$I_\mathrm{d} = 2\pi e \int_l n_\mathrm{e}(v_\mathrm{i,\perp} - v_\mathrm{e,\perp})rdl' \tag{2.27}$$

where l is the magnetic contour and r is the radial position from the thruster centerline. This relation is used to calculate the thermalized electric potential, ϕ^*, at each contour, which is the constant of integration in Eq. 2.20. $\frac{\partial \phi^*}{\partial \lambda}$ can be derived by substituting $v_\mathrm{e,\perp}$ (Eq. 2.21) into the this I_d relation (Eq. 2.27) and using $\vec{E} = -\nabla\phi$.

2.5.5   Calculation of Electron Temperature

Electron energy equation (2.14) is solved for electron temperature (T_e) by a fourth-order Runge-Kutta scheme [23]. Terms on the left hand side of this equation represent the material derivative, flow work, and thermal convection, respectively. The right

hand side consists of the joule heating source term and two energy losses due to ionization and wall interactions.

Ionization Cost

Ionization energy loss is calculated by a cost factor (ψ) multiplied to the ionization rate to account for the energy loss due to the non-ionizing collisions. The ion production cost factor for xenon adopts the Dugan's model [24] which is an exponentially decreasing function of electron temperature scaled to the ratio of the first excitation energy to the first ionization energy, ε_i of xenon:

$$\psi(T_e)_{Xe \to Xe^+} = 1.655 \exp\left(\frac{0.3163}{T_e/\varepsilon_i}\right) + 0.1336 \tag{2.28}$$

Dugan's model depicted in Fig. 2.6, assumes that the majority of the energy cost for the target ionization is approximated by the energy wasted by the first excitation, which works well for xenon.

However, the bookkeeping of energy consumption from the non-ionizing reactions of N_2 seems to be far more complex. Thus, the ionization cost for N_2 is not directly modeled but approximated by referencing that of xenon's at the corresponding reduced electric field, E/n_e. The further detail of calculating ionization cost for N_2 using this technique is discussed in Appendix.

Heat Loss to the Walls

The last term in the right hand side of the energy equation 2.14, Γ_w, accounts for the net energy density loss due to the interaction between electrons and the sheath near the wall [13]:

$$\Gamma_w = \frac{\Gamma_e}{L} \left(2k_B T_e + e\phi_w - \bar{\sigma}e\phi_w - 0.57 \times 0.6 \times 2k_B T_e\right), \tag{2.29}$$
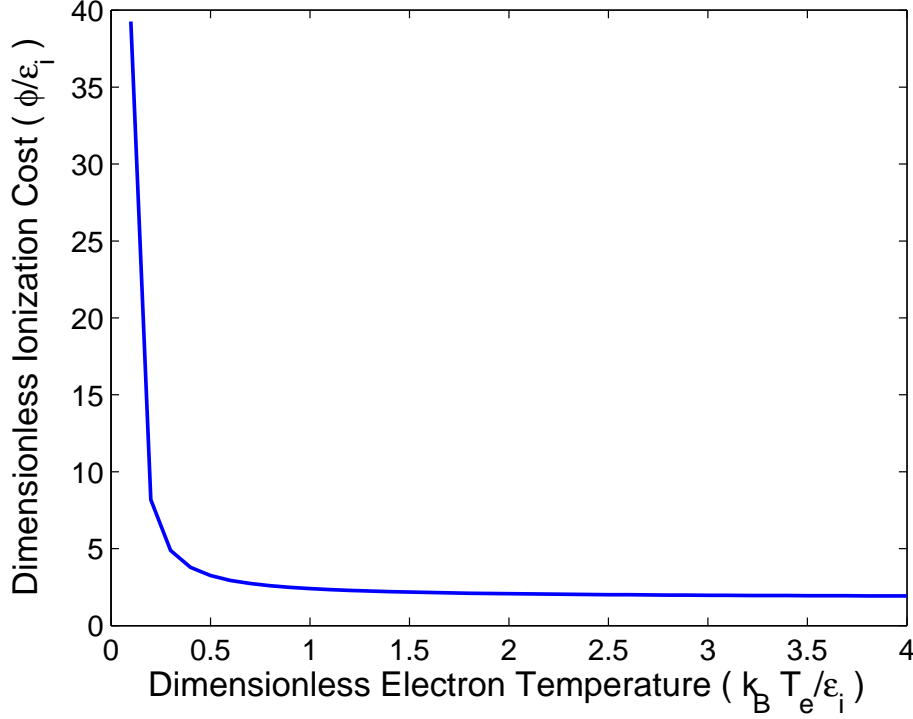
Figure 2.6: Nondimensionalized ion production cost factor of Dugan's Model.

where Γ_e is the net electron flux which can be related to the net ion flux, Γ_i, using continuity as follows.

$$\Gamma_e = (1 - \bar{\sigma})\Gamma_i = (1 - \bar{\sigma})n_e\sqrt{\frac{k_B T_e}{m_i}} \qquad (2.30)$$

And L is the length of the magnetic contour. ϕ_w is the wall potential or the sheath potential relative to the potential at the edge of the presheath. ϕ_w is modeled as a function of $\bar{\sigma}$, the electron emission yield due to electron scattering from the wall, as follows.

$$\phi_w = \begin{cases} \frac{k_B T_e}{e} \ln\left[(1 - \bar{\sigma})\sqrt{\frac{m_i}{2\pi m_e}}\right] & : \bar{\sigma} < 0.98 \\ 1.02\frac{k_B T_e}{e} & : \bar{\sigma} \geq 0.98 \quad \text{(space charge saturation)} \end{cases} \qquad (2.31)$$

Here, the analysis of Barral *et al.* [25] for the electron emission yield, $\bar{\sigma}$, for alumina

is used, which assumes that 57% of electrons striking the walls are backscattered electrons, which are assumed to retain 60% of their primary energy.

$$\bar{\sigma}(T_\mathrm{e}[\mathrm{eV}]) = 0.57 + \frac{2T_\mathrm{e}}{18\,[\mathrm{eV}]} \tag{2.32}$$

The further details on the derivation toward Eq. 2.29 can be found at [13].

Chapter 3

Entropy Closure Model

3.1 Motivation

Motivated by Knoll and Cappelli's success with a one-dimensional implementation [17], we implemented an isentropic model in a 2-D hybrid simulation with an assumption that the spatial variation of entropy along the channel of a Hall thruster is negligible [26]. In its implementation, the isentropic relation, $T_e \propto n_e^{2/3}$, is expanded to a polytropic relation, $T_e \propto n_e^k$, where k, the polytropic constant of a positive real number. This implementation turned out to be difficult for two reasons. First, the isentropic model has an inherently positive feedback characteristic, which hampers convergence. Second, early simulation results for a limited set of thruster conditions suggested the possible failure of the isentropic assumption in some regions of the thruster channel. In essence, the assumption of zero entropy production may not be valid in regions where electron-scattering collisions are very frequent.

Consequently, we developed a new model to describe electron transport in Hall thrusters, which we refer to as an entropy closure model. In this approach, we model the entropy production and its scaling with effective collision frequency, ν_{eff}, and magnetic field, B, and use a transport equation for electron entropy to close the set of equations for the electron fluid. The transport equation for electron entropy allows us to calculate the electron drift velocity, which defines the electron mobility in accordance with the electron momentum equation (Eq. 2.13) used in the hybrid

Hall thruster simulations. Therefore, the effective electron mobility, μ_{eff}, in Eq. 2.21 becomes a calculated parameter that is dynamically linked to the other plasma properties within the framework of a simulation.

3.2 Numerical Model

3.2.1 Assumption

Our approach to modeling entropy production is to examine its possible dependence on plasma properties, such as the plasma density, plasma collisionality, and the applied magnetic field. The basic assumption is that in the regions of strong magnetic field, effective collisions are less frequent, and the rate of entropy production is expected to be small. This assumption guides the selection of a maximal set of parameters to determine the dimensionless relation that governs the local scaled entropy production, $\dot{s}_{\text{e}}/k_{\text{B}}$. The set is assumed to include plasma density, n_{e}, the local magnetic field, B (through the local electron cyclotron frequency $\omega_{\text{ce}} = eB/m_{\text{e}}$), and the local effective collision frequency, ν_{eff}, which encompasses both physical and virtual electron scattering, i.e., the scattering of electrons as a result of coherent and turbulent fluctuations in the electric field [27]. Such scattering is important in entropy production as it allows the electrons to sample the micro-canonical electron energy states of the system. The experiments [11] guide us in this reasoning through the wealth of data that suggests that in regions of strong magnetic field, the effective collisionality (ν_{eff}) is weak and so the rate of entropy production ($\dot{s}_{\text{e}}$) is expected to be small.

3.2.2   Determination of Entropy Production

Dimensional reasoning [28] reduces the maximal set of nondimensional Π groups to two:

$$\Pi_1 = \frac{\dot{s}_e}{n_e k_B \nu_{\text{eff}}} \tag{3.1}$$

$$\Pi_2 = \frac{\omega_{\text{ce}}}{\nu_{\text{eff}}} \tag{3.2}$$

which indicates that the entropy production $\dot{s}_e$ depends on an unknown function (f) of the Hall parameter, $\omega_{\text{ce}}/\nu_{\text{eff}}$:

$$\dot{s}_e = n_e k_B \nu_{\text{eff}} \cdot f\left(\frac{\omega_{\text{ce}}}{\nu_{\text{eff}}}\right) \tag{3.3}$$

Recall from Eq. 1.4 that the Hall parameter is inversely proportional to the effective electron cross-field mobility, μ_{eff}. The functional dependence of f must be determined by empirical means. As the first approach, a simple function that is linear with respect to the inverse Hall parameter is tested, i.e.,

$$f\left(\frac{\omega_{\text{ce}}}{\nu_{\text{eff}}}\right) \approx \alpha \frac{\nu_{\text{eff}}}{\omega_{\text{ce}}} \tag{3.4}$$

where α is constant. α is taken to be of order of unity for the initial implementation. Thus, the volumetric entropy production rate used is,

$$\dot{s}_e = n_e k_B \frac{\nu_{\text{eff}}^2}{\omega_{\text{ce}}} \tag{3.5}$$

$$= n_e k_B \omega_{\text{ce}} B^2 \mu_{\text{eff}}^2 \tag{3.6}$$

3.2.3   Entropy Transport Equation for Electrons

A transport equation for entropy, s_e, is required to close the set of equations for the electron fluid, where the existing equations are the first three moments of the

Boltzmann equation as described in Section 2.5. We take the entropy equation as [29]:

$$\frac{\partial(n_e s_e)}{\partial t} + \nabla \cdot n_e s_e \vec{u_e} = -\nabla \cdot \frac{\vec{q_e}}{T_e} + \dot{s}_e \tag{3.7}$$

or

$$n_e \frac{Ds_e}{Dt} = -\nabla \cdot \frac{\vec{q_e}}{T_e} + \dot{s}_e - \dot{n}_e s_e \tag{3.8}$$

where $\vec{u_e}$ is electron velocity, T_e is electron temperature, $\dot{s}_e$ is the volumetric entropy production determined from Section 3.2.2, and finally $\vec{q_e}$ is the heat flux. Here, the heat flux term is assumed to consist only of conduction through the electron fluid, and we group all other terms associated with Joule heating, ionization, and wall loss into sources of entropy production. We neglect variations in the radial direction to reduce Eq 3.8 to one-dimensional in $\hat{n}_\perp$. We assume that the heat flux term is primarily axial:

$$\vec{q_e} = -K_{\text{eff}} \nabla T_e \tag{3.9}$$

and express it in terms of the effective thermal conductivity:

$$K_{\text{eff}} = \frac{8 n_e k_B^2 T_e \mu_{\text{eff}}}{\pi e} \tag{3.10}$$

$$= \underbrace{\frac{8 k_B T_e}{m_e \pi}}_{\bar{C}_e^2} \frac{m_e k_B n_e \mu_{\text{eff}}}{e}$$

$$= \frac{m_e k_B \bar{C}_e^2 n_e \mu_{\text{eff}}}{e} \tag{3.11}$$

where $\bar{C}_e$ is the mean speed of electrons.

Entropy Transport Equation 3.8: Convective Derivative

Assuming 1-D entropy flow and a local equilibrium, the entropy per electron, s_e, can be expressed using the Sackur–Tetrode equation [30]:

$$s_\mathrm{e} = \frac{5k_\mathrm{B}}{2} \ln T_\mathrm{e} - k_\mathrm{B} \ln p_\mathrm{e} + k_\mathrm{B} \left\{ \ln \left[\left(\frac{2\pi m_\mathrm{e}}{h^2} \right)^{3/2} k_\mathrm{B}^{5/2} \right] + \frac{5}{2} \right\} + k_\mathrm{B} \ln 2 \qquad (3.12)$$

where h is Planck's constant ($6.62606957 \times 10^{-34} \, \mathrm{m^2 kg/s}$) and the isotropic pressure, p_e is assumed to obey the ideal gas law, $p_\mathrm{e} = n_\mathrm{e} k_\mathrm{B} T_\mathrm{e}$.

Substituting this expression for s_e into the terms of the convective derivative on the left hand side of Eq. 3.8 yields:

$$\begin{aligned}
\frac{\partial s_\mathrm{e}}{\partial t} &= \frac{5k_\mathrm{B}}{2} \frac{\partial \ln T_\mathrm{e}}{\partial t} - k_\mathrm{B} \frac{\partial}{\partial t} \ln \left(n_\mathrm{e} k_\mathrm{B} T_\mathrm{e} \right) \\
&= \frac{5k_\mathrm{B}}{2T_\mathrm{e}} \frac{\partial T_\mathrm{e}}{\partial t} - \frac{1}{n_\mathrm{e} T_\mathrm{e}} \frac{\partial}{\partial t} \left(n_\mathrm{e} k_\mathrm{B} T_\mathrm{e} \right) \qquad (3.13) \\
\frac{\partial s_\mathrm{e}}{\partial \hat{n}_\perp} &= \frac{5k_\mathrm{B}}{2} \frac{\partial \ln T_\mathrm{e}}{\partial \hat{n}_\perp} - k_\mathrm{B} \frac{\partial}{\partial \hat{n}_\perp} \ln \left(n_\mathrm{e} k_\mathrm{B} T_\mathrm{e} \right) \\
&= \frac{5k_\mathrm{B}}{2T_\mathrm{e}} \frac{\partial \ln T_\mathrm{e}}{\partial \hat{n}_\perp} - \frac{1}{n_\mathrm{e} T_\mathrm{e}} \frac{\partial}{\partial \hat{n}_\perp} \left(n_\mathrm{e} k_\mathrm{B} T_\mathrm{e} \right) \qquad (3.14)
\end{aligned}$$

Finally, combining these terms gives the complete left hand side of Eq. 3.8:

$$\begin{aligned}
n_\mathrm{e} \frac{D s_\mathrm{e}}{Dt} &= n_\mathrm{e} \frac{\partial s_\mathrm{e}}{\partial t} + n_\mathrm{e} v_{\mathrm{e},\perp} \frac{\partial s_\mathrm{e}}{\partial \hat{n}_\perp} \\
&= \frac{5k_\mathrm{B} n_\mathrm{e}}{2T_\mathrm{e}} \frac{\partial T_\mathrm{e}}{\partial t} - \frac{1}{T_\mathrm{e}} \frac{\partial}{\partial t} \left(n_\mathrm{e} k_\mathrm{B} T_\mathrm{e} \right) + \frac{5k_\mathrm{B} n_\mathrm{e} v_{\mathrm{e},\perp}}{2T_\mathrm{e}} \frac{\partial \ln T_\mathrm{e}}{\partial \hat{n}_\perp} - \frac{v_{\mathrm{e},\perp}}{T_\mathrm{e}} \frac{\partial}{\partial \hat{n}_\perp} \left(n_\mathrm{e} k_\mathrm{B} T_\mathrm{e} \right)
\end{aligned}$$

$$(3.15)$$

Entropy Transport Equation 3.8: Heat Flux Term

We can expand the first term on the right hand side of 3.8 by substituting in the assumed form of the heat flux (Eq. 3.9):

$$-\nabla \cdot \frac{\vec{q_\mathrm{e}}}{T_\mathrm{e}} = -\frac{1}{T_\mathrm{e}} \nabla \cdot \vec{q_\mathrm{e}} + \frac{\vec{q_\mathrm{e}} \cdot \nabla T_\mathrm{e}}{T_\mathrm{e}^2} \qquad (3.16)$$

$$= \frac{1}{T_\mathrm{e}} \nabla \cdot (K_\mathrm{eff} \nabla T_\mathrm{e}) - \frac{K_\mathrm{eff} (\nabla T_\mathrm{e})^2}{T_\mathrm{e}^2} \tag{3.17}$$

The first of these terms may be given by:

$$\frac{1}{T_\mathrm{e}} \nabla \cdot (K_\mathrm{eff} \nabla T_\mathrm{e}) = \frac{1}{T_\mathrm{e}} (\nabla K_\mathrm{eff}) \cdot \nabla T_\mathrm{e} + \frac{1}{T_\mathrm{e}} K_\mathrm{eff} \nabla^2 T_\mathrm{e} \tag{3.18}$$

$$= \frac{\partial K_\mathrm{eff}}{\partial \hat{n}_\perp} \frac{\partial \ln T_\mathrm{e}}{\partial \hat{n}_\perp} + \frac{K_\mathrm{eff}}{T_\mathrm{e}} \frac{\partial^2 T_\mathrm{e}}{\partial \hat{n}_\perp^2} \tag{3.19}$$

where we used the relation

$$\frac{\nabla T_\mathrm{e}}{T_\mathrm{e}} = \frac{1}{T_\mathrm{e}} \frac{\partial T_\mathrm{e}}{\partial \hat{n}_\perp} = \frac{\partial \ln T_\mathrm{e}}{\partial \hat{n}_\perp}.$$

Substituting Eq. 3.10 into 3.19 gives:

$$\begin{aligned}
\frac{1}{T_\mathrm{e}} \nabla \cdot (K_\mathrm{eff} \nabla T_\mathrm{e}) &= \frac{\partial \left[\frac{8 n_\mathrm{e} k_\mathrm{B}^2 T_\mathrm{e} \mu_\mathrm{eff}}{\pi e} \right]}{\partial \hat{n}_\perp} \frac{\partial \ln T_\mathrm{e}}{\partial \hat{n}_\perp} + \frac{K_\mathrm{eff}}{T_\mathrm{e}} \frac{\partial^2 T_\mathrm{e}}{\partial \hat{n}_\perp^2} \\
&= \frac{8 k_B^2}{\pi e} \frac{\partial \left[n_\mathrm{e} T_\mathrm{e} \mu_\mathrm{eff} \right]}{\partial \hat{n}_\perp} \frac{\partial \ln T_\mathrm{e}}{\partial \hat{n}_\perp} + \frac{K_\mathrm{eff}}{T_\mathrm{e}} \frac{\partial^2 T_\mathrm{e}}{\partial \hat{n}_\perp^2} \\
&= \left[K_\mathrm{eff} \frac{\partial \ln T_\mathrm{e}}{\partial \hat{n}_\perp} + \frac{m_\mathrm{e} k_\mathrm{B} C_\mathrm{e}^2 n_\mathrm{e}}{e} \frac{\partial \mu_\mathrm{eff}}{\partial \hat{n}_\perp} + \frac{m_\mathrm{e} k_\mathrm{B} C_\mathrm{e}^2 \mu_\mathrm{eff}}{e} \frac{\partial n_\mathrm{e}}{\partial \hat{n}_\perp} + \right] \frac{\partial \ln T_\mathrm{e}}{\partial \hat{n}_\perp} \\
&\quad + \frac{K_\mathrm{eff}}{T_\mathrm{e}} \frac{\partial^2 T_\mathrm{e}}{\partial \hat{n}_\perp^2} \\
&= K_\mathrm{eff} \left(\frac{\partial \ln T_\mathrm{e}}{\partial \hat{n}_\perp} \right)^2 + \frac{m_\mathrm{e} k_\mathrm{B} C_\mathrm{e}^2 n_\mathrm{e}}{e} \frac{\partial \ln T_\mathrm{e}}{\partial \hat{n}_\perp} \frac{\partial \mu_\mathrm{eff}}{\partial \hat{n}_\perp} \\
&\quad + \frac{m_\mathrm{e} k_B C_\mathrm{e}^2 \mu_\mathrm{eff}}{e} \frac{\partial \ln T_\mathrm{e}}{\partial \hat{n}_\perp} \frac{\partial n_\mathrm{e}}{\partial \hat{n}_\perp} + \frac{K_\mathrm{eff}}{T_\mathrm{e}} \frac{\partial^2 T_\mathrm{e}}{\partial \hat{n}_\perp^2} \tag{3.20}
\end{aligned}$$

The second term on the right hand side of Eq. 3.17 is simply,

$$-\frac{K_\mathrm{eff} (\nabla T_\mathrm{e})^2}{T_\mathrm{e}^2} = -K_\mathrm{eff} \left(\frac{\partial \ln T_\mathrm{e}}{\partial \hat{n}_\perp} \right)^2 \tag{3.21}$$

Combining the results Eq. 3.20 and Eq. 3.20 gives a simplified form of the heat

flux term:

$$-\nabla \cdot \frac{\vec{q_e}}{T_e} = \frac{m_e k_B C_e^2 n_e}{e} \frac{\partial \ln T_e}{\partial \hat{n}_\perp} \frac{\partial \mu_{\text{eff}}}{\partial \hat{n}_\perp}$$
$$+ \frac{m_e k_B C_e^2 \mu_{\text{eff}}}{e} \frac{\partial \ln T_e}{\partial \hat{n}_\perp} \frac{\partial n_e}{\partial \hat{n}_\perp} + \frac{K_{\text{eff}}}{T_e} \frac{\partial^2 T_e}{\partial \hat{n}_\perp^2} \qquad (3.22)$$

where the second order derivative of T_e can be expressed as

$$\frac{\partial^2 T_e}{\partial n_\perp^2} = T_e \left(\frac{\partial \ln T_e}{\partial \hat{n}_\perp} \right)^2 + \frac{T_e \partial^2 \ln T_e}{\partial n_\perp^2} \qquad (3.23)$$

Finally, the first term on the right hand side of the entropy equation (3.8) becomes:

$$-\nabla \cdot \frac{\vec{q_e}}{T_e} = \frac{m_e k_B C_e^2 n_e}{e} \frac{\partial \ln T_e}{\partial \hat{n}_\perp} \frac{\partial \mu_{\text{eff}}}{\partial \hat{n}_\perp}$$
$$+ \frac{m_e k_B C_e^2 \mu_{\text{eff}}}{e} \frac{\partial \ln T_e}{\partial \hat{n}_\perp} \frac{\partial n_e}{\partial \hat{n}_\perp} + K_{\text{eff}} \left[\left(\frac{\partial \ln T_e}{\partial \hat{n}_\perp} \right)^2 + \frac{\partial^2 \ln T_e}{\partial n_\perp^2} \right] \qquad (3.24)$$

Entropy Transport Equation 3.8: Final Steps

We combine all the derived expressions above with the entropy production term modeled in Section 3.2.2 to arrive at a new form for Eq. 3.8. For a simplified case of steady-state conditions, Eq 3.8 further reduces to the following equation:

$$\frac{3 k_B n_e v_{e,\perp}}{2} \frac{d \ln T_e}{d \hat{n}_\perp} - k_B v_{e,\perp} \frac{d \ln n_e}{d \hat{n}_\perp}$$
$$= \frac{m_e k_B C_e^2 n_e}{e} \frac{\partial \ln T_e}{\partial \hat{n}_\perp} \frac{\partial \mu_{\text{eff}}}{\partial \hat{n}_\perp}$$
$$+ \frac{m_e k_B C_e^2 \mu_{\text{eff}}}{e} \frac{\partial \ln T_e}{\partial \hat{n}_\perp} \frac{\partial n_e}{\partial \hat{n}_\perp} + K_{\text{eff}} \left[\left(\frac{\partial \ln T_e}{\partial \hat{n}_\perp} \right)^2 + \frac{\partial^2 \ln T_e}{\partial n_\perp^2} \right]$$
$$+ k_B n_e \omega_{\text{ce}} B^2 \mu_{\text{eff}}^2 + \dot{n}_e s_e \qquad (3.25)$$

Recall the relation between electron velocity and effective mobility (Eq. 2.21)

derived in Section 2.5.3 and rearrange it as follows:

$$\text{Eq. 2.21: } v_{e,\perp} = -\mu_{\text{eff}} \left(E_\perp + \frac{k_B T_e}{e n_e} \frac{\partial n_e}{\partial \hat{n}_\perp} + \frac{k_B}{e} \frac{\partial T_e}{\partial \hat{n}_\perp} \right)$$

$$\Rightarrow v_{e,\perp} = -\mu_{\text{eff}} \frac{k_B T_e}{e} \left(\frac{e E_\perp}{k_B T_e} + \frac{d \ln n_e}{d \hat{n}_\perp} + \frac{d \ln T_e}{d \hat{n}_\perp} \right) \tag{3.26}$$

Finally, by substituting $v_{e,\perp}$ from Eq. 3.26, the entropy transport equation 3.25 is reduced to the following first-order ordinary differential equation (ODE) for μ_{eff} where properties are assumed to vary mainly along the direction normal to the magnetic contour.

$$\frac{8}{\pi} \frac{k_B T_e}{e} \frac{\partial \ln T_e}{\partial \hat{n}_\perp} \frac{d\mu_{\text{eff}}}{d \hat{n}_\perp} + \frac{e B^3}{m_e} \mu_{\text{eff}}^2 + \beta \, \mu_{\text{eff}} - \frac{\dot{n}_e s_e}{k_B n_e} = 0. \tag{3.27}$$

Here, $\dot{n}_e$ is the ionization rate, q_{ew} is heat flux to the wall, and L is the contour length. The coefficient β in Eq. (3.27) is

$$\beta = \frac{k_B T_e}{e} \left[\frac{eE}{k_B T_e} + \frac{d \ln n_e}{d \hat{n}_\perp} + \frac{d \ln T_e}{d \hat{n}_\perp} \right] \left[\frac{3}{2} \frac{d \ln T_e}{d \hat{n}_\perp} - \frac{d \ln n_e}{d \hat{n}_\perp} \right]$$

$$+ \frac{8}{\pi} \frac{k_B T_e}{e} \left[\frac{d \ln T_e}{d \hat{n}_\perp} \frac{d \ln n_e}{d \hat{n}_\perp} \right.$$

$$\left. + \left(\left(\frac{d \ln T_e}{d \hat{n}_\perp} \right)^2 + \frac{d^2 \ln T_e}{d \hat{n}_\perp^2} \right) \right]. \tag{3.28}$$

Entropy Wall Loss

Underestimating the energy loss to the Hall thruster walls is a possible source of error expected from the 1-D approximation of Eq. 3.27. Because the heat is transferred radially, this approach is unable describe the entropy produced by such an energy transfer. To be consistent with the energy transport equation of electrons (Eq. 2.14) which also assumes one-dimensional transport of energy, we do not consider expanding the model into 2-D. Instead, we take the similar approach to that shown in section 2.5.5 by including the estimated energy transfer of bulk electrons to the channel walls into our 1-D model.

Thus, we introduce an entropy term Eq. 3.27 to account for energy loss to the channel walls. We approximate the entropy wall loss $-\nabla_{\hat{n}_\parallel} q_w$ as follows:

$$-\nabla_{\hat{n}_\parallel} q_w \approx -\frac{q_w}{L} \tag{3.29}$$

where L is the length of the magnetic contour, and the energy loss to the walls q_w is modeled with the same approach used for deriving the electron energy density loss, Γ_w (Eq. 2.29), as follows.

$$\frac{q_w}{L} = \Gamma_e \left[2k_B T_e + e\phi_w - \bar{\sigma} e\phi_w - 0.57 \times 0.6 \times 2k_B T_e \right] \tag{3.30}$$

$$= (1 - \bar{\sigma})\Gamma_i \left[e\phi_w(1 - \bar{\sigma}) + 2k_B T_e(0.658) \right], \tag{3.31}$$

where $\bar{\sigma}$ is the electron emission yield [31] assuming alumina walls, Γ_i is the ion flux to the walls, and the sheath potential is given from Eq. 2.31:

$$\phi_w = \begin{cases} \frac{k_B T_e}{e} \ln\left[(1 - \bar{\sigma})\sqrt{\frac{m_i}{2\pi m_e}}\right] & (\sigma < 0.98) \\ 1.02\frac{k_B T_e}{e} & (\sigma \geq 0.98) \end{cases}$$

Adding the wall loss term (3.31) to the equation 3.27 yields:

$$\frac{8}{\pi} \frac{k_B T_e}{e} \frac{\partial \ln T_e}{\partial \hat{n}_\perp} \frac{d\mu_{eff}}{d\hat{n}_\perp} + \frac{eB^3}{m_e} \mu_{eff}^2 + \beta \mu_{eff} - \frac{\dot{n}_e s_e}{k_B n_e} - \frac{q_{ew}}{L k_B T_e n_e} = 0. \tag{3.32}$$

Later in this chapter, we examine the effect of the wall loss term by comparing the simulated results using Eq. 3.27 to those using 3.32.

3.2.4   Implementation Methodology

Reduction to a Quadratic Equation

There are several possible approaches for including Eq. 3.27 in the hybrid simulation. In this study, we choose to solve a quadratic equation for μ_{eff} at each time step by setting the first order derivative, $\frac{d\mu_{eff}}{d\hat{n}_\perp}$, to a constant equal to that determined by the previous time step. Then the roots of the following quadratic equation can be

explicitly calculated:

$$\frac{eB^3}{m_e}\{\mu_{\text{eff}}^{(i)}\}^2 + \beta\{\mu_{\text{eff}}^{(i)}\} + \underbrace{\left[\frac{8}{\pi}\frac{k_B T_e}{e}\frac{\partial \ln T_e}{\partial \hat{n}_\perp}\frac{d\{\mu_{\text{eff}}^{(i-1)}\}}{d\hat{n}_\perp} - \frac{\dot{n}_e s_e}{k_B n_e}\right]}_{\text{constant coefficient}} = 0. \qquad (3.33)$$

Here, we take only the positive (+) root to maintain a positive electron mobility. With this numerical strategy, we benefit in two ways. First, the computational cost is significantly reduced, because we avoid iterating for the solution at every node at every time step. Second, and more importantly, we avoid the challenging singularity problem that is caused by the structure of the coefficient of the first order derivative of μ_{eff}. The analysis of Ref. [32] shows that the contribution to the resulting mobility from the first order derivative term is small, justifying this approach.

Note that numerical errors may invite unrealistic negative or imaginary roots, especially when the simulation is going through a transient state. Although this case is rare for a stable simulation of the SHT, whenever an unrealistic root might be calculated for $\{\mu_{\text{eff}}^{(i)}\}$, we assume a conditional steady-state for the problematic node and use the mobility from the previous step $\{\mu_{\text{eff}}^{(i-1)}\}$ instead.

Eq. (3.27) is solved along the centerline of the radial dimension and the solution is used as a representative value at each axial position for the purposes of both numerical stability and cost efficiency. The derivatives of the logarithms of electron temperature and density($\frac{d \ln T_e}{d\hat{n}_\perp}, \frac{d \ln n_e}{d\hat{n}_\perp}$) are calculated using a second order Euler's scheme at each time step, using the computed data from the previous time step.

Numerical Adjustments

Numerical adjustments were adopted after a series of preliminary runs with the entropy closure model in order to enhance its stability. These include attention to the region close to the anode when using the effective mobility calculated by Eq. 3.27. In our current version of this hybrid simulation, the computational grid near the anode is not well resolved due to small variations in the magnetic field in this region. This leads to a numerical instability which can be avoided by enforcing the classical mobility in that region (axial position less than 0.02 m). In the rest of the domain,

the computed mobility is introduced gradually at each time step, with 10% of the instantaneously computed mobility at each timestep added to 90% of the mobility used in the previous timestep. The instantaneously computed mobility is also filtered by local averaging to reduce high frequency spatial noise.

3.3   Simulation Results: Stanford Hall Thruster

3.3.1   Nominal Operating Conditions

A representative example of the entropy closure model performance in the hybrid simulation for the SHT is shown in Fig. 3.1 – 3.2. The nominal operating condition for the SHT is a discharge voltage of 200 V and a xenon mass flow rate of 2 mg/s. The time-averaged profiles of the inverse Hall parameter are compared with the experimentally measured data, a Bohm-type model, and the transport computed based on classical scattering. The calculated electron transport using the entropy closure model captures the transport barrier, albeit weakly, near the exit plane (where the axial position is 0.08 m) and agrees reasonably well with that measured at axial positions between 0.02 to 0.04 m and outside the channel (axial position greater than 0.08 m).

Figure 3.2 compares the simulated axial potential, ion velocity, electron temperature, and plasma density profiles to those measured experimentally. The entropy closure model predicts the potential drop in the acceleration region to be more gradual than that seen in the experimental measurements. This is consistent with the weaker transport barrier generated using the entropy closure model. The overestimation of the effective mobility in the Hall region (near axial position of 0.08 m) seems to also enhance the model-simulated electron temperature by approximately 50% higher at the peak than those measured experimentally. However, the location of this computed peak is closer to the peak location measured measured experimentally than is the peak location computed using the Bohm model. Due to the enhanced electron temperature, the model-simulated plasma density is also higher than measured data. The entropy model prediction for the axial ion velocity is in remarkably good
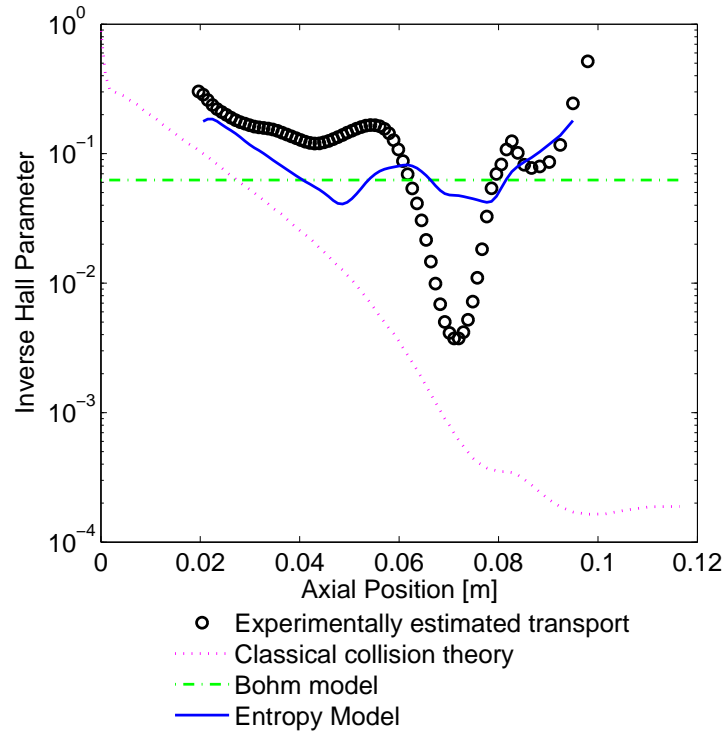
Figure 3.1: Time-averaged inverse Hall parameter computed using the entropy closure model (red solid line) and compared to: (i) experimentally measured values (open circles), (ii) values based on a Bohm model (blue dashed line), and (iii) the computed value using classical theory (red dotted line). The discharge voltage is 200 V. Background gas is not accounted for in these simulations. Xenon mass flow of 2 mg/s are used for all cases.
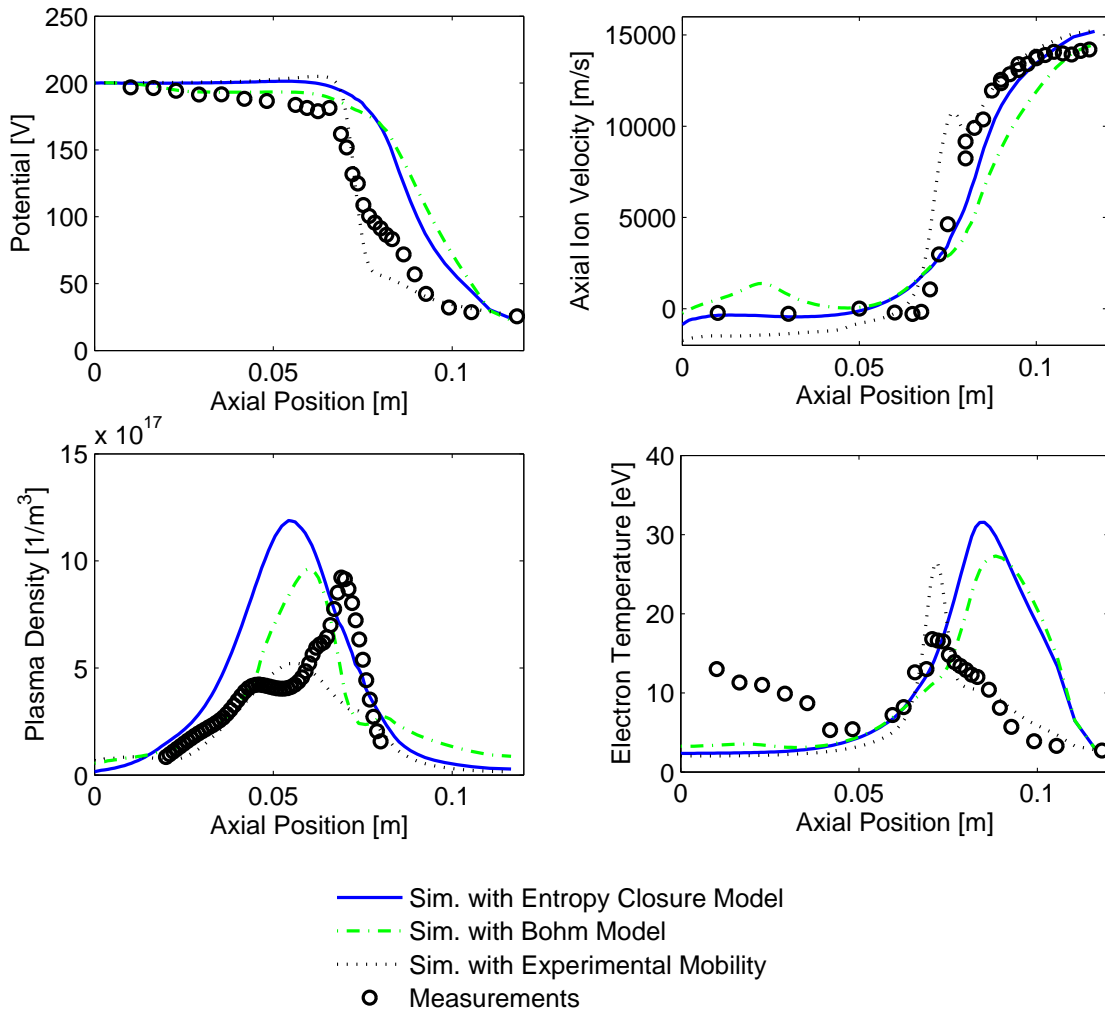
Figure 3.2: Simulated plasma properties using the entropy model compared to experimental measurements and simulated results using the Bohm model and the experimental mobility. The discharge voltage is 200 V and the mass flow rate is 2 mg/s.

agreement with the measurements, especially at the axial location between 0.03 and 0.1 m, when compared to the simulated results using other transport models such as the experimental mobility and Bohm mobility. This is encouraging, considering that the ion velocity measurements carry some of the smallest experimental uncertainty.

3.3.2   Discharge Voltage Variation
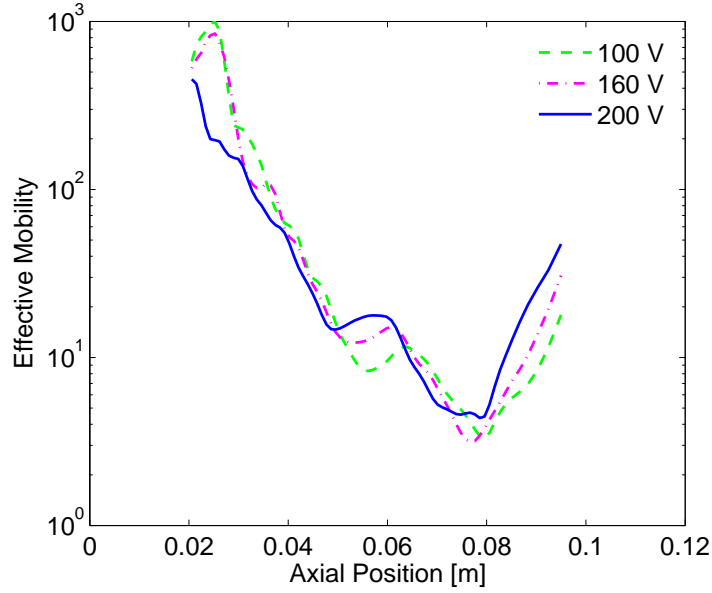
Figure 3.3: A comparison of the simulated mobility using the entropy model at various discharge voltages. The effects of background gas are not included. A xenon mass flow of 2 mg/s is used for all cases.

Discharge voltages other than the nominal 200 V are investigated in order to study the transportability of the closure model. The computed effective mobility for discharge voltages of 100 V, 160 V, and 200 V are compared in Fig. 3.3 which indicates that the mobility calculated with the entropy closure model does not substantially vary with discharge voltage. This is despite the fact that the calculated plasma properties (and their spatial variation) do seem to vary, albeit weakly, with the change in discharge voltage. This is expected from the nature of the derived mobility equation (Eq. 3.27 – 3.28) because the effective mobility depends on the logarithms of plasma

density and electron temperature. This result suggests that for any given thruster, it may be possible to find a universal curve (for a given magnetic field configuration) that captures the general transport behavior. Such a universality is embedded in the Bohm model description, where the mobility is inversely proportional to the magnetic field through a constant of $O(0.05)$ [12].
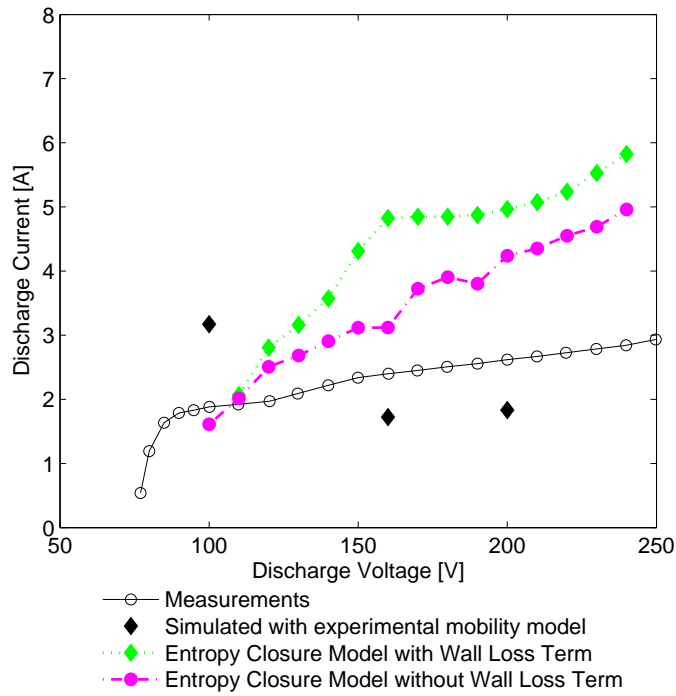
Figure 3.4: Comparison of discharge voltage and current characteristics. The xenon mass flow is 2 mg/s.

Figure 3.4 compares the I-V characteristic computed by the entropy closure model to that measured experimentally, as well as that computed using the experimentally measured mobility. Although the simulated discharge current is generally higher than the measurements ($\circ$), it is noteworthy that the I-V characteristic predicted by the entropy closure model shows a trend similar to that obtained in the experiments. This trend is not seen when the measured mobility is used in the simulations (diamonds), particularly for the low discharge voltage cases.

Effect of Entropy Wall Loss

Inclusion of the heat conduction wall loss in the entropy model seems to increase, although weakly, the resulting entropy production and enhance the computed electron transport in regions of the plasma near the exit plane (see Fig. 3.5). This slight difference in the computed effective mobility seems to be related to the reason why the results with varied discharge voltages are not so different. However, the wall loss term increases the computed discharge currents by 1 to 2 amps, as shown in Fig. 3.4. Increased entropy production is expected for the case with wall loss effects to compensate for the entropy lost to the wall.
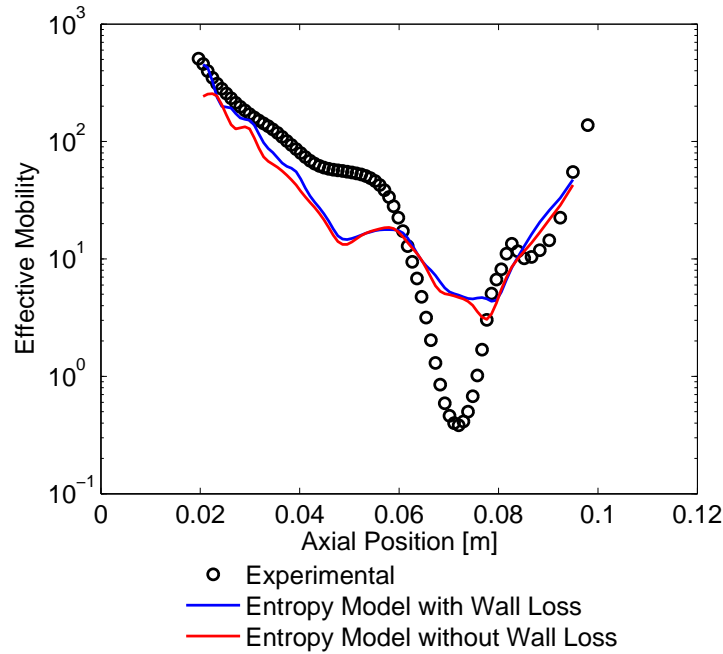
Figure 3.5: Effective electron mobility simulated using the entropy model (with and without the wall loss contribution) are compared to the experimentally measured mobility. Background gas is not included. A discharge voltage of 200 V and xenon mass flow of 2 mg/s are used for all cases.

3.4   Discussion

Although the SHT simulation results with the entropy closure model do not perfectly agree with the experimental measurements, the implementation of the entropy closure model has contributed to our knowledge of Hall thruster simulations in the following ways.

First, the results suggest that the inclusion of an entropy equation into hybrid particle-in-cell (PIC) simulations of Hall thruster, even in a simplified 1-D form, is a reasonable approach to describe electron cross-field mobility within the simulation. Second, the form of the entropy production chosen as an inverse linear function of the effective electron mobility (Eq. 3.4) fails to capture the sharp transport barrier at the Hall region where the magnetic field peaks. To emphasize the effect of the magnetic field on the entropy, higher order polynomial functions of the inverse hall parameter are recommended to replace the linear function. Note that, for example, if a square function of the inverse Hall parameter, $\nu_{\mathrm{eff}}/\omega_{\mathrm{ce}}$, is chosen, the resulting equation for μ_{eff} will be a first-order ODE with a cubic term in μ_{eff}.

Chapter 4

Turbulent Transport Model

4.1 Motivation

The turbulent transport model described in this chapter continues our effort to derive a simple model for the electron mobility that captures relevant physics and is easily integrated into 2-D hybrid simulations with minimal adjustable parameters. Although the entropy closure model in Chapter 3 shows potential as such a model, searching for the dependency function (f in Eq. 3.3) is arbitrary and its implementation is numerically complicated and expensive.

The turbulent transport model was inspired by the entropy closure model when we realized that most of the entropy is produced when the thermal energy is dissipated. The model assumes that the primary means of electron energy dissipation is the turbulent eddy cascade.

The plasma inside the channel and into the near-field plume of Hall thrusters is very turbulent. Early literature described the presence of a wide spectrum of plasma oscillations in Hall thrusters [33]. Studies of plasma density fluctuations inside a thruster using probes show a characteristic energy spectrum over wavenumber scales typical of a turbulent flow [34]. The intensity of this plasma turbulence seems to be related to the measured electron cross-field mobility [11]. Experiments have also reported fluctuations at very high frequencies [35, 36], some with wavelengths smaller

than the gyroradius [36], particularly outside the thruster channel. Correlated fluctuations between plasma density and potential can give rise to cross-field current exceeding that predicted classically. Near the exit plane, where electrons drift azimuthally and ions drift axially, the system can support streaming instabilities [37], resistive instabilities [38, 39], and Rayleigh-Taylor type instabilities [40]. Further upstream into the channel and downstream into the plume, there are strong gradients in plasma density and magnetic field; these gradients can render drift waves unstable [41, 42]. Morozov *et al.* [43] was first to suggest that such instabilities could be relevant to Hall thruster operation in 1973.

4.2   Zero-Equation Model

It is well established from the magnetohydrodynamics (MHD) theory that for a conducting fluid with a very low magnetic Reynolds number $R_\mathrm{m}(= UL/\eta$, where U is a typical velocity scale of the flow, L is a typical length scale and η is the magnetic diffusivity), when the induced magnetic field is negligible compared to the imposed field, the kinetic energy of particles is converted into heat via Joule dissipation [44].

The turbulence in Hall thruster plasmas is expected to be electrostatic with fluctuations in plasma density and mean velocities accompanied by variations in plasma potential. In discharge plasmas, these fluctuations can be strongly correlated and contribute to anomalous current beyond that expected from classical scattering mechanisms. We imagine that electrons migrating from the cathode to the anode will eventually convert their energy into electrostatic fluctuations. Those electrons may also scatter from these fluctuations, depleting their kinetic energy and converting it to thermal energy. In essence, this dissipative mechanism is analogous to electron Joule heating. In our modeling, we treat this process as the dominant mechanism for electron thermalization.

The zero-equation model proposed here attempts to describe this energy dissipation with a plausible assumption that the rate at which large-scale aspects of turbulence (large eddies) supply energy to the small eddies is proportional to the reciprocal

of a time scale τ which characterizes the turbulence [45]. Because the amount of kinetic energy per unit mass in the large-scale turbulence is proportional to u^2, the rate of energy supplied to the small-scale eddies is of order $\left(\frac{1}{\tau}\right) \cdot u^2$, where u is the velocity variation of the turbulent eddies (relative to the mean flow). Note that the time scale τ can be scaled as the ratio of a characteristic length scale l to a velocity scale, i.e., $\tau \sim \frac{l}{u}$. Hence, the specific kinetic energy dissipation rate scales as follows. [46]

$$\varepsilon \sim \frac{u^3}{l} \tag{4.1}$$

Introducing a parameter referred to as turbulent viscosity, ν_{turb}, the scaling of which follows the early work of Prandtl as $u \cdot l$ [47], the dissipated energy rate per unit mass can be expressed as:

$$\varepsilon = \nu_{\text{turb}} \left(\frac{u}{l}\right)^2 \tag{4.2}$$

Here, the term in parentheses (u/l) represents the spatial variation of the turbulent velocity field and is indicative of the eddy turnover rate.

The turbulent viscosity is scaled based on an analogy with kinetic theory, sharing the same dimension as kinematic viscosity (length^2/time). Here, we assume that the largest eddies might scale as the local electron gyroradius, ρ_{e} $(= \frac{\bar{C}_{\text{e}}}{\omega_{\text{ce}}})$, which is about 0.1 mm to 1 mm in the channel of a Hall thruster at the peak magnetic field of 100 G and electron temperature of 20 eV. This is consistent with the scale of the fluctuations in 2-D current distributions seen in the Particle-in-Cell (PIC) simulations of Adam *et al.* [48]. We also assume that the velocity scale for the transport of these eddies is the mean electron speed, $\bar{C}_{\text{e}}$. We then express the turbulent viscosity as:

$$\nu_{\text{turb}} = K\bar{C}_{\text{e}}\rho_{\text{e}} \tag{4.3}$$

where K is a constant that will be derived from experiments. Ideally, the constant K will be transportable to similar Hall discharges, perhaps of differing geometries and operating on different propellants. This constant is the only parameter that must be specified, and we expect it to be of order unity. In the simulations presented here,

K is taken to range from $1/2$ and $1/3$ through $O(1)$. The values for $K = 1/2$ and $K = 1/3$ are inspired from relations derived with a simple kinetic theory [30].

Rather than attempting to scale the eddy turnover rate (u/l) in Eq. 4.2, we assume that electrons are scattered from the fluctuations at a rate equal to $(1/\tau)$. This rate is assumed to be related to the effective electron scattering rate, ν_{eff}, that affects the transport of the electron fluid (Eq. 1.4), as follows:

$$\text{Eq. 1.4} \;\Rightarrow\quad \mu_{\mathrm{eff}} = \frac{\nu_{\mathrm{eff}}}{\omega_{\mathrm{ce}}}\frac{1}{B} \tag{4.4}$$

$$\nu_{\mathrm{eff}} = \mu_{\mathrm{eff}}\omega_{\mathrm{ce}}B \tag{4.5}$$

This assumption states that electron thermal energy is dissipated through viscosity at the effective rate at which electrons scatter off the turbulent eddies. This mechanism for dissipation is assumed to underlie the Joule heating process.

Combining the scaling justified above, $(u/l) \sim \nu_{\mathrm{eff}}$, and Eq. 4.3 yields:

$$\varepsilon = K\bar{C}_{\mathrm{e}}\rho_{\mathrm{e}}\nu_{\mathrm{eff}}^2 \tag{4.6}$$

$$= K\bar{C}_{\mathrm{e}}^2\omega_{\mathrm{ce}}B^2\mu_{\mathrm{eff}}^2 \tag{4.7}$$

This specific energy, ε, is used to form a new expression for the volumetric turbulent energy dissipation rate, ξ:

$$\xi = en_{\mathrm{e}}m_{\mathrm{e}} = Kn_{\mathrm{e}}m_{\mathrm{e}}\bar{C}_{\mathrm{e}}^2\omega_{\mathrm{ce}}B^2\mu_{\mathrm{eff}}^2 \tag{4.8}$$

It is interesting to compare this energy dissipation rate to the entropy production rate for the entropy closure model in Chapter 3. If we assume that irreversibilities in the thruster are entirely due to the turbulent energy dissipation, then the volumetric rate of entropy is simply:

$$\dot{s}_{\mathrm{e,turb}} = \frac{\xi}{T_{\mathrm{e}}} \tag{4.9}$$

Substituting Eq. 4.8 into this expression, we find that:

$$\dot{s}_{e,\text{turb}} = \frac{K n_e m_e \bar{C}_e^2 \omega_{ce} B^2 \mu_{\text{eff}}^2}{T_e}$$

$$= \frac{8 k_B T_e}{m_e \pi} \frac{K n_e m_e \omega_{ce} B^2 \mu_{\text{eff}}^2}{T_e}$$

$$= \left(\frac{8K}{\pi}\right) n_e k_B \omega_{ce} B^2 \mu_{\text{eff}}^2 \tag{4.10}$$

which is equivalent to the entropy source term we modeled with a simple linear function for f in Sec. 3.2.2 expressed as Eq. 3.6. Here, the scaling parameter α from the entropy model is related to K of the turbulent model through $\alpha = (8K/\pi)$.

The volumetric dissipation is equated to the Joule heating term, i.e., $|\vec{J} \cdot \vec{E}|$. Because the electric field is mainly directed in the direction along the thruster channel from the anode to cathode, we can reasonably assume $\vec{J} \cdot \vec{E} \approx J_\perp E_\perp$, where the subscript $\perp$ means the direction perpendicular to the magnetic field lines. Note that this direction effectively aligns with the z – direction along the channel of the Hall thrusters in this study. The electron current density can be expressed in terms of the electron velocity in the perpendicular direction, $u_{e,\perp}$, given by Eq. 2.21 in Chapter 2.

$$J_\perp = e n_e u_{e,\perp} \tag{4.11}$$

$$\text{From Eq. 2.21:} \ u_{e,\perp} = -\mu_{\text{eff}} \left(E_\perp + \frac{k_B T_e}{e n_e} \frac{\partial n_e}{\partial \hat{n}_\perp} + \frac{k_B}{e} \frac{\partial T_e}{\partial \hat{n}_\perp} \right)$$

Then the volumetric rate of Joule heating can be expressed:

$$|\vec{J} \cdot \vec{E}| \approx |J_\perp E_\perp| \tag{4.12}$$

$$= e n_e \mu_{\text{eff}} E_\perp \left(E_\perp + \frac{k_B T_e}{e n_e} \frac{\partial n_e}{\partial \hat{n}_\perp} + \frac{k_B}{e} \frac{\partial T_e}{\partial \hat{n}_\perp} \right) \tag{4.13}$$

Equating this relation to the volumetric energy dissipation rate from Eq. 4.8 yields

an explicit relation for the effective electron mobility, as follows:

$$\xi = |\vec{J} \cdot \vec{E}| \tag{4.14}$$

$$K n_e m_e \bar{C}_e^2 \omega_{ce} B^2 \mu_{eff}^2 = e n_e \mu_{eff} E_\perp \left(E_\perp + \frac{k_B T_e}{e n_e} \frac{\partial n_e}{\partial \hat{n}_\perp} + \frac{k_B}{e} \frac{\partial T_e}{\partial \hat{n}_\perp} \right) \tag{4.15}$$

$$\mu_{eff} = \frac{E_\perp}{K B^3 \bar{C}_e^2} \left(E_\perp + \frac{k_B T_e}{e n_e} \frac{\partial n_e}{\partial \hat{n}_\perp} + \frac{k_B}{e} \frac{\partial T_e}{\partial \hat{n}_\perp} \right) \tag{4.16}$$

More discussion regarding the theoretical rational behind the modeling can be found in Ref. [49].

4.3   Implementation Methodology

Three post-processing steps are applied for the implementation of the proposed model to dampen the numerical instability inherently caused by the perturbation of a dynamic electron mobility updated every ion time step. The post-processing steps include: A) correction at the anode and/or cathode region B) filtering high-frequency spatial noise, and C) temporal relaxation when updating mobility, listed in the order they are processed in the algorithm.

Step A: Anode and Cathode Correction

For all the simulated results presented in this study, the mobility in the anode region (axial position from 0 to about 25 % of the channel length) is assumed to remain constant. In the anode region, Joule heating is insignificant because the plasma density and electric field are much smaller than those at the downstream. Therefore, we can reasonably assume that this region is governed more by classical collision theory than the turbulent transport discussed above. We further assume that this region is less dynamic and fix the mobility to be constant every time step to avoid any numerical instability due to the coarseness of the computational in this region. For SPT simulations, the transport coefficients at the last few grid points near the cathode are also fixed to prevent high amplitude fluctuations because the resolution near the plume is much lower in the current version of the SPT simulation than in

the SHT simulation.

Step B: Local Averaging

The fluid equation solver described in Chapter 2 has a mobility gradient term in the axial (Z) direction. To avoid numerical artifacts, the mobility is locally averaged to have a smooth curve. The mobility calculated from Eq. 4.16 at each node is updated to an averaged value using two adjacent points in Z. Let's call the mobility treated in Step A after calculation using Eq. 4.16 at a certain time step (k), $\mu_{\text{eff,A}}^{(k)}$, and its value at node i, $\mu_{\text{eff,A}}^{(k)}(Z_i)$. This value will either be derived from the turbulent model or and imposed constant near the boundaries, with no guarantee of a continuous gradient. Thus, we update the mobility at each node as follows:

$$\mu_{\text{eff, B}}^{(k)}(Z_i) = \frac{\mu_{\text{eff,A}}^{(k)}(Z_{i-1}) + \mu_{\text{eff,A}}^{(k)}(Z_i) + \mu_{\text{eff,A}}^{(k)}(Z_{i+1})}{3} \tag{4.17}$$

Step C: Temporal Relaxation: Dynamic Rate

Now the mobility, $\mu_{\text{eff,B}}^{(k)}$, calculated and corrected in Steps A and B, is partially introduced into the simulation using a relaxation technique. The fraction by which the instantaneously calculated mobility contributes to the updated mobility is called the "dynamic rate," and the remaining portion is taken from the mobility value used in the previous time step. For example, at the k-th time step of the simulation, if the dynamic rate is 90 %, the mobility to be used in the fluid equations is updated with the following expression:

$$\mu_{\text{eff}}^{(k)} = 0.9\,\mu_{\text{eff, B}}^{(k)} + 0.1\,\mu_{\text{eff}}^{(k-1)} \tag{4.18}$$

For the SHT simulation with xenon propellant, the turbulent transport model performed stably with a dynamic rate as high as 90% for discharge voltages larger than 160 V. The effect of the dynamic rate on the discharge current and the performance of the thruster will be discussed throughout the following section.
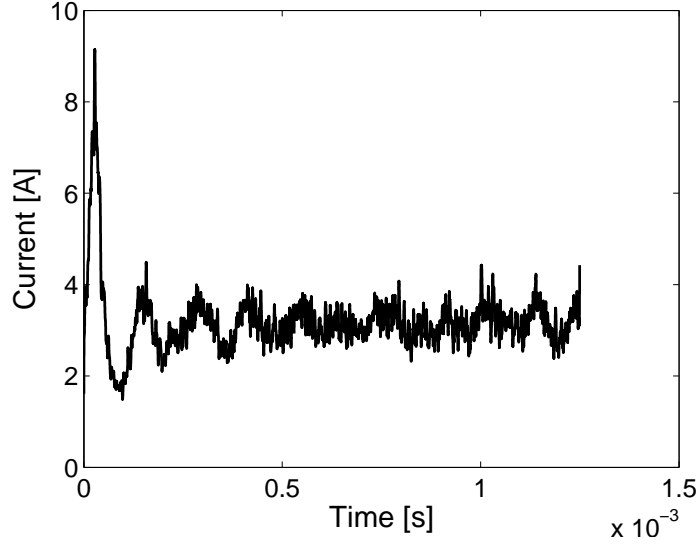
Figure 4.1: Simulated SHT discharge current operating at dynamic rate = 80 %, $K = 1/2$, $V_d = 200$ V, and $\dot{m}_{Xe} = 2$ mg/s.

4.4   Simulation Results: SHT

Nominal conditions for SHT operation are 200 V of discharge voltage (V_d) and 2 mg/s of xenon flow rate ($\dot{m}_{Xe}$). To obtain the simulated current-voltage (I-V) characteristics of the SHT using the proposed model, the discharge voltage is varied from 100 V to 250 V, while the propellant mass flow rate is kept constant.

The time-evolution of the simulated discharge current (I_d) at the SHT nominal condition is presented in Fig 4.1, for which a dynamic rate of 80 % and $K = 1/2$ are used. To exhibit meaningful current oscillations without numerical artifacts due to the high dynamic rate, each data point represents a local average of instantaneous current. After an initial transition period with a high amplitude fluctuation, the current reaches an equilibrium state at about 3 A with a 10 kHz oscillation characteristic of a "breathing mode" instability. The breathing mode is a common instability seen in Hall thrusters with oscillation at a few tens of kHz in the axial direction of the channel [31]. The mechanism behind the breathing mode is related to a fluctuation in the ionization rate of the propellant. When neutral gas fills the channel and is ionized, the ions are accelerated faster than the neutrals are replenished, causing a

decrease in the ionization rate. When the neutral density is recharged by the anode flow, the cycle restarts. R-Z hybrid PIC simulations like ours are known to be capable of capturing the breathing mode [33].

Sensitivity Analysis of Dynamic Rate

As expected, a higher dynamic rate of instantaneous mobility induces a more severe fluctuation in discharge current. It appears that this oscillation is a numerical artifact because it is triggered only by the higher dynamic rate. When the dynamic rate is higher than 50 %, the mobility profile fluctuates more radically from time step to time step, causing the electron current to fluctuate as well. An FFT analysis (Fig. 4.2) of the discharge current oscillation at the various conditions yields two pieces of evidence that support the argument that this MHz-class oscillation is a numerical artifact. First, the peak frequency is linearly dependent on the discrete time step as a given parameter of the simulation. Second, the peak frequency of the oscillation has no correlation with the applied discharge voltage, implying that this MHz oscillation is not a function of the energy of the plasma.

A more interesting finding regarding the dynamic rate is that it affects the time-averaged plasma properties and performance of the simulated thruster as well as the mobility, which will be presented in Sec. 4.4.2 – 4.4.3

4.4.1 Simulated Mobility

Figure 4.3 shows the time-averaged mobility calculated by the turbulent model both (a) over 2-D domain and (b) along the channel centerline. The data shown here is averaged over 1.25 microseconds. It also compares the axial variations estimated by measurements, classical collision theory (Eq. 1.2), and Bohm-type scaling with a Hall parameter of 16 (see Sec. 1.2.2). The experimental mobility was calculated using a simplified relation for electron mobility [11] with measured plasma properties.

Remarkably, the turbulent model captures a transport barrier (dip in 1-D mobility plot) with a location and magnitude similar to that found experimentally, as shown in Fig. 4.3 (b). This transport barrier is where electrons are trapped by the Hall
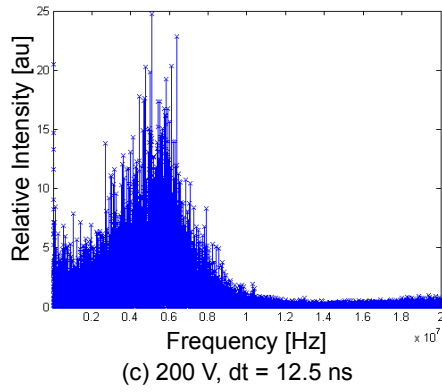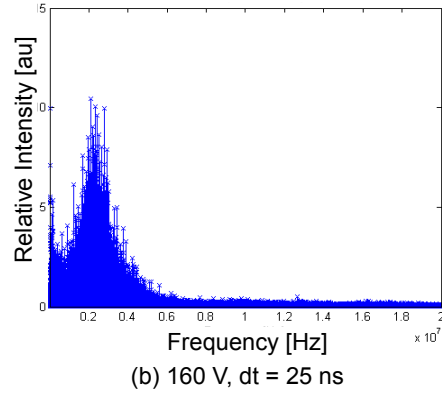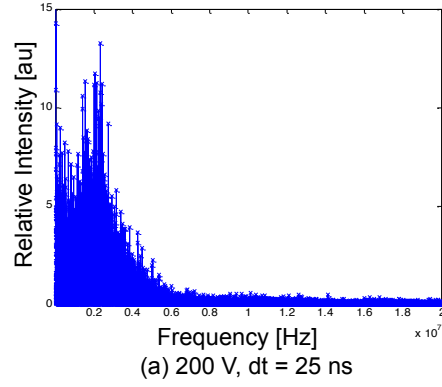
Figure 4.2: Power spectral density analysis of simulated discharge current. (a) Discharge voltage $(V_{\rm d})$ of 200 V and ion time step (dt) of 25 ns. (b) $V_{\rm d} = 160$ V, dt = 25 ns. (c) $V_{\rm d} = 200$ V, dt = 12.5 ns.
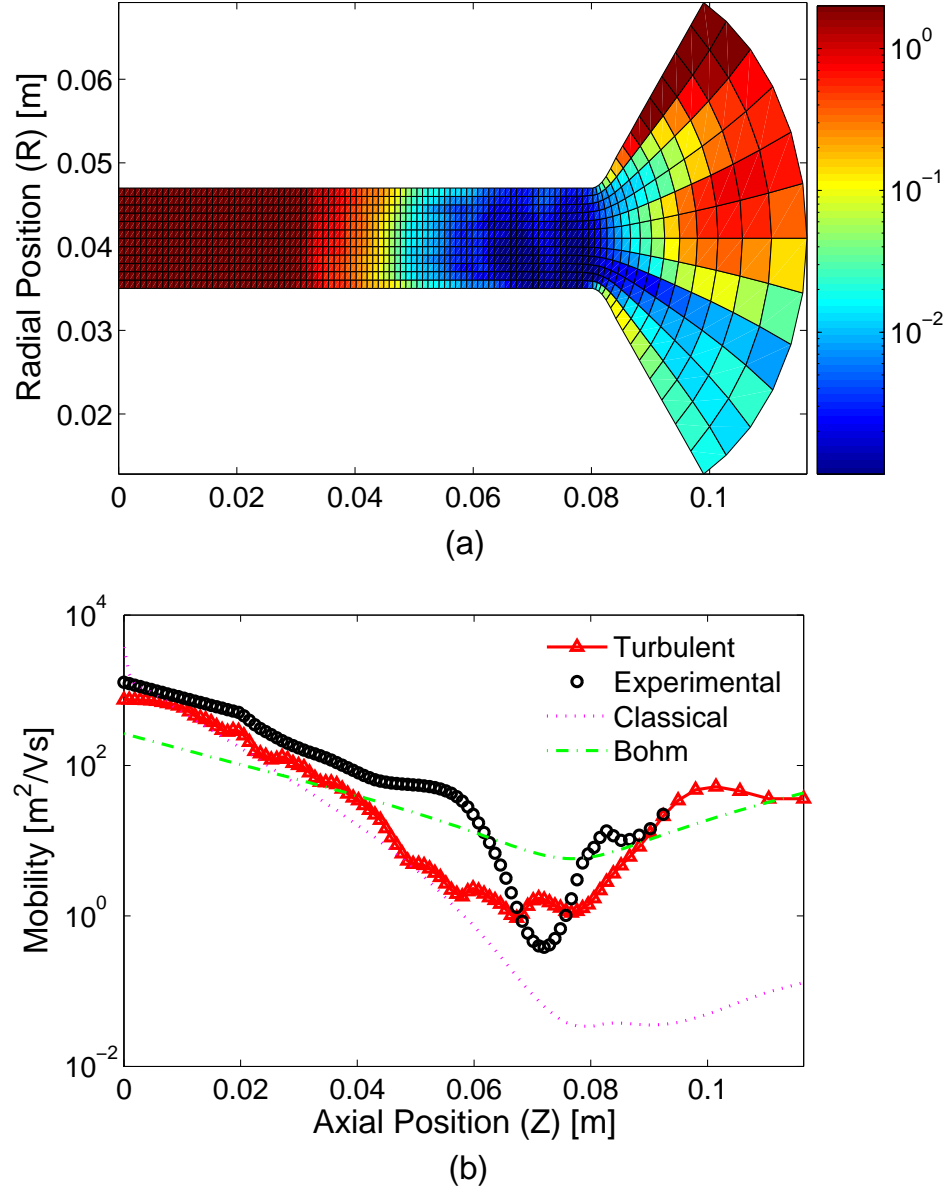
Figure 4.3: Time-averaged mobilities calculated with the turbulent transport model (a) over the full 2-D domain, and (b) along the channel centerline (R = 0.041 m). Dynamic rate = 80 %, $K = 1/2$, $V_d = 200$ V, and $\dot{m}_{Xe} = 2$ mg/s. The channel exit is at Z = 0.08 m. The mobilities calculated using Bohm and classical models are shown for comparison.

current and the majority of ionization takes place, also known as the "Hall region." The width of the transport barrier, however, is wider for the simulated result than the experimental. At the axial positions between 0.02 and 0.06 m, the turbulent model shows agreement with the classical mobility. In general, the proposed model with a parameter $K = 1/2$ which is based on physical intuition [30], outperforms the classical and Bohm-type scaling in reproducing the experimental results.
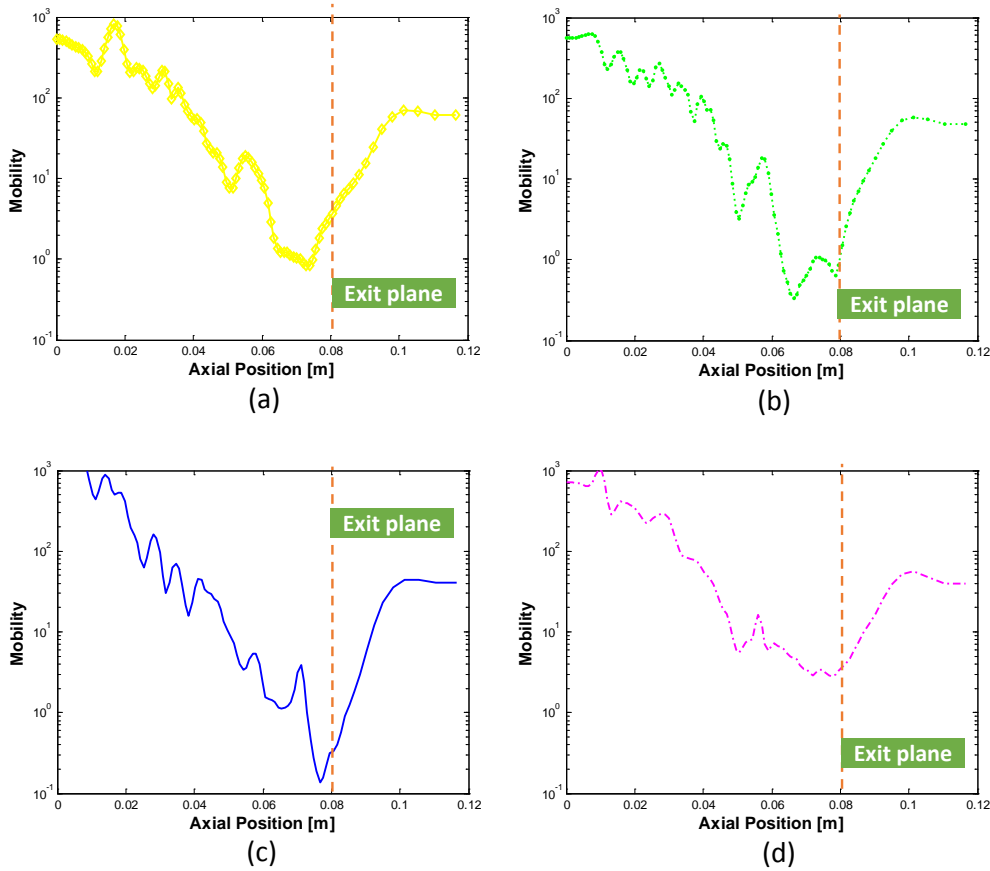
Figure 4.4: Turbulent mobility snapshots at different time steps. Each panel is separated in time by 25 μs. The channel exit is marked at axial position = 0.08 m.

Figure 4.4 features dynamic aspects of the model with snapshots of the turbulent mobility at incremental time steps, from the same simulation results as Fig. 4.3. The snapshots are taken at 25 microsecond intervals. The snapshots suggest that the mobility changes dynamically during the simulation both in the location and
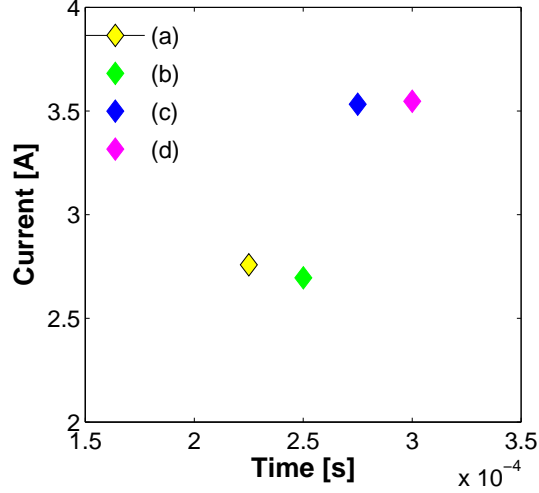
Figure 4.5: Discharge current at each snapshot of Fig. 4.4.

the intensity of the transport barrier. Compared with Fig. 4.3, snapshot (a) shows a remarkable agreement with the experimental mobility. With a reasonably high dynamic rate (50 % or higher), the turbulent transport model is capable of capturing time-varying characteristics of plasma electron mobility in a Hall thruster. Although there exists local numerical noise in the calculated mobility, the location of the Hall region is maintained near the exit plane (axial position of 0.08 m). Figure 4.5 depicts the corresponding discharge current of snapshots (a) – (d) in Fig. 4.4, which provides visual evidence that the electron mobility and the discharge current are closely related within the simulation.

4.4.2 Effect of Dynamic Rate

Accumulated simulation experience suggests that dynamic rate affects the time-averaged mobility in a consistent manner: higher dynamic rate magnifies the transport barrier. Figure 4.6 compares the time-averaged mobility along the channel centerline at dynamic rates of 50 %, 80 %, and 90 %, along with the experimental mobility. For the simulation results shown here, all other conditions are the same as those in the previous section: $K = 1/2$, $V_{\mathrm{d}} = 200$ V, and $\dot{m}_{\mathrm{Xe}} = 2$ mg/s. The transport barrier is most significant at 90 % dynamic rate, although it is split in two.

It is also noteworthy that the simulated mobilities have similar profiles, regardless of the dynamic rate, in regions other than the transport barrier near the channel exit ($Z = 0.08$ m),
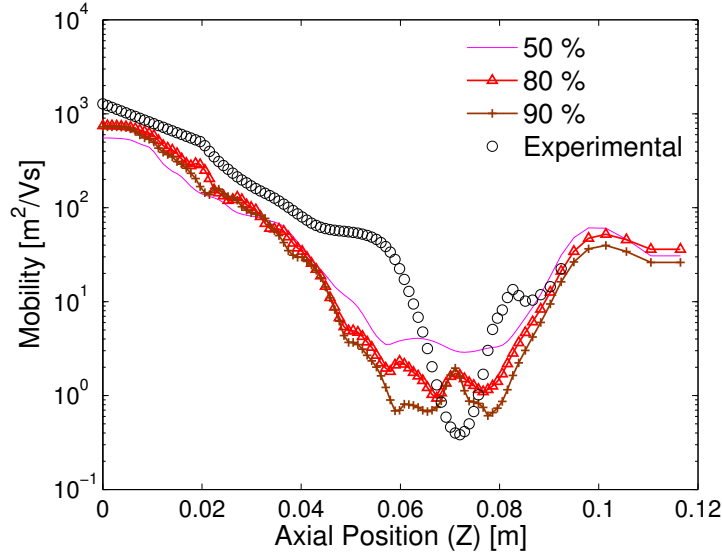
Figure 4.6: Time-averaged mobilities simulated by the turbulent transport model with dynamic rates of 50 %, 80 % and 90 % are compared to experimental mobility (estimated from measured electron velocities in the SHT). $K = 1/2$, $V_{\mathrm{d}} = 200$ V, and $\dot{m}_{\mathrm{Xe}} = 2$ mg/s are used for turbulent models. The channel exit is at axial position = 0.08 m.

Table 4.1: Effect of the dynamic rate on SHT discharge current

Dynamic Rate [%]	$I_{\mathrm{d,mean}}$ [A]
50	4.5
80	3.2
90	2.6

Consequently, the time-averaged discharge current ($I_{\mathrm{d,mean}}$) is lower for a higher dynamic rate, because the lower mobility near the channel exit (Z = 0.08 m) reduces the axial electron current, as shown in Table 4.1.

The dynamic rate also affects the simulated plasma properties, especially the
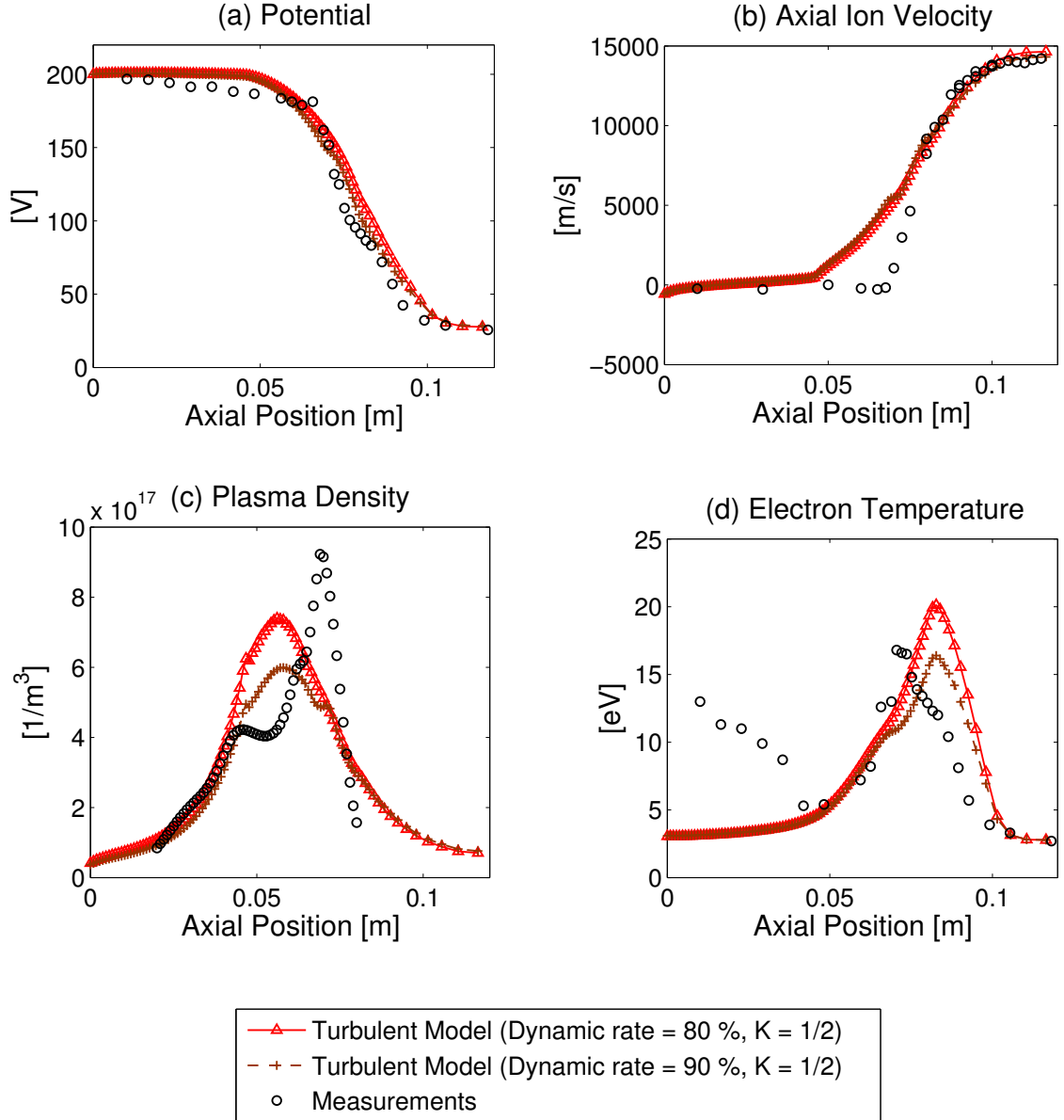
Figure 4.7: Comparison of model-predicted potential, ion velocity, plasma density and electron temperature profiles to the measured data. Dynamic rates of 80 and 90 % are compared. The channel exit is at axial position = 0.08 m.

electron (plasma) density and temperature, as shown in Fig. 4.7. The figure depicts simulated 1-D profiles of electric potential, axial ion velocity, plasma density and electron temperature using 80 % and 90 % dynamic rates and $K = 1/2$. It also provides a comparison with experimental measurements conducted with the prototype SHT. Axial variations of electric potential and axial ion velocity do not seem to vary significantly with respect to the dynamic rate. For both the dynamic rates, electric potential profiles agree remarkably well to the measurements, while axial ion velocity profiles agree only at regions upstream and outside of the channel.

The peak values of electron (plasma) density and temperature, however, are calculated to be higher with 80 % dynamic rate than those with 90 %, which matches the observed discharge current trend. The locations of the peaks of electron density and temperature are similar for both dynamic rates, which are reasonably closer to those of the measurements. The calculated electron peak temperature for the 90 % dynamic rate case is very close to the measured value.

4.4.3   Comparison of I-V Characteristics

The discussion of the impact of the dynamic rate on the model is continued by comparing the simulated current-voltage (I-V) characteristics. In Fig. 4.8, time-averaged discharge current ($I_{d,mean}$) is plotted against applied discharge voltage (V_d) for three combinations of dynamic rates and K. For the cases with 80 % dynamic rate, the simulated discharge currents using the turbulent model seem to be overestimated for most of the V_d range compared with measured currents (black solid line with circles) from the prototype SHT. At a fixed $K = 1/2$, the I-V curve with 90 % dynamic rate has lower mean currents than those with 80 % in most of the V_d range. At a fixed dynamic rate of 80 %, simulated current seems to be inversely proportional to K. The simulated current with 90 % dynamic rate and $K = 1/2$ agrees well with the measurements for V_d near 200 V, the nominal V_d. Assuming higher dynamic rate (ideally 100 %) better reflects the physics behind the turbulent model, this result suggests that $1/2$ for the parameter K might be the value of choice for simulations of the SHT in this V_d range. Transportability of the K value when we implement the

turbulent model into simulations of other thrusters needs further testing. A test on an SPT-100 type thruster simulation with $K = 1/2$ is presented in Sec. 4.5.
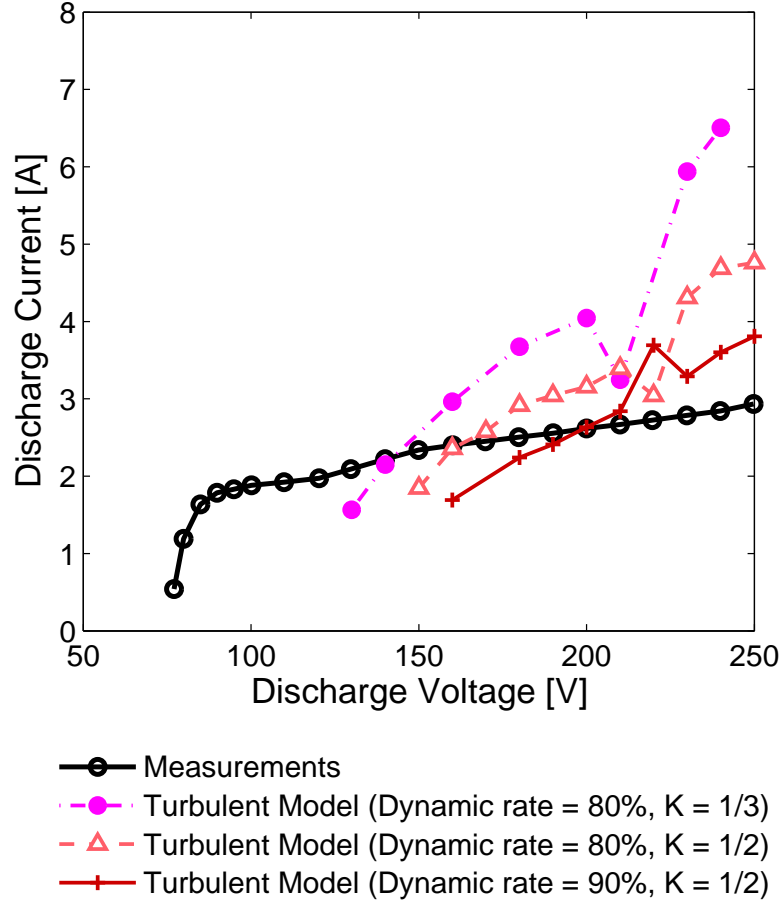

Figure 4.8: Model-predicted current-voltage characteristics of the SHT compared with measured data.

4.5 Application of Turbulent Model to SPT-100

To validate the transportability and utility of the turbulent transport model, we implemented the model on another thruster with different geometry, albeit with similar electromagnetic configuration.

4.5.1   SPT-100-ML

The SHT simulation was modified to have a channel length of 25 mm and outer diameter of 100 mm so that the results could be compared to the wealth of published experimental data [50, 51, 52] on an SPT-100 type thruster (meaning Stationary Plasma Thruster with 100-mm-diameter channel) that is referred to as SPT-100-ML. It is a laboratory thruster manufactured as a part of a French research program, "Plasma Propulsion for Orbital Systems," that involves teams from CNRS, CNES, SEP and ONERA [51]. The design of SPT-100-ML is based on the former USSR's SPT-100 thruster with a flight heritage in the satellite industry [50].

The performance of SPT-100-ML has been tested at the French national facility PIVOINE [53] that was designed and built for the program. Ground tests of the thruster demonstrated 80 mN of thrust, 45 % efficiency, and 1500 s specific impulse when operated at a nominal condition of 300 V of discharge voltage and 5 mg/s of xenon propellant [51]. At the nominal condition, the discharge current at a stable state is reported to be 4.2 A when inner and outer magnetic coils current is set at 4.5 A. Their reports also show that when they changed the magnetic coil current from 2.7 A to 4.5 A, resulting discharge current decreases abruptly from about 6.5 A to 4.2 A. However, when they increased the magnetic current above 4.5 A, the discharge current stays constant near 4.2 A (Fig. 3 in Ref. [51]).

The variations of performance parameters (thrust, specific impulse, and total efficiency) as a function of magnetic current as well as discharge voltage are given in Ref. [51]. At the discharge voltage of 300 V, measured thrust (T) of the SPT-100-ML reads to be approximately between 70 to 90 mN; specific impulse (I_{sp}) and efficiency (η) to be approximately between 1400 to 1650 s and 27 to 53 %, respectively. In this study, we will discuss the simulated results by comparing the experimental data given by Ref. [51]. However, the detailed magnetic field data is not stated in this paper due to the proprietary reason. Therefore, we cannot expect a point-to-point comparison. Instead, we extend the data range for comparison to enclose the whole published range from 2.7 A to 6.3 A for the magnetic currents, assuming the imposed magnetic field in our simulation falls between that range.

4.5.2 SPT-100 Simulation

Thanks to a similar electromagnetic configuration to the SHT, it was straightforward to convert the SHT simulation to model the SPT-100-ML. Because this project to implement the turbulent model for the SPT-100-ML geometry is not a collaboration but rather a simple test, we could only rely on the published data. (Also, we call this model, the SPT-100 simulation, not the SPT-100-ML simulation to avoid any confusion.) Thus, we guess the external magnetic field by emulating a field similar to that of the SHT, relying on the published data by Dorval *et al.* [54] where one-dimensional radial magnetic field strength ($B_{\rm r}$) along the centerline of the channel is available. To emulate the magnetic field, we use Finite Element Method Magnetics, an open source magnetic field solver using finite element methods [55]. The computational grid modified for the SPT-100 is shown in Fig. 4.9 (a). The color in the figure indicates the calculated magnetic field. One can compare this grid to that of the SHT simulation given in Fig. 4.9 (b).

4.5.3 SPT-100 Simulation Results

For the SPT-100 simulation with the turbulent model, the nominal condition is set to 300 V of discharge voltage and 5 mg/s of xenon flow rate to match the standard working condition denoted in [51]. Due to lack of numerical stability, only up to 80 % of dynamic rate is tested with the parameter $K = 1/2$.

The simulated discharge current ($I_{\rm d}$) at the SPT-100 nominal condition is presented in Fig. 4.10, which is post-processed to filter high frequency numerical artifacts with the same method used in Fig. 4.1. The simulated current oscillation agrees well with experiments, corresponding to a mode in between the "fluctuating mode" at 100 V and the "oscillating mode" at 300 V, described in Fig. 6 of Ref. [51].

Time-averaged discharge current, $I_{\rm d,mean}$, however, does not seem to correspond to the reported discharge current measured with the nominal operating condition. The SPT-100 simulation with the turbulent model predicts 6.2 A, while the experimental value is 4.2 A. Perhaps, this discrepancy is caused by the uncertainty of the applied magnetic field in SPT-100 simulation, considering that the discharge current is a
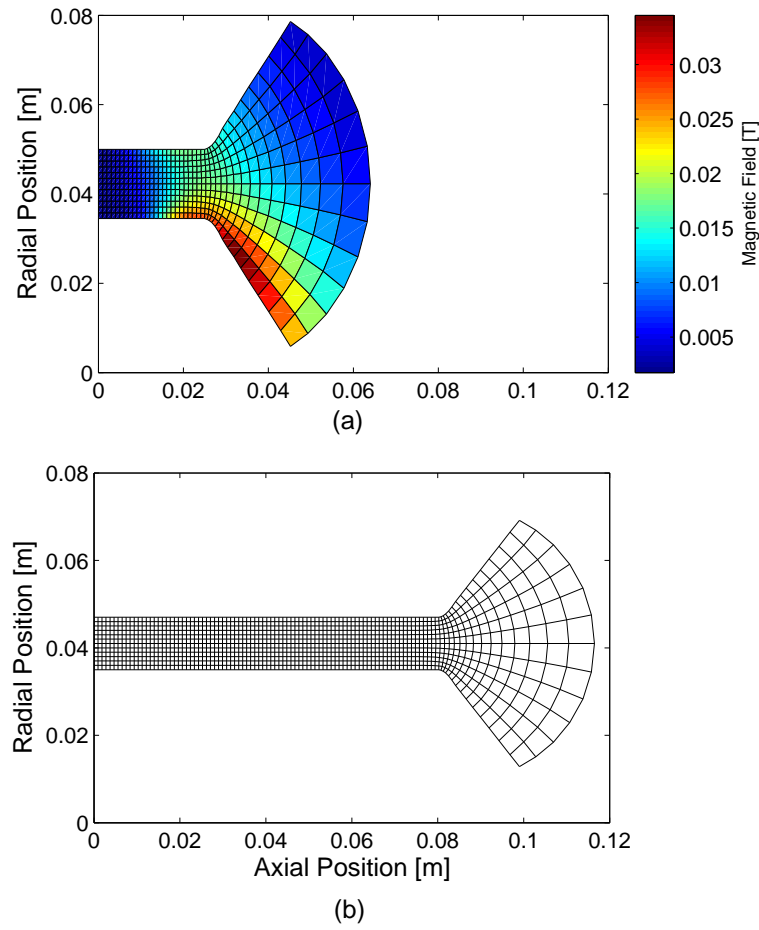
Figure 4.9: The computational domain modified for (a) the SPT-100 simulation with the applied magnetic field overlaid. (b) The domain for the SHT simulation for comparison.
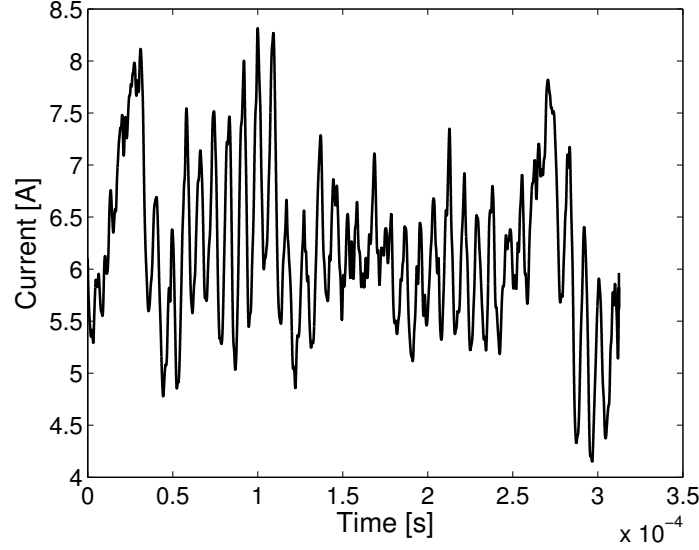
Figure 4.10: Time evolution of simulated discharge current of the SPT-100 operating at dynamic rate = 80 %, $K = 1/2$, $V_d = 300$ V, and $\dot{m}_{Xe} = 5$ mg/s.

strong function of the magnetic coil current, as mentioned previously. Thus, it is still encouraging that the simulated $I_{d,mean}$ is in the range between the maximum and minimum of measurements, as shown in Fig. 4.11. In this figure, experimentally measured discharge currents [51] at 200 and 300 V discharge voltages are compared to the simulated discharge current using the turbulent model. For 200 V, the simulated $I_{d,mean}$ is closer to the measured values with magnetic coil current of 3.6 A, while $I_{d,mean}$ for 300 V is closer to the coil current of 2.7 A.

Similar trends are observed in the performance parameters. Using the same conditions used as Fig. 4.11, the turbulent model predicts the performance parameters – thrust, efficiency, and specific impulse – listed in Table 4.2. The simulated thrust and efficiency are within the range of the experimental values obtained from Ref. [51], although the specific impulse is overestimated for both 200 V and 300 V. Despite the lack of data for verification, the turbulent transport model that was developed on one geometry seems to be easily implemented on another and predicts results similar to experimental measurements.
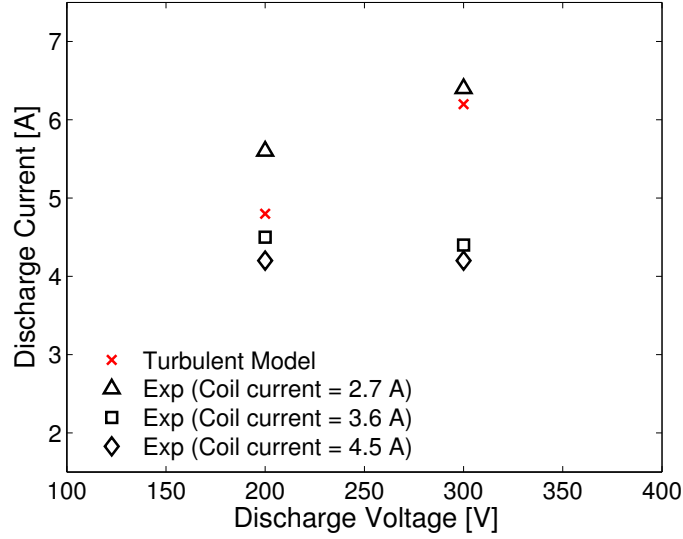
Figure 4.11: Comparison of simulated discharge current of the SPT-100 at $V_d = 200$ and 300 V to experiment measurements of the SPT-100-ML. The turbulent model with $K = 1/2$ is used. 70 % dynamic rate is used for 200 V and 80 % for 300 V.

Table 4.2: Performance estimation of the SPT-100 type thruster using the turbulent transport model compared with experimental data. Thrust, overall efficiency, and specific impulse are compared.

	Turbulent 200 V	Exp. 200 V	Turbulent 300 V	Exp. 300 V
T [mN]	66	$50 - 65$	90	$70 - 90$
η [%]	46	$22 - 38$	45	$27 - 53$
I_{sp} [s]	1348	$900 - 1200$	1833	$1350 - 1650$

Chapter 5

Nitrogen-Fueled Hall Thruster

5.1 Nitrogen (N_2) as an Alternative Propellant

Motivated by the increasing costs of xenon, researchers have sought and tested alternative propellants. The most popular alternatives are among the noble gases, such as argon and krypton [56]. Because they are inert gases as xenon, their chemical characteristics resemble those of xenon; therefore, their replacement of xenon would entail only minor costs in spacecraft requalification. However, the performance of thrusters operated with these replacement propellants is not as desirable as that with xenon.

Some researchers have attempted to find alternative propellants that could meet performance criteria and be cost effective, even if this means that redesign and requalification of Hall thrusters would be more extensive. These researchers have looked at metals, i.e., bismuth [56], zinc, and magnesium [57], as potential alternative propellants. These metals are heavy and easy to ionize, yielding reasonable performance compared to xenon [56]. However, designing thrusters to operate with metals poses several technical challenges; for example, the metal vapor can easily coat the inside of thrusters and adjacent devices, possibly resulting in impaired system reliability [56].

Other groups have focused on molecular gases, i.e., N_2 or O_2, for future applications. Because molecular gases have quite different properties from xenon, it would not be desirable to use them as a replacement for xenon in an existing xenon-propelled

applications. However, the successful implementation of molecular gases into a new Hall thruster design would open up great possibilities for various novel concepts.

One possibility might be a hybrid rocket system that involves a dual-mode propulsion system for deep space exploration. It would consist of a high thrust to power (T/P) option from a chemical combustion rocket, a high specific impulse (I_{sp}) option from a Hall thruster, and shared propellant storage. Because molecular nitrogen (N_2) is a major mass carrier in the by-product of hydrazine (N_2H_4), a common fuel for chemical rockets, a N_2-fueled Hall thruster could be easily integrated into the hybrid concept.

Although there are some research groups that run Hall thrusters on ambient air and molecular oxygen [58], there has been very little reported research on the development of N_2-fueled Hall thrusters. This chapter focuses on the modification of the simulation models previously discussed throughout this thesis to develop a N_2-fueled Hall thruster simulation. Furthermore, optimization of the thruster geometry and its operating conditions are investigated.

Table 5.1: Properties of N_2 and Xe.

Propellant	N_2	Xe
Particle Mass [amu]	28.01	131.29
Ionization Energy [eV]	15.58	12.12
First Excitation [eV]	6.17	8.32
Abundance	79 mol % in air	0.087 ppm in air
Element Type	Molecular gas	Noble gas
State at STP	Gas	Gas
Relative Cost	Not a factor	High

5.2   Chemical Properties of Nitrogen

In this section, the alternative propellant, molecular nitrogen (N_2) is compared to the traditional propellant, xenon. The two important features that cause the nitrogen Hall thruster to behave quite differently from the traditional xenon-propelled Hall thrusters are the lighter propellant mass and the higher ionization energy of N_2,

relative to xenon. As described in Table 5.1, N_2 weighs 28.01 amu, which is about a quarter of the atomic weight of xenon (131.28 amu). Lighter mass potentially extends the operational lifetime of thrusters because the impulse that each impacting particle exerts on the wall of a thruster channel is proportional to the mass times the velocity ($\Delta p \sim mv$). Here, the velocity, v, can be represented by the mean speed, $\bar{C}$, of the particle from the kinetic theory as follows [30]:

$$\bar{C} = \sqrt{\frac{8k_{\mathrm{B}}T}{m\pi}}, \tag{5.1}$$

where k_B is the Boltzmann constant, T is the gas temperature, and m is the particle mass. Thus, the incidental momentum flux per collision from a particle to the channel wall will be reduced by a factor of $\sqrt{\frac{m_{\mathrm{Xe}}}{m_{\mathrm{N_2}}}}$, which is approximately two, if N_2 replaces xenon as a propellant.

However, the transit time of the propellant particle in the thruster channel is shortened due to the lighter mass of the N_2 because the transit time scale, τ, is inversely proportional to the mean speed, $\bar{C}$, i.e., $\tau \sim \frac{L_{\mathrm{C}}}{\bar{C}}$. The reduced transit time (residence time in the channel) reduces the probability of effective collisions that lead to the ionization of the neutral particles. The N_2 propellant is, thus, more difficult to ionize, compared to xenon.

In addition, the higher ionization energy and the molecular structure of N_2 (15.58 eV) makes N_2 more difficult to ionize than xenon. This will be addressed more in detail in the following section.

5.2.1 Ionization Mechanism

As discussed in Chapter 2, the ion particles in the simulation represent the singly charged ions, N_2^+, in this study. The molecular ionization, i.e.:

$$N_2 + e^- \rightarrow {N_2}^+ + 2e^- \tag{5.2}$$

is considered to be the source of ion production. Measured data by Saporoschenko [59] qualitatively supports the assumption that N_2^+ is the dominant species in a nitrogen

Hall thruster. He measured the ionizations in nitrogen gas versus the electron accelerating potential using a mass-spectrometer and observed that the current of N_2^+ ions peaked at the electron energy regime between 16 to 24 eV.

Table 5.2 presents the competing reactions that involve the molecular nitrogen (N_2) or atomic nitrogen (N) as a reactant at the energy regime near 15.58 eV [60]. Molecular ionization of N_2 (reaction 5) requires the least amount of energy (15.58 eV) among the ion-producing reactions of N_2 in the Table 5.2. Atomic ionization (reaction 4) does require less threshold energy (14.55), but it must be preceded by a dissociation that requires another 9.8 eV. The sequential atomic ionization after a dissociation is not only more expensive, but also less probable than the molecular ionization because the propellant transit time τ is relatively short in the Hall thruster channel. Meanwhile, it is reasonable to neglect the dissociative ionization reaction (6) for the simulation because it has a significantly high threshold energy, 24.32 eV which is well above the operating condition of the SHT.

According to the Table 5.2, however, there are many competing reactions that are likely to occur in the nitrogen plasma with threshold energies less than 15.58 eV including the dissociation and excitations. In the model, the energy loss due to those reactions are lumped together for the sake of numerical simplicity. Also, atomic nitrogen (N) is not treated as a tracked species in the simulation. Although excluding N atoms might decrease the accuracy of simulated properties of N_2 neutrals in the ionization zone, the discrepancy is expected to be insignificant in other regions because the atoms are expected to recombine at a substantial rate.

5.3   Implementation to the SHT Simulation

To study the performance of a Hall thruster fueled by N_2, we used the same simulation platform we discussed throughout this thesis. With the same Stanford Hall Thruster (SHT) geometry and the applied magnetic field, the properties of neutrals and ions must be modified to model N_2. In this work, we modified three components in the

Table 5.2: Competing reactions in low temperature N_2 plasma.

Reactions	Threshold [eV]	Description
(1) $e^- + N_2 \rightarrow N_2^* + e^-$	6.17	Excitation (general)
(1a) $e^- + N_2 \rightarrow N_2^*(A^3\Sigma_u^+) + e^-$	6.17	Excitation $(A^3\Sigma_u^+)$
(2) $e^- + N_2 \rightarrow N(^4S) + N(^4S) + e^-$	9.80	Dissociation
(3) $e^- + N_2 \rightarrow N^* + N(^4S) + e^-$	12.14	Dissociative excitation
(3a) $e^- + N_2 \rightarrow N^*(^2D) + N(^4S) + e^-$	12.14	Dissociative excitation
(3b) $e^- + N_2 \rightarrow N^*(^2P) + N(^4S) + e^-$	14.34	Dissociative excitation
(4) $e^- + N \rightarrow N^+ + 2e^-$	14.55	Atomic ionization
(5) $e^- + N_2 \rightarrow N_2^+ + 2e^-$	15.58	Molecular ionization
(6) $e^- + N_2 \rightarrow N^+ + N(^4S) + e^-$	24.32	Dissociative ionization

simulation: (1) the propellant mass, changed from 131.29 amu to 28.01 amu, (2) the ionization rate function, and (3) the ion production cost factor.

5.3.1 Mass Flow Rate

To maintain the same number density of neutral propellants in the thruster channel, the following mass flow rate relation for a propellant, p, is useful to calculate the nominal mass flow rate of N_2:

$$\dot{m}_p = \frac{m_p n_p \bar{C}_p A_C}{4},\tag{5.3}$$

where $\dot{m}$ is the mass flow rate, m is the particle mass, n is the number density, $\bar{C}$ is the mean speed of the particle defined by Eq. 5.1, and A_C is the cross-sectional area of the channel.

Scaling $\dot{m}_{N_2}$ to $\dot{m}_{Xe}$ for the same macroscopic pressure (i.e., the same number density, n) and temperature, T, using Eqs. 5.3 and 5.1 yields:

$$\frac{\dot{m}_{N_2}}{\dot{m}_{Xe}} = \frac{m_{N_2}}{m_{Xe}}\sqrt{\frac{m_{Xe}}{m_{N_2}}} = \sqrt{\frac{m_{N_2}}{m_{Xe}}} = 0.46 \approx 0.5.\tag{5.4}$$

Thus, the N_2 mass flow rate of 1 mg/s would be approximately equivalent to the nominal xenon flow rate of 2 mg/s. However, in preliminary simulations with 1 mg/s

of N_2 mass flow, it was difficult to sustain the plasma due to the lower ionization rates. Instead, 1.5 mg/s and 2 mg/s of N_2 mass flow rate are tested as the operating conditions.

5.3.2   Ionization Rate

The ionization rates are calculated as a function of electron temperature and electron drift velocity assuming a shifted Maxwellian distribution of electrons. The Binary-Encounter-Bethe (BEB) model [22] was used to calculated nitrogen ionization cross-section. The calculated ionization rate of N_2 is compared to the ionization rate of xenon in Fig. 5.1. The ionization rate of N_2 is as low as approximately 40% of the ionization rate of xenon in overall range of the electron temperature.
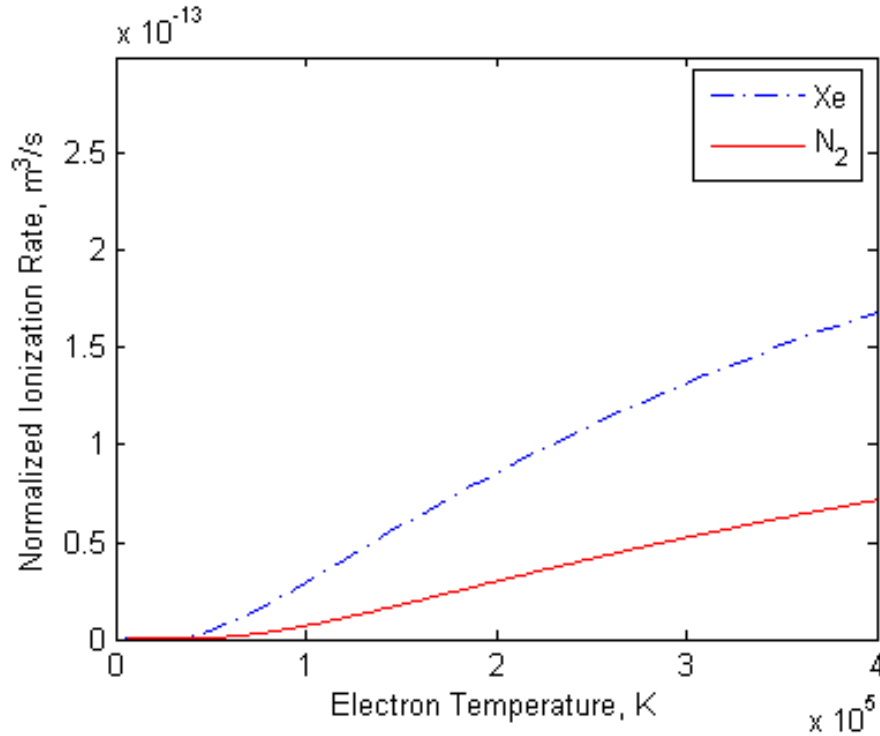

Figure 5.1: Comparison of the direct ionization rates for xenon and N_2.

5.3.3 Ionization Cost

Because nitrogen has a more complex electronic, vibrational, and rotational structure, the ionization cost factor for nitrogen is modeled by an alternative approach, instead of Dugan's method [24] as used for xenon because it accounts for only the first excitation energy. For the N_2 model, the ionization cost (ϕ_c) is defined as the electron energy lost per newly produced electron. It can be related to the Townsend ionization coefficient, α_c, which depends on the reduced electric field, E/n. The ionization cost is given as [61],

$$\phi_c = \frac{E}{\alpha_c} = \frac{E/n}{\alpha_c/n}.$$

(5.5)

The Boltzmann equation solver BOLSIG [62] was used to obtain steady-state values for ϕ_c, for both xenon and N_2, at values of E/n ranging from 10^2 to 10^7 Td (where 1 Td $= 10^{-17}$ V·cm^2) which spans the operating range of the simulation. The ratio of ϕ_c for nitrogen to ϕ_c for xenon is evaluated over this range of E/n, and then multiplied by the ionization cost factor of xenon determined using the method of Dugan *et al.* (depicted in Fig. 2.6) as described in Chapter 2. The ratio $\frac{\phi_{c,N_2}}{\phi_{c,Xe}}$ is plotted in Fig. 5.2, and the sensitivity of the simulation to this multiplication is found to be rather small. The one drawback of this method is that the electron energy distribution used in evaluating the Townsend coefficients does not account for the magnetized nature of the electrons.

5.4 Simulation Results and Discussion

For the initial implementation of nitrogen as an alternative propellant in the SHT (the nitrogen (N_2)-fueled SHT) simulation, same macroscopic conditions are maintained as the nominal xenon operation (the xenon (Xe)-fueled SHT). The discharge voltage (V_d) is 200 V and the imposed magnetic field is also taken to be the same as the Xe-fueled SHT simulation in Chapter 2. For the electron transport, the turbulent transport model discussed in Chapter 4 is used with 50 % dynamic rate and $K = 1/2$.

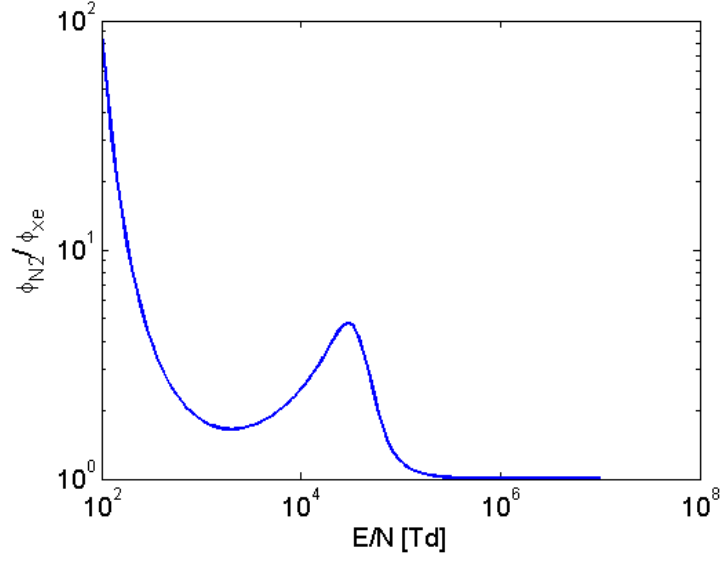Figure 5.3 presents an example of transient behavior of simulated discharge current

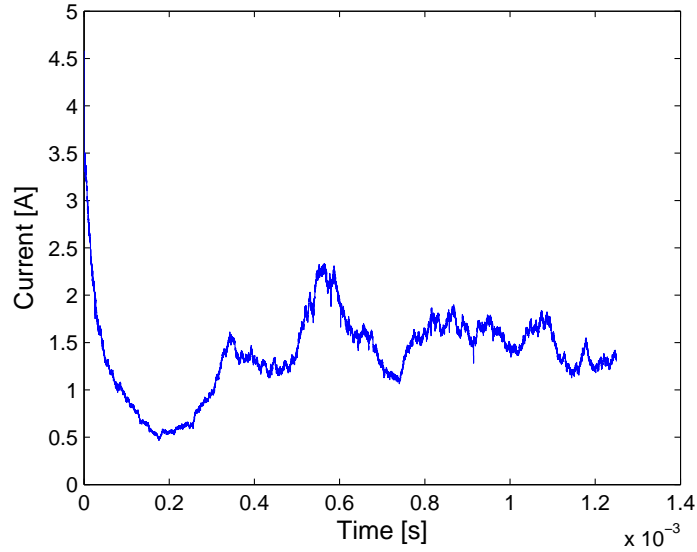Figure 5.2: Ratio of ionization cost of nitrogen to that of xenon.

Figure 5.3: Time evolution of simulated discharge current of the N_2-fueled SHT. V_d = 200 V, and $\dot{m}_{N_2}$ = 1.5 mg/s.

of the N_2-fueled SHT at with 200 V of discharge voltage and 1.5 mg/s of mass flow rate. After a period of transition, the current seems to reach a steady state with a mean current of 1.49 A. A comparison to the nominal case of the Xe-fueled SHT that showed a simulated mean current of 3.2 A (Table 4.1) indicates that the ion flux in the N_2-fueled SHT is much weaker than that in the Xe-fueled SHT.

Hereinafter, the simulated plasma properties of the N_2-fueled SHT at 1.5 mg/s and 2 mg/s mass flow rates are compared with that of the Xe-fueled SHT at the same nominal condition. 200 V discharge voltage and $K = 1/2$ for the turbulent transport model are applied. Note that the simulated plasma properties discussed in this section are averaged over time and radial position.
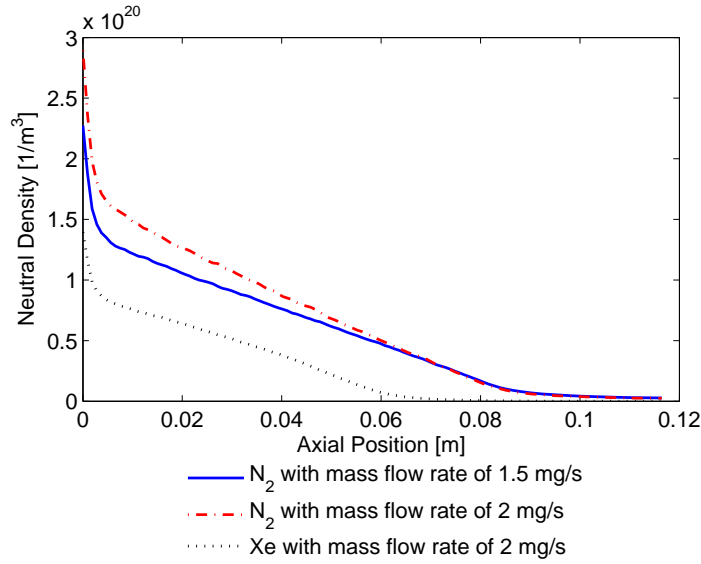
Figure 5.4: Simulated ion velocity of the N_2-fueled SHT at discharge voltage of 200 V.

Figure 5.4 compares the neutral densities along the axial position for the N_2-fueled SHT at 1.5 mg/s and 2 mg/s mass flow rates to that of the Xe-fueled SHT at 2 mg/s. Near the anode (axial position, Z = 0), the number densities of neutrals vary according to their injection rate and particle mass. As the neutrals proceed toward the cathode (Z = 0.12 m), however, the densities of nitrogen neutrals remain at a considerable amount even beyond the exit plane (Z = 0.08 m) as opposed to xenon
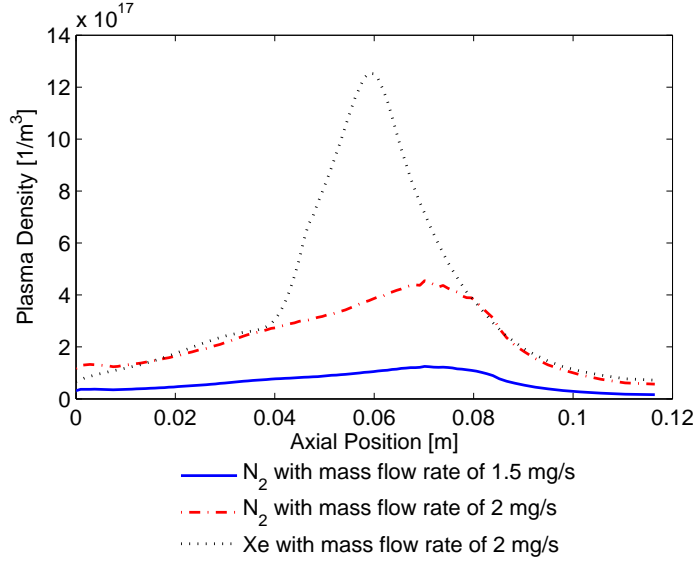
Figure 5.5: Simulated plasma density of the N_2-fueled SHT at discharge voltage of 200 V.

neutrals, most of which are depleted by ionization beyond Z = 0.06 m. This implies the ionizations are less efficient in N_2-fueled SHT than in Xe-fueled SHT, which can also be observed in the comparison of plasma density in Fig. 5.5.

For N_2-fueled SHT, even with the higher 2 mg/s mass flow rate, the peak plasma density is 3 times smaller than the peak plasma density for the Xe-fueled SHT. The consequence of inefficient ionization in a Hall thruster is poor thruster performance. For example, our simulation of N_2-fueled SHT at 1.5 mg/s predicts an estimated thrust of 7 mN, efficiency (η) of 5 %, and specific impulse (I_{sp}) of 450 s, whereas Xe-fueled SHT is predicted to produce thrust of 28 mN, efficiency of 23 %, and specific impulse of 1446 s. See Table 5.3.

Figure 5.6-5.7 present the effect of the lighter mass of nitrogen. Compared to the axial ion velocity for xenon, N_2^+ is faster by a factor of about 2 near the axial position 0.12 m, where the factor of 2 corresponds to the square root of the mass ratio, $\sqrt{m_{\mathrm{Xe}}/m_{N_2}} \approx 2$. Propellant mass flow rate does not affect the axial velocity of ions. However, the higher mass flow rate slightly increases the velocity of neutrals,

Table 5.3: Performance summary for N_2-fueled SHT compared with Xe-fueled SHT. Discharge voltage is 200 V.

Propellant	Mass Flow [mg/s]	Thrust [mN]	Efficiency, η [%]	Specific impulse, I_{sp} [s]
N_2	1.5	7	5	450
	2	21	11	1054
Xe	2	28	23	1446

because of the increased pressure gradient due to the higher number density at the upstream.
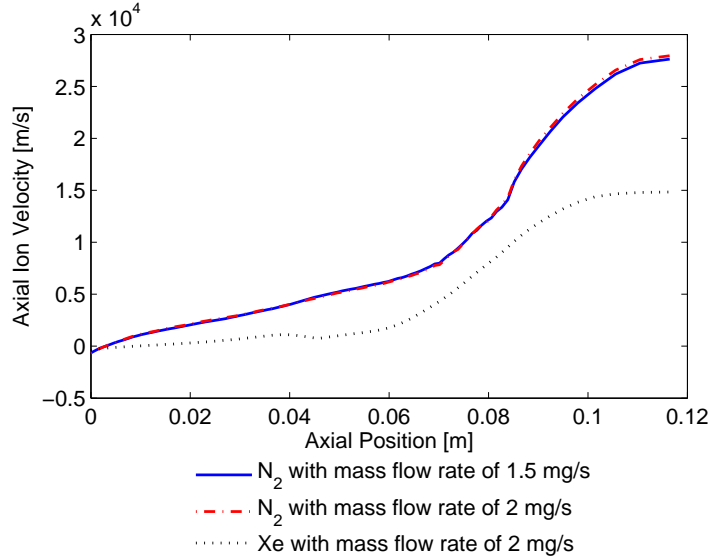

Figure 5.6: Simulated ion velocity of the N_2-fueled SHT at discharge voltage of 200 V.

Figure 5.8 shows that potential drop in the N_2-fueled SHT is more gradual than the Xe-fueled SHT, providing a wider acceleration zone for ions. The shape of the potential drop is closely related to the shape of the effective mobility profile presented in Fig. 5.9, where the computed transport barrier is qualitatively less significant for the N_2-fueled SHT with both mass flow rates. From this figure, one can also notice that the turbulent model is not a strong function of mass flow rate.

The initial simulation results indicates that an existing Hall thruster optimized for
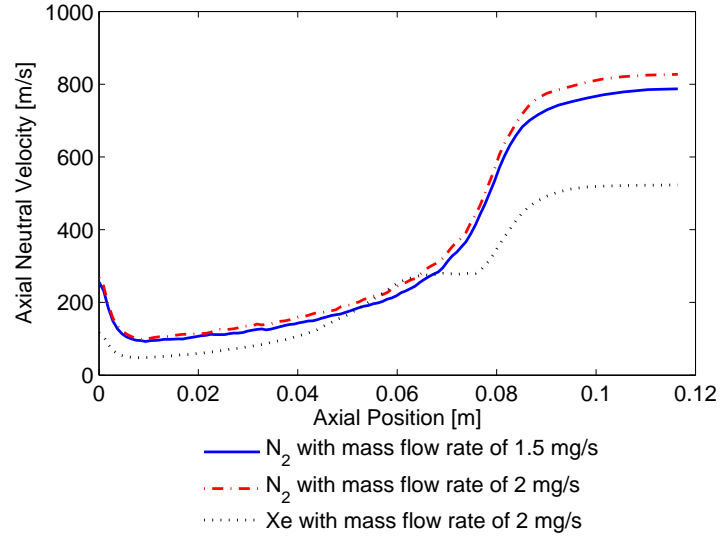
Figure 5.7: Simulated neutral velocity of the N_2-fueled SHT at discharge voltage of 200 V.
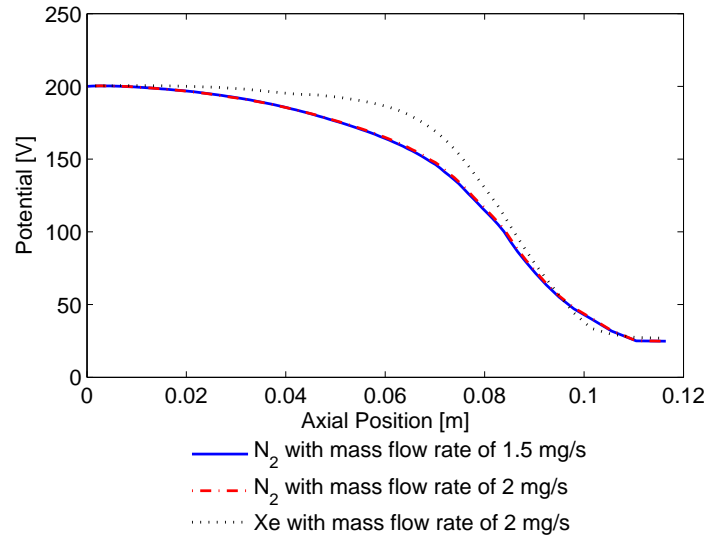
Figure 5.8: Simulated potential of the N_2-fueled SHT at discharge voltage of 200 V.
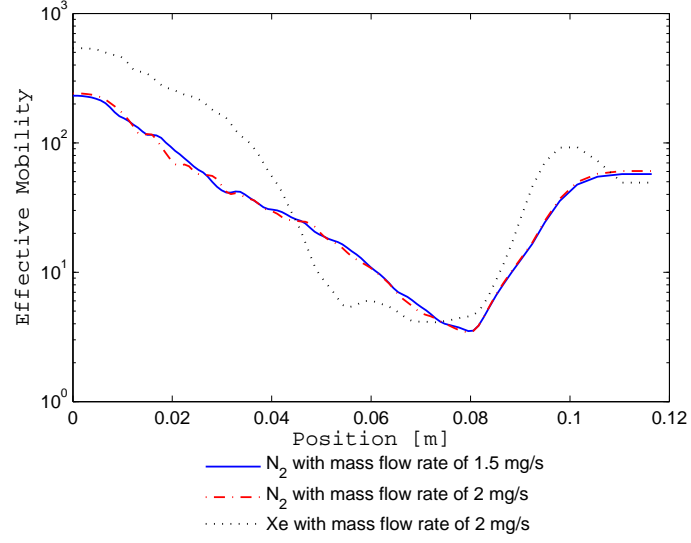
Figure 5.9: Simulated mobility of the N_2-fueled SHT at discharge voltage of 200 V.
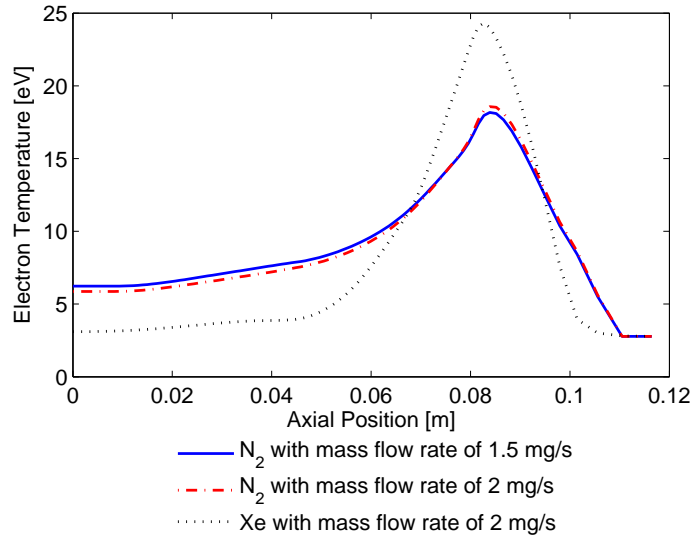
Figure 5.10: Simulated electron temperature of the N_2-fueled SHT at discharge voltage of 200 V.

xenon propellant would perform poorly with nitrogen fed as an alternative propellant. Although increasing mass flow rate can be a quick patch, it would be ideal to aim for designing a new geometry or magnetic field configuration, an example of which can be found in the appendix.

Chapter 6

Conclusions and Future Work

Radial-axial hybrid PIC (Particle-in-Cell) Hall thruster simulations are useful in investigating plasma-wall interaction and parametric performance study. However, the difficulty in modeling the anomalous electron transport limits the simulations to be widely utilized for various types of applications and their operating conditions. The dynamic models developed and implemented in this work calculate the electron transport across the applied magnetic field (electron mobility) similar to that experimentally estimated. Furthermore, the turbulent model is capable of capturing the structure and the dynamic characteristic of the electron mobility.

Entropy closure model uses a dimensional reasoning to model entropy production in a 1-D entropy transport equation, leading to an equation of the electron mobility, which relies on two parameters: the dependency function (f) of electron mobility on entropy production and the constant α. The simulated plasma properties of the initial implementation show reasonable agreement with those from experiments, although the simulated mobility is in marginal agreement with the experimental mobility. In order to increase the accuracy and utility of the entropy model, further investigation on other forms of dependency function and a parametric study on the adjustable constant α are suggested. The development of a method to mitigate numerical instability for the simulation when the mobility fluctuates must be preceded as well.

The turbulent transport model assumes that the turbulent energy dissipation is related to the Joule heating. Using a scaling law similar to the fluid kinetic theory,

the effective electron mobility scales to an simple function of plasma properties those are calculated within the simulation. The simulated mobility captures the transport barrier which characterizes the plasma behavior in Hall thrusters better than classical collision theory and a Bohm type mobility model. Without a fitting parameter tuned to experiments, this model is tested on an SPT-type thruster. Due to lack of information of the applied magnetic field, the accuracy of the simulated results is not validated. But we observed that the results agree with the published experimental data measured at a range of the magnetic coil current. The nitrogen (N_2)-fueled SHT is also simulated using the turbulent model. As expected, the light mass and the stable molecular structure of nitrogen caused the costly ionization in Hall thruster that leads to a poor thrust performance.

Future work is recommended to include the collaboration with the authors of the French SPT-100-ML data to obtain the accurate magnetic field for the SPT simulation. Also, more tests on other types of Hall thruster and operation conditions would help us determine if the parameter $K = 1/2$ is valid and universal. With a transferable K, the turbulent model is expected to be a useful tool to design a novel application and optimize operating condition.

Appendix A

Optimization of Nitrogen Hall Thruster

The initial simulation results of Chapter 5 indicates a low performance with the nitrogen propellant when run on the existing Stanford Hall Thruster (SHT). Therefore, optimization tailored to the characteristic of a nitrogen propellant is required. Because the main reason for the low performance is the low ionization due to the fast flying nitrogen particles, a modification in the magnetic field configuration and resulting changes in thruster are adopted. In addition, the propellant injection rate is increased to promote overall performance and to explore the optimum regime for nitrogen propellant. The simulation results presented here suggest that nitrogen-fueled thrusters are more appropriate for higher-power class missions (1 kW or higher).

A.1 Modification in Magnetic Field Configuration and Geometry

The goal of the modification is to broaden and intensify the ionization zone, also known as the Hall region, to increase the probability of ionization of N_2. The original magnetic field of the SHT has the peak of the magnetic field at the exit plane by a perpendicularly placed conducting plate with a depth of 3 millimeters, as shown in
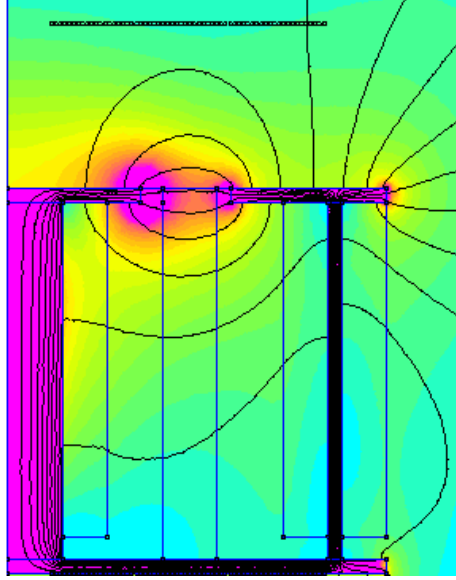
Figure A.1: SHT magnetic field flux lines.

Fig. A.1. The magnetic field lines are concentrated near this 3-millimeter depth across the channel (Fig. A.1). With denser and straighter magnetic flux lines, this region is where the Hall effect is strongest and thus most ionizations occur. To increase the probability of ionization of N_2, this ionization region is widened toward the upstream because the nitrogen particles are moving as twice as fast as the xenon particles, as can be calculated using the kinetic theory discussed as Eq. 5.1. In addition, it is suggested that a stronger applied magnetic field is required to compensate for the harder-to-ionize characteristics of N_2.

Finite Element Method Magnetics (FEMM) [55] is used to simulate modified configurations for magnetic field profiles. Through a trial-and-error approach to meeting the prescribed conditions for modified configuration, the design shown in Fig. A.2 is adopted as the final configuration of the N_2 thruster. In this design, the following modifications are applied to the existing SHT:

- Shortened solenoids (magnetic coils)

- Thickened and extended exit plane that encompasses the acceleration zone

- Offset of the whole channel toward the exit zone
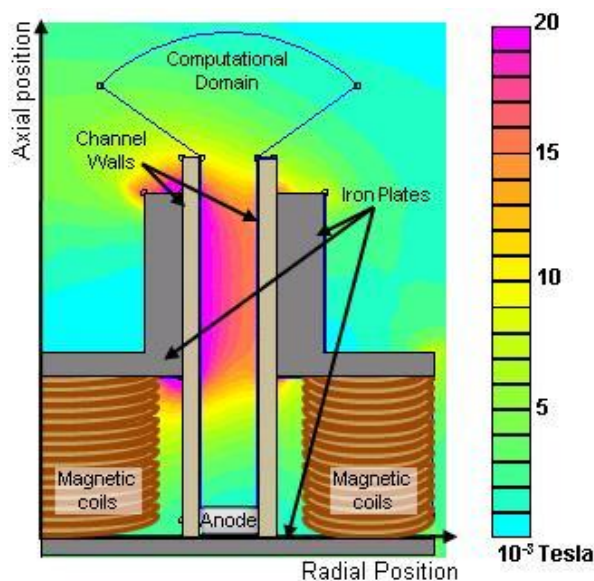
- Increased current in solenoids

Figure A.2: FEMM generated magnetic field profiles of modified SHT design for nitrogen.

Note that the key change in design is the shortening magnetic coils, which allowed an extension in the exit plane of conducting metal into a channel-surrounding wall. This surrounding wall of conducting material enabled us to generate a more gradual and wider peak than that of the original SHT design. Offsetting the channel toward the exit zone is achieved by a combination of an offset of anode and an extension of the channel length, to maintain the effective channel length (a distance from anode to exit plane) to be 80 millimeters. The source currents applied to the solenoids are increased by about 250 % of the original configuration; thus, the resulting source current density of the center coil is 0.6 MA/m^2 and that of each of the corner coils is 0.342 MA/m^2.

Figure A.3 compares the resulting magnetic field strength of the SHT and N_2 thruster along the centerline of the channel. Note that the exit plane at 0.08 m of the axial position, which corresponds to peak of the SHT magnetic field. As desired, the modified magnetic field for the N_2 thruster has a wider plateau in the middle of the channel instead of a sharp peak.
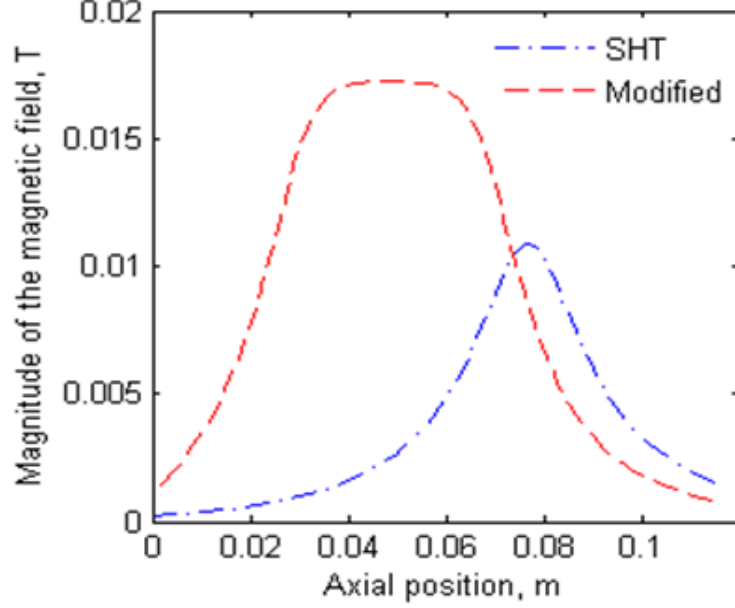
Figure A.3: Comparison of magnetic field profile of the SHT and N_2 thruster.

A.2   Shear-based Transport Model

To implement the modified configuration into the existing Hall thruster simulation, a shear-based transport model of Scharfe [63], or shear model, is used instead of the dynamic mobility models introduced in this thesis because these models have not been fully tested with its transportability for a substantial modification in magnetic field. The shear model is a semi-empirical model with two fitting parameters. The model attempts to account for the suppression of transport-causing fluctuations by the strong shearing in the electron fluid along the cross-field direction in regions of strong magnetic field. The shear model is expressed as an effective inverse Hall parameter as followed:

$$(\omega_{ce}\tau)_{\text{eff}}^{-1} = (\omega_{ce}\tau)_{\text{clas}}^{-1} + (\omega_{ce}\tau)_{\text{nw}}^{-1} + (\omega_{ce}\tau)_{\text{fluc}}^{-1} \left(\frac{1}{1 + (Cs)^2} \right) \tag{A.1}$$

where $(\omega_{ce}\tau)^{-1}_{\text{clas}}$ is the contribution of electon-neutral collisions, $(\omega_{ce}\tau)^{-1}_{\text{nw}}$ is the near-wall term based on the electron collision rate with channel walls, $(\omega_{ce}\tau)^{-1}_{\text{fluc}}$ accounts for the transport due to fluctuations, and the shear rate s is given by

$$s = \frac{dv_{\text{e},\theta}}{dz} = \frac{dE_{\text{z}}/B_{\text{z}}}{dz} \tag{A.2}$$

Due to the lack of experimental data for the modified nitrogen Hall thrusters, the fitting parameters $(\omega_{ce}\tau)_{\text{fluc}}$ and C are guessed to be similar to those fitted for xenon-fueled SHT, $(\omega_{ce}\tau)_{\text{fluc}} = 10$ and $C = 9 \times 10^{-8}$. Thus, $(\omega_{ce}\tau)_{\text{fluc}} = 5$ and $C = 2 \times 10^{-8}$ s are used in this study.

A.3 Simulation Results for Modifications

The FEMM-generated magnetic field profile for N_2 thruster, as shown in Fig. A.3, is implemented in the simulation to investigate the effect of the modification for N_2. Discharge voltage is 200 V for all cases discussed in this section. However, the propellant mass flow rate was varied from the nominal 1 mg/s up to 3.5 mg/s to test the effect of the mass flow rate on the thruster's performance.

A.3.1 Results for Mass Flow Rate of 1 mg/s

For an initial test of the simulating the newly designed N_2 thruster, 1 mg/s is used as the mass flow rate. Modified design of magnetic field proved effective by raising the mean current up to 68 %, from 3.1 A to 5.2 A, because higher current originates from higher production of ions in the channel through ionizations. One of the most direct effects of the modified magnetic field is shown at the comparison of plasma potential profiles simulated with the two configurations in Fig. A.4. The plasma potential drops gradually throughout the channel for the modified configuration, whereas in the SHT, the potential drops sharply near the exit plane, which is at 0.08 m of the axial position. Enhanced ionization is also represented in the plasma density, which is increased by approximately 50 % at their peak values. As another effect of widened modified magnetic field, electron temperature of simulation with the N_2

thruster has a flatter peak than that of simulation with the SHT. While axial neutral velocity was not affected by the changed in magnetic field, the lower neutral density for the modified design in overall domain suggests the consistent implication that the ionization rate was increased. It is also noteworthy that the gap between the neutral densities of the two configurations are largest at the axial position from 0.02 to 0.04 m, implying that the increased portion of ionization occurs mainly in this region. Thus, we can conclude that the ionization zone is effectively moved toward the upstream of the channel as intended by the modification.
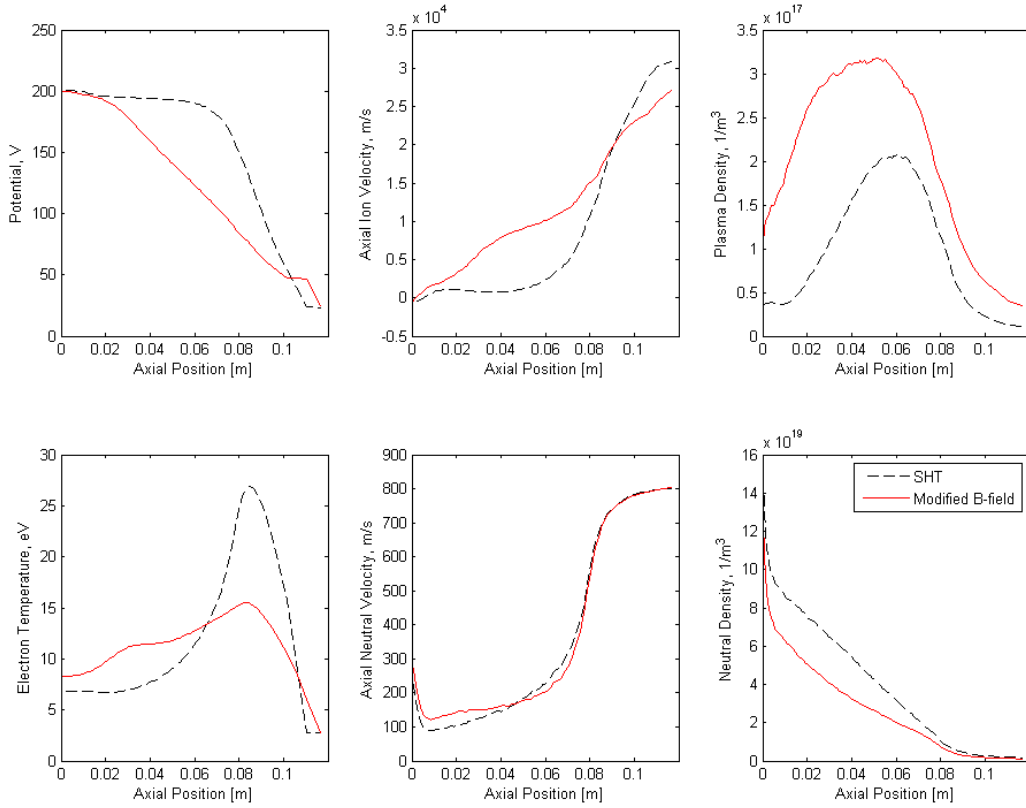

Figure A.4: Comparison of simulated plasma properties of the N_2 thruster (solid) with simulated results of the SHT (dashed). Both used N_2 as propellants at 1 mg/s. Discharge voltage is 200 V.

Thruster performance was also significantly enhanced due to the promoted ionization. Thrust was raised from 6.8 to 12.3 mN and efficiency from 3.7 to 7.3 %. However, these performance indexes are still in the uninterestingly low range that weakens the significance of this study. Therefore, further optimization of operating conditions was necessary.

A.3.2 Results with Increased Mass Flow Rate

In this section, simulated results with increased mass flow rates tested up to 3.5 mg/s with 0.5 mg/s increment are presented. Figure A.5 compares the plasma densities of simulation results with mass flow rates of 1 mg/s, 1.5 mg/s, and 2 mg/s on the N_2 thruster. The calculated peak values are 3.17×10^{17} m^{-3}, 7.80×10^{17} m^{-3}, and 1.23×10^{18} m^{-3} respectively. It is noteworthy that the trend of increase in peak plasma density is not linear, but higher than linear increase with respect to the mass flow rates.

Table A.1 presents the effect of mass flow rate on the performances of the simulated results with mass flow rates from 1 mg/s to 3.5 mg/s with the increment of 0.5 mg/s. Comparing the increase in performance at each increment, one can observe the highest promotion of the overall performance at the increment between 1 and 1.5 mg/s. This suggests the existence of an critical point in this range of mass flow rate beyond which ionization boosts up. Currents and thrusts keeps increasing with respect to the increase of mass flow rate almost linearly. Specific impulse and efficiency, however, reaches maximum points and get saturated at mass rate between 2.5 and 3.5 mg/s. On the other hand, thrust to power ratio (T/P) is highest at mass rate of 1.5 mg/s and it is almost constant for the mass flow rate higher than 1.5 mg/s, implying that the thrust and power is equally affected by the increase in mass flow rate. Therefore, the optimal mass flow rate for the N_2 thruster at 200 V should be at least 2.5 mg/s when the specific impulse and efficiency are the most important criteria. If the power is one of the criteria, one can refine the increment in mass flow rate and search for the current required. I suggest the N_2 thruster is expected to perform at its best for the missions that require a power higher than 3.5 kW and for those that has
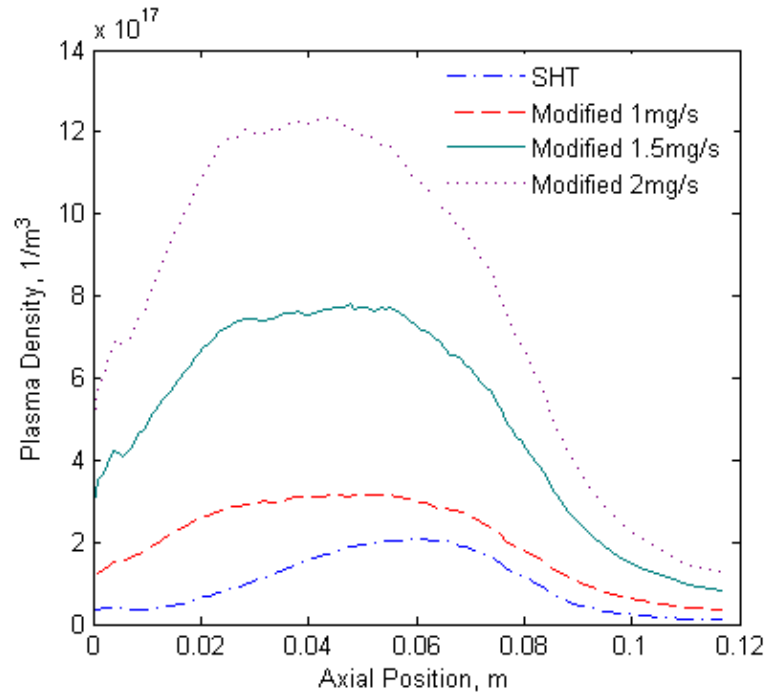
Figure A.5: Comparison of simulated plasma density at varying mass flow rates with the N_2 thruster. Simulated plasma density with the SHT at 1 mg/s (dash-dot) is given as guidance for the index of enhanced ionization.

sufficient power source (such as from solar panel) so that the low efficiency could be compensated.

A.3.3 Nitrogen Thruster Prototype

Based on the modified design discussed in this thesis, the thruster geometry of Fig. A.2 was prototyped by colleagues in the Stanford Plasma Physics Laboratory (SPPL) as shown in Fig. A.6, whose operation is shown in Fig. A.7.

Table A.1: Performance summary for N_2 thruster with varying mass flow rate. Discharge voltage is 200 V.

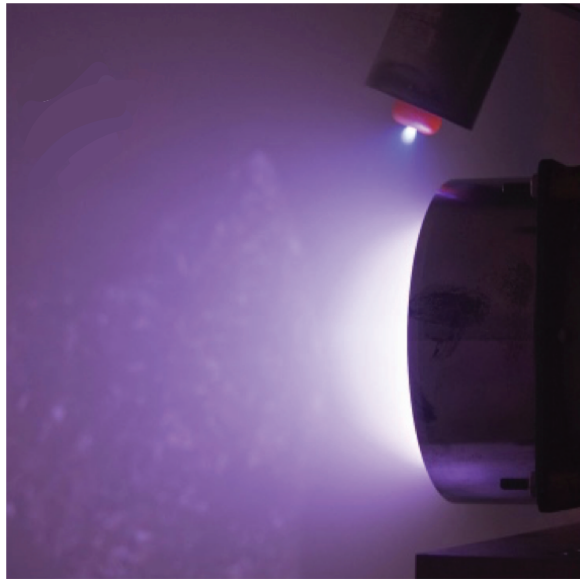| Magnetic Field Configuration	Mass Flow [mg/s]	Thrust [mN]	Current [A]	I_{sp} [s]	η [%]	T/P [mN/kW]
SHT	1	6.8	3.1	692	3.7	9.19
Modified	1	12.3	5.2	1324	7.3	8.42
	1.5	24.4	10.5	1662	9.5	12.84
	2	38.6	16.5	1971	11.3	11.68
	2.5	53.9	22.89	2202	12.75	11.79
	3	68.4	28.75	2328	13.62	11.90
	3.5	79.3	33.17	2313	13.61	11.96

Figure A.6: N_2 thruster prototype.

Figure A.7: N$_2$ thruster prototype operating. Photography by Andrew Smith.

Appendix B

Polytropic Model of Electron Transport

According to Knoll and Cappelli [17], the axial variation of electron entropy along the Hall thruster channel seems to be negligible, especially for the lower discharge voltage (V_d) regime ($V_\mathrm{d} \leq 160$ V). Assuming 1-D entropy flow and a local equilibrium, the entropy per electron, s_e, is expressed using the Sackur-Tetrode equation [30], as previously mentioned in Chapter 3 (Eq. 3.12):

$$s_\mathrm{e} = \frac{5k_\mathrm{B}}{2}\ln T_\mathrm{e} - k_\mathrm{B}\ln p_\mathrm{e} + k_\mathrm{B}\left\{\ln\left[\left(\frac{2\pi m_\mathrm{e}}{h^2}\right)^{3/2}k_\mathrm{B}^{5/2}\right] + \frac{5}{2}\right\} + k_\mathrm{B}\ln 2$$

where h is Planck's constant ($6.62606957 \times 10^{-34}\,\mathrm{m^2kg/s}$) and the isotropic pressure, p_e is assumed to obey the ideal gas law, $p_\mathrm{e} = n_\mathrm{e}k_\mathrm{B}T_\mathrm{e}$.

Applying the isentropic assumption, $\nabla s_\mathrm{e} = 0$, yields the simple relation between the electron temperature and the electron density, as follows:

$$\frac{3}{2}\frac{n_\mathrm{e}}{T_\mathrm{e}}\nabla T_\mathrm{e} - \nabla n_\mathrm{e} = 0 \tag{B.1}$$

$$T_\mathrm{e} = C_1 n_\mathrm{e}^{\frac{2}{3}} \tag{B.2}$$

where C_1 is the constant of integration which must be specified empirically. A calculation using measured n_e and T_e of the SHT [17] indicates that the constant C_1 varies with respect to the applied V_d. For the nominal condition of 200 V discharge voltage and 2 mg/s xenon flow, the experimental data requires C_1 to be on the order of 10^{-7} K-m^2.
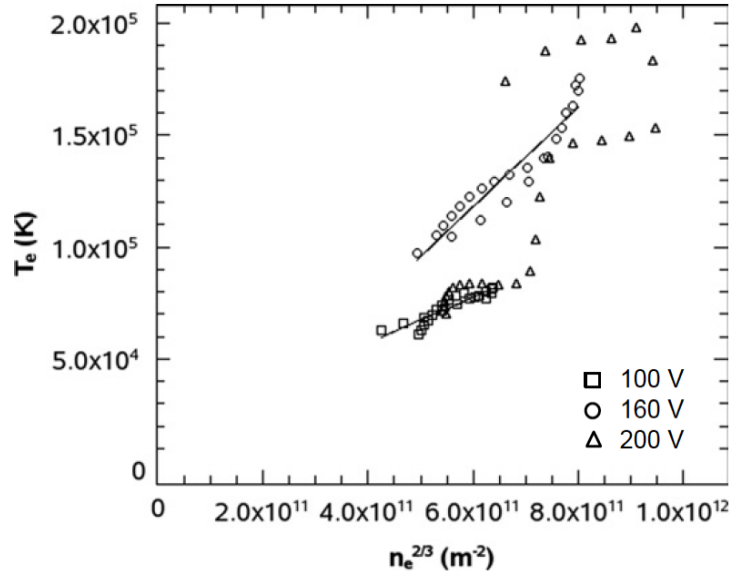

Figure B.1: Electron temperature versus number density raised to the 2/3 power.

The exponent 2/3 is derived directly from the isentropic relation in Eq. B.2. However, Fig. B.1 (taken from Ref. [17]) where T_e is plotted against $n_e^{2/3}$ using experimental data shows that the relation B.2 needs modification, especially for the 200 V case. Therefore we open the possibility of taking other factors than 2/3 for the exponent, so that the Eq. B.2 becomes a polytropic relation,

$$T_e = C_1 n_e^k \tag{B.3}$$

where k is called the polytropic constant.

This relation substitutes the part that solves for electron temperature in the simulation, while the electron equations Eq. 2.12-2.14 are rearranged to express the

effective electron mobility. Note that the above expression for T_e resolves the electron temperature in two-dimension (R-Z) directly from the 2-D electron density field which is calculated from PIC part.

Bibliography

[1] Choueiri, E. Y., "New Dawn for Electric Rockets," *Scientific American*, Feb 2009.

[2] Goddard, R. H., "Method and Means for Producing Electrified Jets of Gas," 1917.

[3] Koppel, C. R. and Estublier, D., "The SMART-1 Hall Effect Thruster Around the Moon: In Flight Experience," *Proceedings of the 29th International Electric Propulsion Conference*, 2005.

[4] Thomas, C. A., *Anomalous Electron Transport in the Hall-Effect Thruster*, Ph.D. thesis, Stanford University, Stanford, CA, 2006.

[5] Fernandez, E., Cappelli, M. A., and Mahesh, K., "2D Simulations of Hall Thrusters," *Center for Turbulance Research Annual Research Briefs*, 1998, pp. 81.

[6] Scharfe, J. M., *Nonlinear Hybrid-PIC Modeling and Electrostatic Probe Survey of Hall Thrusters*, Ph.D. thesis, Massachusetts Institute of Technology, Cambridge, MA, 1999.

[7] Birdsall, C. and Langdon, A., *Plasma physics via computer simulation*, The Adam Hilger series on plasma physics, McGraw-Hill, 1985.

[8] Dawson, J. M., "Particle simulation of plasmas," *Reviews of Modern Physics*, Vol. 55, Apr 1983, pp. 403–447.

[9] Hirakawa, M. and Arakawa, Y., "Numerical simulation of plasma particle behavior in a Hall thruster," *AIAA*, Vol. 3195, 1996.

[10] Janes, G. S. and Lowder, R. S., "Anomalous Electron Diffusion and Ion Acceleration in a Low-Density Plasma," *Physics of Fluids*, Vol. 9, June 1966, pp. 1115–1123.

[11] Meezan, N. B., Hargus Jr., W. A., and Cappelli, M. A., "Anomalous Electron Mobility in a Coaxial Hall Discharge Plasma," *Physical Review E*, Vol. 63, Feb 2001.

[12] Bohm, D., Burhop, E., and Massey, H., *The Characteristics of Electrical Discharges in Magnetic Fields*, McGraw Hill, 1949.

[13] Scharfe, M. K., *Electron Cross Field Transport Modeling in Radial-Axial Hybrid Hall Thruster Simulations*, Ph.D. thesis, Stanford University, Stanford, CA, 2009.

[14] Morozov, A., "Effect of Near-Wall Conductivity in a Strongly Magnetized Plasma," 1968.

[15] Meezan, N. B. and Cappelli, M. A., "Kinetic study of wall collisions in a coaxial Hall discharge," *Physical Reciew E*, Vol. 66, No. 036401, 2002.

[16] Hagelaar, G. J. M., Bareilles, J., Garrigues, L., and Boeuf, J. P., "Two-dimensional model of a stationary plasma thruster," *Journal of Applied Physics*, Vol. 91, No. 9, 2002.

[17] Knoll, A. K. and Cappelli, M. A., "A Simple Isentropic Model of Electron Transport in Hall Thrusters," *Journal of Physics D: Applied Physics*.

[18] Knoll, A. K., *Plasma Oscillations and Associated Electron Transport within Hall Thrusters*, Ph.D. thesis, Stanford University, Stanford, CA, 2010.

[19] Bittencourt, J., *Fundamentals of Plasma Physics*, Springer, 2004.

[20] Rejoub, R., Lindsay, B. G., and Stebbings, R. F., "Determination of the absolute partial and total cross sections for electron-impact ionization of the rare gases," *Phys. Rev. A*, Vol. 65, Apr 2002, pp. 042713.

[21] Nagy, P., Skutlartz, A., and Schmidt, V., "Absolute ionisation cross section for electron impact in rare gases," *Journal of Physics B: Atomic and Molecular Physics*, Vol. 13, 1980, pp. 1249–1267.

[22] Hwang, W., Kim, Y.-K., and Rudd, M. E., "New Model for Electron-Impact Ionization Cross Sections of Molecules," *Journal of Chemical Physics*, Vol. 104, Feb. 1996, pp. 2956.

[23] Moin, P., *Fundamentals of Engineering Numerical Analysis Second Edition*, Cambridge University Press, 32 Avenue of the Americas, New York, NY 10013-2473, USA, 2010.

[24] Dugan, J. V. and Sovie, R. J., *Volume ion production costs in tenuous plasmas: A general atom theory and detailed results for helium, argon, and cesium*, National Aeronautics and Space Adminiatration, 1967.

[25] Barral, S., Makowski, K., Paradzynski, Z., Gascon, N., and Dudeck, M., "Wall material effects in stationary plasma thrusters. II. Near-wall and in-wall conductivity," *Physics of Plasmas*, Vol. 10, No. 10, October 2003.

[26] Cha, E., Cappelli, M. A., and Fernandez, E., "Implementation of a Polytropic Model for Two-dimensional Hybrid Hall Thruster Simulations," *Bulletin of the American Physics Society, 65th Annual Gaseous Electronics Conference*, Vol. 57, No. 8, 2012.

[27] Smith, A. W. and Cappelli, M. A., "Time and Space-correlated Plasma Potential Measurements in the Near Field of a Coaxial Hall Plamsa Discharge," *Physics of Plasmas*, Vol. 16, 2009, pp. 073504.

[28] Bridgeman, P. W., "Dimensional Analysis," 1922.

[29] Schobeiri, M. T., *Fluid Mechanics for Engineers: A Graduate Textbook*, Springer, 2010.

[30] Vincenti, W. G. and Kruger, Jr., C. H., *Introduction to Physical Gas Dynamics*, Robert E. Krieger Publishing Co., INC., 1965.

[31] Barral, S. and Ahedo, E., "Low-frequency model of breathing oscillations in Hall discharges," *Phys. Rev. E*, Vol. 79, Apr 2009, pp. 046401.

[32] Cappelli, M. A., Cha, E., and Fernandez, E., "Entropy Closure Model for Transport in Hall Thruster Simulations," *Proceedings of the 33rd International Electric Propulsion Conference*, 2013.

[33] Choueiri, E. Y., "Plasma Oscillations in Hall Thrusters," *Physcis of Plasmas*, Vol. 8, No. 4, Apr 2001.

[34] Gascon, N. and Cappelli, M. A., "Plasma Instabilities in the Ionization Regime of a Hall Thurster," *Proceedings of the 39th Joint Propulsion Conference*.

[35] Lazurenko, A., Albarede, L., and Bouchoule, A., "Physical Characterization of High-Frequency Instabilities in Hall Thrusters," *Physics of Plasmas*, Vol. 13, 2006.

[36] Tsikata, S., Lemoine, N., Pisarev, V., and Gresillon, D. M., "Dispersion Relations of Electron Density Fluctuations in a Hall Thurster Plasma, Observed by Collective Light Scattering," *Physics of Plasmas*, Vol. 033506, No. 16, 2009.

[37] Baranov, V., Nazarenko, Y., Petrosov, V., Vasin, A., and Yashnov, Y., "Theory of Oscillations and Conductivity for Hall Thrusters," *Proceedings of 32nd AIAA Joint Propulsion Conference*, 1996.

[38] Litvak, A. A. and Fisch, N. J., "Resistive Instabilities in Hall Current Plasma Discharge," *Physcis of Plasmas*, Vol. 8, No. 2, 2001.

[39] Fernandez, E., Scharfe, M., Thomas, C., Gascon, N., and Cappelli, M., "Growth of Resistive Instabilities in E×B Plasma Discharge Simulations," *Physics of Plasmas*, Vol. 15, No. 1, 2008, pp. 012102.

[40] Litvak, A. A. and Fisch, N. J., "Rayleigh Instabilities in Hall Thrusters," *Physics of Plasmas*, Vol. 11, No. 4, 2004.

[41] Kapulkin, A. and Guelman, M. M., "Low-Frequency Instability in Near-Anode Region of Hall Thruster," *IEEE Transactions on Plasma Science*, Vol. 36, No. 5, 2008.

[42] Frias, W., Smolyakov, A. I., Kaganovich, I. D., and Raitses, Y., "Long Wavelength Gradient Drift Instability in Hall Plasma Devices. I. Fluid Theory," *Physics of Plasmas*, Vol. 19, No. 7, 2012.

[43] Morozov, A. I., Esipchuk, Y. V., Kapulkin, A. M., Nevrovskii, V. A., and Smirnov, V. A., "Azimuthally Asymmetric Modes and Anomalous Conductivity in Closed Electron Drift Accelerators," *Soviet Physics Technical Physics*, Vol. 18, 1973.

[44] Davidson, P., *An Introduction to Magnetohydrodynamics*, Cambridge Texts in Applied Mathematics, Cambridge University Press, 2001.

[45] Tennekes, H. and Lumley, J., *A First Course in Turbulence*, Pe Men Book Company, 1972.

[46] Taylor, G. I., "Statistical Theory of Turbulence," *Proceedings of the Royal Society of London. Series A, Mathematical and Physical Sciences*, Vol. 151, No. 873, 1935, pp. pp. 421–444.

[47] Doshi, M. R. and Gill, W. N., "A Note on the Mixing Length Theory of Turbulent," *AIChE Journal*, Vol. 16, No. 5, 1970.

[48] Adam, J. C., Boeuf, J. P., Dubuit, N., Dudek, M., Garrigues, L., Gresillon, D., Heron, A., Hagelaar, G. J. M., Kulaev, V., Lemoine, N., Mazouffre, S., Luna, J. P., Pisarev, V., and Tsikata, S., "Physics, Simulations and Diagnostics of Hall Effect Thrusters," *Plasma Physics and Controlled Fusion*, Vol. 50, No. 12, 2008.

[49] Cappelli, M. A., Young, C. V., Cha, E., and Fernandez, E., "A Zero-Equation Turbulence Model for Two-Dimensional Hybrid Hall Thruster Simulations," *submitted to Physics of Plasmas*, 2015.

[50] Bouchoule, A., Cadiou, A., Hron, A., Dudeck, M., and Lyszyk, M., "An Overview of the French Research Program on Plasma Thrusters for Space Applications," *Contributions to Plasma Physics*, Vol. 41, No. 6, 2001, pp. 573–588.

[51] Bechu, S., Perot, C., Gascon, N., Lasgorceix, P., Hauser, A., and Dudeck, M., "Operating Mode Investigation of a Laboratory Stationary Plasma Thruster," *American Institute of Aeronautics and Astronautics*, , No. 99-2567, 1999.

[52] Bouchoule, A., Boeuf, J.-P., Heron, A., and Duchemin, O., "Physical investigations and developments of Hall plasma thrusters," *Plasma Physics and Controlled Fusion*, Vol. 46, No. 12B, 2004, pp. B407.

[53] Lasgorceix, P., Perot, C., Dudeck, M., Beltan, T., and Cadiou, A., "P.I.V.O.I.N.E. Ground Test Facility For Ion Thruster Testing," *Proceedings of the Second European Spacecraft Propulsion Conference*, 1997.

[54] Dorval, N., Bonnet, J., Marque, J. P., Rosencher, E., Chable, S., Rogier, F., and Lasgorceix, P., "Determination of the ionization and acceleration zones in a stationary plasma thruster by optical spectroscopy study: Experiments and model," *Journal of Applied Physics*, Vol. 91, No. 8, 2002.

[55] Meeker, D., "Finite Element Method Magnetics Version 4.2 User's Manual," *http://www.femm.info*, 2010.

[56] Scharfe, D. B., *Alternative Hall Thruster Propellants Krypton and Bismuth: Simulated Performance and Characterization*, Ph.D. thesis, Stanford University, Stanford, CA, 2009.

[57] Maleka, J. M., Washeleski, R. L., Massey, D. R., King, L. B., and Hopkins, M. A., "Development of a Magnesium and Zinc Hall-effect Thruster," *Proceedings of the 31st International Electric Propulsion Conference*, 2009.

[58] Frisbee, R. H., Polk, J. E., Gallimore, A. D., and Marrese, C. M., "Oxygen-Propellant Plasma Thrusters for Cis-Lunar Electric Propulsion Missions," *Proceedings of 34th AIAA/ASME/SAE/ASEE Joint Propulsion Conference and Exhibit*, 1998.

[59] Saporoschenko, M., "Ions in Nitrogens," *Physical Review*, Vol. 111, No. 6, 1958.

[60] Boivin, R. F. and Scime, E. E., "Control of Nitrogen Species in Helicon Plasmas," *Plasma Source Science and Technology*, Vol. 14, No. 2, Mar. 2005, pp. 283–292.

[61] Brown, S. C., *Introduction to Electrical Discharges in Gases*, John Wiley and Sons, 1966.

[62] Hagelaar, G. J. and Pitchford, L. C., "Solving the Boltzmann Equation to Obtain Electron Transport Coefficients and Rate Coefficients for Fluid Models," *Plasma Source Science and Technology*, Vol. 14, Oct. 2005, pp. 722–733.

[63] Scharfe, M. K., Thomas, C., Scharfe, D. B., Gascon, N., Cappelli, M. A., and Fernandez, E., "Shear-Based Model for Electron Transport in Hybrid Hall Thruster Simulations," *IEEE Transactions on Plasma Science*, Vol. 26, No. 5, 2008, pp. 2058.